NASA/TM-2009-215718

Experimental Investigation of Project Orion Crew Exploration Vehicle Aeroheating: LaRC 20-Inch Mach 6 Air Tunnel Test 6931

Brian R. Hollis
Langley Research Center, Hampton, Virginia

April 2009

NASA STI Program . . . in Profile

Since its founding, NASA has been dedicated to the advancement of aeronautics and space science. The NASA scientific and technical information (STI) program plays a key part in helping NASA maintain this important role.

The NASA STI program operates under the auspices of the Agency Chief Information Officer. It collects, organizes, provides for archiving, and disseminates NASA's STI. The NASA STI program provides access to the NASA Aeronautics and Space Database and its public interface, the NASA Technical Report Server, thus providing one of the largest collections of aeronautical and space science STI in the world. Results are published in both non-NASA channels and by NASA in the NASA STI Report Series, which includes the following report types:

- TECHNICAL PUBLICATION. Reports of completed research or a major significant phase of research that present the results of NASA programs and include extensive data or theoretical analysis. Includes compilations of significant scientific and technical data and information deemed to be of continuing reference value. NASA counterpart of peer-reviewed formal professional papers, but having less stringent limitations on manuscript length and extent of graphic presentations.

- TECHNICAL MEMORANDUM. Scientific and technical findings that are preliminary or of specialized interest, e.g., quick release reports, working papers, and bibliographies that contain minimal annotation. Does not contain extensive analysis.

- CONTRACTOR REPORT. Scientific and technical findings by NASA-sponsored contractors and grantees.

- CONFERENCE PUBLICATION. Collected papers from scientific and technical conferences, symposia, seminars, or other meetings sponsored or co-sponsored by NASA.

- SPECIAL PUBLICATION. Scientific, technical, or historical information from NASA programs, projects, and missions, often concerned with subjects having substantial public interest.

- TECHNICAL TRANSLATION. English-language translations of foreign scientific and technical material pertinent to NASA's mission.

Specialized services also include creating custom thesauri, building customized databases, and organizing and publishing research results.

For more information about the NASA STI program, see the following:

- Access the NASA STI program home page at *http://www.sti.nasa.gov*

- E-mail your question via the Internet to help@sti.nasa.gov

- Fax your question to the NASA STI Help Desk at 443-757-5803

- Phone the NASA STI Help Desk at 443-757-5802

- Write to:
  NASA STI Help Desk
  NASA Center for AeroSpace Information
  7115 Standard Drive
  Hanover, MD 21076-1320

NASA/TM-2009-215718

Experimental Investigation of Project Orion Crew Exploration Vehicle Aeroheating: LaRC 20-Inch Mach 6 Air Tunnel Test 6931

Brian R. Hollis
Langley Research Center, Hampton, Virginia

National Aeronautics and
Space Administration

Langley Research Center
Hampton, Virginia 23681-2199

April 2009

Available from:

NASA Center for AeroSpace Information
7115 Standard Drive
Hanover, MD 21076-1320
443-757-5802

Table of Contents

List of Tables

List of Figures

Abstract

An investigation of the aeroheating environment of the Project Orion Crew Entry Vehicle has been performed in the Langley Research Center 20-Inch Mach 6 Air Tunnel. Data were measured on a ~3.5% scale model (0.1778-m/7-inch diameter) of the vehicle using coaxial thermocouples at free stream Reynolds numbers of 2.0×10^6/ft to7.30×10^6/ft and computational predictions were generated for all test conditions. The primary goals of this test were to obtain convective heating data for use in assessing the accuracy of the computational technique and to validate test methodology and heating data from a test of the same wind tunnel model in the Arnold Engineering Development Center Tunnel 9. Secondary goals were to determine the extent of transitional/turbulent data that could be produced on a CEV model in this facility, either with or without boundary-layer trips, and to demonstrate continuous pitch-sweep operation in this tunnel for heat-transfer testing.

For laminar conditions, predictions and data generally agreed to within the estimated ±12% experimental uncertainty; this agreement was consistent with results from previous testing. The use of boundary-layer trips was shown to produce transitional flow on the model, however it was unclear if fully-turbulent flow was generated even at the highest test Reynolds number. Finally, comparisons between static and transient angle-of-attack data validated the continuous pitch-sweep mode of operation.

Nomenclature

Symbols

c_p	specific heat of test gas (J/kg/K)
D	vehicle maximum diameter (m or in.)
h	heat-transfer film-coefficient (kg/m^2/s)
h_{FR}	heat-transfer film-coefficient from Fay-Riddell theory (kg/m^2/s)
H_{AW}	adiabatic wall recovery enthalpy (J/kg)
H_w	wall enthalpy (J/kg)
H_o	total enthalpy (J/kg)
H_∞	free stream enthalpy (J/kg)
M_e	boundary layer edge Mach number
M_∞	free stream Mach number
p_w	pressure at model wall (Pa)
Pr	Prandtl number
q_{300}	predicted heat transfer rate at 300 K wall temperature (W/m^2)
q	heat transfer rate (W/m^2)
R	vehicle maximum radius (m)
R_n	radius of vehicle nose (m)

R_s radius of aftbody corner (m)
R_t cross-sectional radius of toroidal segment between heat-shield and aftbody (m)
Re_θ Reynolds number based on local boundary layer momentum thickness
Re_∞ free stream unit Reynolds number (1/m or 1/ft)
$Re_{\infty,D}$ free stream Reynolds number based on model diameter
St Stanton number (based on total enthalpy)
St_{aw} Stanton number (based on adiabatic wall recovery enthalpy)
$St \times (Re_{\infty,D})^{1/2}$ non-dimensional laminar heating correlation parameter
$St \times (Re_{\infty,D})^{1/5}$ non-dimensional turbulent heating correlation parameter
T_w wall temperature (K)
T_∞ free stream temperature (K)
x, y, z geometric coordinates (m)
$x/R, y/R, z/R$ normalized geometric coordinates
U_∞ free stream velocity (m/s)
α angle of attack (deg)
δ boundary layer thickness (m)
θ boundary layer momentum thickness (m)
ρ_∞ free stream density (kg/m^3)

Subscripts

AW adiabatic wall
e edge
w wall
0 stagnation or total
∞ free stream

Abbreviations

AEDC Arnold Engineering Development Center
AoA angle of attack
CEV Crew Exploration Vehicle
CFD computational fluid dynamics
ISS International Space Station
LaRC Langley Research Center
MSL Mars Science Laboratory
NIST National Institute of Standards and Technology
TPS thermal protection system

Background and Introduction

The Crew Exploration Vehicle concept was defined by NASA's Exploration Systems Architecture Study (Ref. 1) that was conducted in 2005 to define requirements for crew and cargo launch systems to support lunar and Mars exploration programs as well as access to the International Space Station (ISS). Several versions of the Orion CEV are planned that will provide transportation first to the ISS, then to the moon, and finally to Mars.

The Crew Module of the CEV (Figure 1) has a configuration that is outwardly similar to the Apollo Command Module - a spherical-segment heat shield joined by a small toroidal section to a truncated-cone shaped crew compartment. The Orion CEV however, will be considerably larger than Apollo with a maximum heat shield

diameter of ~5 m (current configuration) vs. 3.912 m for Apollo. This larger size will allow transport of up to six crew members on International Space Station missions or up to 4 crew members on Lunar missions.

An investigation of the aeroheating environment of the Project Orion Crew Exploration Vehicle (CEV) entry vehicle has been performed in the Langley Research Center (LaRC) 20-Inch Mach 6 Air Tunnel. This study compliments previous testing of the same wind tunnel model in the Arnold Engineering Development Center (AEDC) Tunnel 9 (Refs. 2 and 3). The goals of this study were to obtain laminar data for use in evaluating the accuracy of computational fluid dynamics (CFD) methods applied to the CEV configuration, to independently validate the test technique and data-acquisition/reduction procedures used during the AEDC test, and to investigate the use of boundary-layer trips to produce fully-developed turbulent flow on this vehicle configuration. An additional non-programmatic goal was to demonstrate the ability to acquire heat-transfer data in continuous pitch-sweep mode (as performed in the prior AEDC Tunnel 9 test) in this tunnel.

Experimental Method

Model Configuration and Instrumentation

A 0.03556-scale model (based on an assumed 5.00-m full scale at the time of the model design) of the CEV was used in this test. A drawing of the model is given in Figure 2 (note that the current configuration has advanced beyond that shown in this figure) and it is shown installed in the LaRC 20-Inch Mach 6 Air Tunnel in Figure 3. The model was fabricated from 15-5 precipitation-hardened stainless steel with an H1100 heat treatment. Although this model was developed originally for testing in AEDC Tunnel 9, the model maximum diameter of 17.78 cm (7.00-in) was chosen for consistency with previous CEV tests (Refs. 4 and 5) and to allow testing of this model in NASA Langley Research Center hypersonic wind tunnels. The model was designed to allow for substitution of a removable insert piece on the lower half of the forebody heat-shield as shown in Figure 4. Inserts with varying forms of distributed and discrete roughness elements were fabricated to allow for investigation of roughness effects on transition and turbulent heating. However, this planned aspect of testing at AEDC Tunnel 9 was minimized after the successful demonstration of natural transition at that tunnel's operating conditions. In the LaRC test, these inserts were also not employed because of the time that would have been required to perform the insert changes (several hours, which is acceptable in a once-per-day run schedule such as AEDC, but not in the multiple runs per day schedule at LaRC) and the lack of an AEDC data set for comparison. To acquire tripping data in this study, discrete squares of Kapton tape, which could be quickly applied to the model, were employed instead of the removable inserts. A description of this method can be found in Ref. 6. In this study, trips of 0.0045-in., 0.0065-in. and 0.0115-in. height were attached to the model along the leading edge of the insert as shown in Figure 5.

The model was instrumented with 101 MedTherm Type-E (chromel-constantan) coaxial thermocouples (installation shown in Figure 6 and Figure 7). The gages were press-fit through holes drilled into the model and then hand-worked to conform to the model surface and to form the required junctions between the chromel and constantan elements of the thermocouple. Thermocouple instrumentation is the primary method (Ref. 7) for obtaining heat-transfer data in AEDC Tunnel 9, which is the facility for which this model was designed. The two dissimilar metals that comprise a thermocouple produce a small, but measurable, voltage when two junctions are formed between the materials. In the case of wind tunnel test instrumentation, one junction is at the surface of the model where it is exposed to heating, and the other is located external to the model and maintained at a controlled reference temperature. The voltage output of a thermocouple is related to temperature through a National Institute of Standards and Technology (NIST) calibration standard (Ref. 8). Temperature-time histories recorded using thermocouples are processed through conduction analysis to determine heat-transfer rate time-histories.

A schematic of the thermocouple instrumentation layout is provided in Figure 8, and the gage locations are listed

in Table 1. There were 82 gages located on the forebody heat-shield portion of the model and the remaining 19 gages were located on the aftbody crew compartment. Gages on the heat shield were arrayed vertically along the centerline (pitch-plane) of the model and horizontally across the leeside (top) of the model where the highest turbulent augmentation occurs. This gage layout was intended for a general assessment of heating distributions over the entire body, not for detailed investigation of specific areas. As such, the spatial resolution in the high-gradient regions of the heat-shield shoulder and on the aftbody immediately following the shoulder was considered to be insufficient for definitive comparisons with computational results.

Test Facility

The NASA LaRC 20-Inch Mach 6 Air Tunnel (Figure 9) is a conventional blow-down facility in which heated, dried, and filtered air is used as the test gas. The tunnel has a two-dimensional, contoured nozzle that opens into a 20.5-in. × 20.0-in. test section. The tunnel is equipped with a bottom-mounted injection system that can transfer a model from the sheltered model box to the tunnel centerline in less than 1 second. During a run, the pitch system can sweep a model at rates of up to 6-deg/sec. Run times of up to 15 minutes are possible in this facility, although for aeroheating tests, run times of only a few seconds are required. The nominal reservoir conditions of this facility are stagnation pressures of 206.8 kPa to 3447.4 kPa (30 psia to 500 psia) with stagnation temperatures of 422 K to 555.5 K (760°R to 1000°R) that produce perfect-gas free stream conditions of Mach 5.8 to 6.1 with Reynolds numbers of 1.64×10^6 1/m to 23.2×10^6 /m (0.5×10^6 /ft to 7.1×10^6 /ft). A schematic of the facility is shown in Figure 10. More detailed information on this facility can be found in Ref. 9.

Data Reduction Method

The coaxial thermocouples with which the CEV model were instrumented produced voltage-time history data that were converted to temperature-time history data via gage calibration standards. From these data, a one-dimensional, finite-volume conduction analysis of the temperature distribution within the substrate of the model was then performed using the 1DHEAT (Ref. 10) code to determine the time-history of the external convective heating experienced by the wind tunnel model. The process was the same as that employed for the AEDC Tunnel 9 test of the same wind tunnel model, as well as that of a similarly-instrumented Mars Science Laboratory model, and a detailed discussion of the data reduction method, assumptions, and uncertainties for that test has been presented in Ref. 11. With respect to the experimental uncertainty, a tentative value of ±12% on heating rates has been estimated, although for consistency with Ref. 2, reference error bars of ±10% will be shown on the heating plots.

Run Matrix

A total of 68 runs were performed in Test 6931 in the LaRC 20-Inch Mach 6 Air Tunnel. Runs were made first at static angles-of-attack to obtain a baseline data set. Runs were then performed with continuous pitch-sweep ranges of ~8 deg (small sweep ranges were required to ensure short test time and adherence to the semi-infinite conduction assumption). Continuous pitch-sweep data acquisition was the testing method employed with the model at AEDC Tunnel 9, and this capability was first demonstrated in the LaRC 20-Inch Mach 6 Air Tunnel using a similarly designed model of the Mars Science Laboratory entry vehicle (Ref. 11) that was also tested in AEDC Tunnel 9. Finally, runs were conducted with squares of Kapton tape applied to the model to act as boundary layer trips; with the exception of one run, all these runs were also conducted with continuous pitch-sweeps of ~8-deg.

The test matrix is given in Table 2 with runs listed in chronological order. In Table 3, these runs are sorted into static angle-of-attack runs, continuous pitch-sweep runs, and runs with trips, and in each category, the runs are sorted first by angle-of-attack and then by free stream Reynolds number. Nominal conditions for each test point are given in these tables. These conditions remain constant over the length of a run, and run-to-run repeatability in this facility is excellent; therefore the nominal conditions can be used for all cases.

Computational Methods and Results

Flow field computations at the wind tunnel test conditions were performed using LAURA (Refs. 12 - 13). The LAURA (Langley Aerothermodynamic Upwind Relaxation Algorithm) code is a three-dimensional, finite-volume flow field solver that includes perfect-gas, equilibrium, and non-equilibrium chemistry models. The code can be used to solve the inviscid, viscous thin-layer Navier-Stokes, or full Navier-Stokes equations - for the current study the thin-layer model was employed. Time integration to steady-state in LAURA is accomplished through a point-relaxation scheme. Roe-averaging (Ref. 14) with Harten's entropy fix (Ref. 15) and Yee's Symmetric Total Variation Diminishing limiter (Ref. 16) is used for inviscid fluxes, and a second-order scheme is employed for viscous fluxes. In this study, a perfect-gas model was used with the appropriate gas parameters for nitrogen.

A structured, finite-volume, multiple-block grid (Figure 11) with a singularity-free nose was employed for the computations. The grid was comprised of 3.8 million points divided into 10 forebody heat-shield blocks and 28 aftbody/sting/wake blocks. Grid adaptation was performed (as per the method detailed in Ref. 13) to align the grid with the bow shock and to produce nominal wall cell Reynolds numbers on the order of 1. The wall boundary condition for the computations was a uniform 300 K temperature. Although the surface temperature rise over the duration of a run does have a small influence on the measured dimensional heat-transfer rates, data reporting and CFD comparisons in this document will be presented in terms of the Stanton number to eliminate this temperature dependence.

Computations were performed for each Reynolds number test condition at 4-deg angle-of-attack increments; laminar solutions were computed for all cases, and where appropriate turbulent solutions were computed. Because of the sparseness of gages on the aftbody of the model and the higher computational overhead of full-body computations, solutions with the wake and sting were performed only for a small subset of the tunnel conditions (selected α = 28-deg cases), while forebody-only computations were performed for all of the cases. The turbulent computations were performed using the algebraic Cebeci-Smith turbulence model (Ref. 17).

Results from the computations are shown in Figure 12 - Figure 17. In these figures, forebody centerline values are plotted for the boundary layer quantities Re_θ, Re_θ/M_e, δ, θ, the dimensional pressure, p_w, the dimensional heating at a uniform 300 K wall temperature q_{300}, the non-dimensional Stanton number, St, and the non-dimensional heating correlation parameters $St \times (Re_{\infty,D})^{1/2}$ and $St \times (Re_{\infty,D})^{1/5}$ for laminar and turbulent flow, respectively.

Results, Analysis, and Comparisons

Continuous Pitch-Sweep Validation

One of the purposes of this test was to validate the acquisition of heating data in continuous pitch sweep mode as was done during the test of this model at AEDC Tunnel 9. Therefore, runs were performed at static pitch intervals of 4-deg from α = 16-deg to α = 32 deg at each Reynolds number and then continuous pitch-sweep runs were made over the intervals of 16-24 deg and 24-32 deg at each Reynolds number. Comparisons of selected cases are presented in terms of Stanton number in Figure 18. The differences between static and continuous pitch-sweep runs were no more than a few percent, which was well within the expected experimental uncertainties of the measurements. These results were taken as successful validation of this continuous pitch-sweep data acquisition technique in LaRC hypersonic tunnels. It should be noted however that this success was obtained only after experience in previous testing of a similarly-instrumented model (Ref. 11) showed that the total run time (and thus the range of the pitch-sweep) had to be limited to only a few seconds (or about 8-deg of pitch-sweep) in order to prevent heat-conduction into the model from reaching the interior surface and violating the constant-temperature back-face assumption, as well as to minimize lateral conduction effects that violate the one-dimensional conduction assumption.

Reynolds Number Trends

Free-stream Reynolds number effects on centerline heating distributions are presented in Figure 19 to Figure 27. Forebody and aftbody data are presented on separate plots since the aftbody heating rates were approximately an order of magnitude lower than those on the forebody. These plots are ordered by angle-of-attack. Continuous and fixed pitch runs are shown separately to make the plots more readable although no significant differences between the two modes were apparent.

These data were plotted in terms of the non-dimensional heating parameter $St\times(Re_{\infty,D})^{1/2}$. For compressible, flat-plate boundary-layer theory (e.g. Ref. 18), it can be shown that this parameter is a weakly-varying function of M_∞ and the temperature ratio T_w/T_e for laminar flow. For a non-similar flow such as that over the CEV model, this parameter still remains nearly constant at given location on the body for constant Mach number and angle-of-attack as the free stream Reynolds number is varied. Thus, non-laminar behavior, i.e. transition onset and turbulent growth, can be identified from these plots for each Mach-α condition. The only condition at which transition on the leeside of the heat-shield was notable was at the highest Reynolds number of 7.1×10^6 /ft ($Re_{\infty,D} = 4.3\times10^6$). The wind-side of the heat-shield remained laminar except around the stagnation region where some increasing augmentation with Reynolds number observed. The crew module (aftbody) remained laminar for all test conditions.

Angle-of-Attack Trends

Angle-of-attack effects on the centerline heating distribution are shown in Figure 28 to Figure 34. Forebody and aftbody data are again presented on separate plots since the aftbody heating rates were approximately an order of magnitude lower than those on the forebody. The data shown were obtained during the continuous pitch-sweep runs with angle-of-attack ranges of 16-deg to 24-deg or 24-deg to 32-deg. There was no unexpected behavior with respect to angle-of-attack; the leeside heating decreased with increasing α and the wind-side heating increased.

Boundary-Layer Trip Effects

Heat-shield data from runs with boundary layer trips on the model are presented in Figure 35 to Figure 39 and crew module (aftbody) data are shown in Figure 40. The data shown in these figures represent a brief preliminary screening of the effects of trips and this report is not meant to represent a comprehensive study of this subject. A subsequent, and much more detailed, trip-effects test was performed in the LaRC 20-Inch Mach 6 Air Tunnel with this model and these data are presented in Ref. 19. In the current study, it was found that the trips perturbed the heating above laminar levels at all test conditions and that the effects of trip height did not appear to be significant. At the lower test Reynolds numbers ($Re_{\infty,D} = 1.8\times10^6$ and 2.3×10^6), the trip effects on the boundary layer appeared to be diminishing downstream of the trips, which indicated that transitional behavior was not sustainable. At $Re_{\infty,D} = 3.4\times10^6$ transition was sustained along the leeside, and at $Re_{\infty,D} = 4.3\times10^6$ heating distributions appeared to approach fully-developed turbulent levels. There did not appear to be any effects on the crew module heating of trips on the heat-shield for any trip height or Reynolds numbers; i.e. the aftbody flow remained laminar.

Off-Centerline Data

In this report, the off-centerline data will not be discussed since the highest heating levels were generated along the centerline when the vehicle is at zero-deg of yaw, and there were no runs were performed with the vehicle yawed. However, these data are presented in a graphical format in Figure 41 to Figure 45 for the clean, no-trip runs and in Figure 46 to Figure 50 for the runs with trips. In each figure, a view of the forebody is shown with a colored symbol that shows the heating level at each gage location. These figures are organized by Mach number and angle-of-attack in order to show the effects of increasing free stream Reynolds number over the whole forebody. For the higher Reynolds numbers runs, and for the runs with trips, the images can be examined to estimate the spread of

transitional/turbulent flow over the heat shield.

Comparison of Data and Predictions

Comparisons of the experimental data with computational predictions for the forebody of the CEV model are shown in Figure 51 to Figure 56 for clean, no-trip runs. These figures are ordered by Reynolds number, and in each figure the data for all angle-of-attack at that Reynolds number are shown. Error bars on the data in these figures represent ±10% for consistency with the presentation in Ref. 2, although the actual experimental uncertainty has been estimated to be a slightly higher value of ±12%. In general, the laminar predictions and laminar experimental data matched to within this ±12% level, with the predictions generally being lower than the data. However, experimental data on the leeside of the model ($z/R > 0.0$) exceeded the laminar predictions due to natural boundary-layer transition at the higher test Reynolds numbers. Additionally, the experimental data in the stagnation region (z/R = -0.5 to -0.8, depending on angle of attack) exceeded the predictions by more than the expected uncertainty range for several of the higher Reynolds number cases. Similar augmentation of the stagnation region experimental heating data has been observed previously in other facilities and with different configurations (Refs. 20 - 22). Therefore it is thought to be a real, non-laminar or unsteady flow phenomenon, as opposed to an artifact of a particular test facility, instrumentation type, or vehicle configuration.

Comparisons of experimental data from runs with trips to laminar predictions are shown in Figure 57 to Figure 59. These plots also include fully-turbulent predictions for the $Re_{\infty,D} = 4.3\times10^6$ ($Re_\infty = 7.3\times10^6$/ft) condition. The plots are ordered by angle-of-attack and include the data from all Reynolds numbers and trip heights (including the no-trip case) for each α. For most cases, the heating levels downstream of the trips remained well below the predicted turbulent levels, which suggested that the flow was transitional. At the highest test Reynolds numbers of $Re_{\infty,D} = 3.4\times10^6$ and 4.3×10^6 the heating data downstream from the trips approached the predicted turbulent levels, however, the predictions were at least ~10% to 15% higher than the data. It is notable than comparisons between turbulent data and predictions for the model in the AEDC Tunnel 9 study (Refs. 2 and 3) generally did fall within the estimated experimental uncertainty. The greater differences in the current study suggest that the state of the tripped boundary layers was close to, but did not reach, sustained, fully-turbulent behavior. It is also possible that lateral conduction around the heat-shield edge to the aftbody caused some drop in the heating levels even for the short run times of this test

In Figure 60, these tripped data are re-plotted in terms of the turbulent correlation parameter $St\times(Re_{\infty,D})^{1/5}$ instead of the laminar parameter $St\times(Re_{\infty,D})^{1/2}$. For fully-turbulent conditions, the leeside distributions should show Reynolds-number independence. However, such behavior was evident only at the outboard of the leeside for the highest Reynolds numbers, which provides additional evidence that there was little, if any, fully-developed turbulence.

The lack of any effect of heat-shield trips on the crew module (aftbody) flow is demonstrated in Figure 61 and Figure 62. For both smooth-body and tripped cases, the data on the windward side ($z/R < 0$) were in close agreement with predicted laminar levels. Note that large areas of the leeside flow on the aftbody were likely separated and unsteady, so the comparisons shown with the steady, laminar predictions should not be considered as definitive.

Comparison with other CEV Heating Data Sets

As noted previously, additional convective heating data have been obtained on the CEV configuration in both this facility and in the AEDC Tunnel 9. Data were obtained in the LaRC 20-Inch Mach 6 Air Tunnel (Ref. 5) using the global, two-color phosphor technique. Data were obtained in AEDC Tunnel 9 (Refs. 2 and 3) using the same wind tunnel model as in the current test.

Comparisons with the previous LaRC Mach 6 data (Test 6917) are shown in Figure 63 to Figure 67 for smooth-body cases and in Figure 68 to Figure 70 for cases with trips. In the smooth-body comparisons, a reference "uncertainty" of ±10% is shown for both coaxial thermocouple and thermographic phosphor data to simplify the plots although the true uncertainties are in ±10% to 20% range. In general, the laminar phosphor data were ~5% lower than the coaxial thermocouple data, which was a reasonable comparison given the higher uncertainties inherent to each technique. For the tripped data comparisons, the phosphor data were instead ~10% to 20% higher than the coaxial thermocouple data, which put them into closer agreement with turbulent predictions. The cause for the difference in comparisons between smooth and tripped cases has not been resolved. One likely hypothesis is that the inherently rougher surface of the phosphor-coated ceramic model helped to sustain and broaden boundary-layer transition and turbulence downstream of the trips more than that of the metallic surface of the coaxial thermocouple model.

A sample comparison of data obtained with the thermocouple model in the AEDC Tunnel 9 and in the LaRC 20-Inch Mach 6 Air Tunnel, and also the thermographic phosphor model data (LaRC Test 6917) is shown in Figure 71. While each of the four data sets (the Tunnel 9 Mach 8 and Mach 10 nozzle data and the Mach 6 coaxial gage and phosphor data) showed internal Reynolds number independence (for laminar data), they did not match each other. The reason for this difference was the use of a Stanton number based on total enthalpy, as defined in Eq. (1), which does not account for the influence of differing total enthalpy levels.

$$(1)\quad St \times \left(\mathrm{Re}_{\infty,D}\right)^{1/2} = \frac{q}{\rho_\infty U_\infty \left(H_0 - H_w\right)} \left(\frac{\rho_\infty U_\infty D}{\mu_\infty}\right)^{1/2} = \frac{q}{\rho_\infty U_\infty \left[\left(H_\infty + U_\infty^2/2\right) - H_w\right]} \left(\frac{\rho_\infty U_\infty D}{\mu_\infty}\right)^{1/2}$$

For simplicity, this definition is typically used in the data reduction process in both facilities as it does not require the use of an adiabatic wall recovery factor which can be defined in different ways. However, in the current case, an adiabatic wall recovery factor equal to the square root of the Prandtl number, which is the definition for a flat plate (Ref. 18), can be employed as an approximation. If the data are recast in terms of this parameter as per Eq. (2), a close agreement can then be obtained for the laminar data as shown in Figure 72. Comparisons for α = 24-deg and α = 32-deg are also shown in this format in Figure 73and Figure 74. For all cases, some differences were still observed in the stagnation region. As noted in Refs. 2 and 3, is it was not clear if there any of the Mach 8 data were truly laminar, thus this the correlation would not be appropriate. In the case of the thermographic phosphor data from Test 6917, the differences were probably due to an approximation made in the use of Eq. (2). The original format of the phosphor data was the variable h/h_{FR}; in order to compute the Stanton number from these data, it was assumed that the wall temperature was 300 K, when in fact the true temperatures would have been somewhat higher, especially in the stagnation region.

$$(2)\quad St_{AW} \times \left(\mathrm{Re}_{\infty,D}\right)^{1/2} = \frac{q}{\rho_\infty U_\infty \left(H_{AW} - H_w\right)} \left(\frac{\rho_\infty U_\infty D}{\mu_\infty}\right)^{1/2} = \frac{q}{\rho_\infty U_\infty \left[\sqrt{\mathrm{Pr}}\left(H_\infty + U_\infty^2/2\right) - H_w\right]} \left(\frac{\rho_\infty U_\infty D}{\mu_\infty}\right)^{1/2}$$

Summary and Conclusions

A convective aeroheating test of a CEV model has been conducted in the LaRC 20-Inch Mach 6 Air Tunnel across a range of free stream Reynolds numbers from 2.0×10^6/ft to 7.3×10^6/ft at angles-of-attack from 16-deg to 32-deg. Laminar or transitional flow was produced naturally in this test, depending on the free stream conditions, and discrete boundary-layer trips were also use to produce transitional and (apparently) nearly fully-turbulent flow. Heating data were obtained from thermocouple measurements on the forebody heat-shield and aftbody of the model. CFD predictions for comparison with the data were made at the tunnel test conditions and for use in correlating the

heating data.

Comparisons between the laminar data and predictions were performed for all forebody test conditions and for a small subset (α = 28 deg) of the aftbody data and the agreement was generally found to be well within the expected experimental uncertainty of ±12%. This level of agreement was consistent with that observed in previous testing of the same model at AEDC Tunnel 9. For cases where transition was artificially produced using boundary-layer trips, fully or near-to-fully developed turbulent flow only appeared to be produced at the very highest test Reynolds number; for those conditions, predictions were generally 10% to 15% higher than the experimental data.

Comparisons between data acquired from static and continuous pitch-sweep runs compared to within the experimental uncertainty, which validated the use of continuous pitch-sweep data acquisition with thermocouples in this facility. Additionally, data sets from other tests of the CEV model using both thermocouples (at AEDC Tunnel 9) and phosphor thermography were shown to compare fairly well when the Stanton number was formulated in terms of the adiabatic recovery enthalpy instead of total enthalpy.

References

1. "NASA's Exploration Systems Architecture Study, Final Report," NASA TM-2005-214062, November, 2005.

2. Hollis, B. R., Horvath, T. J., Berger, K. T., Lillard, R. P., Kirk, B. S., Coblish, J. J., and Norris, J. D., "Experimental Investigation of Project Orion Crew Exploration Vehicle Aeroheating in AEDC Tunnel 9," NASA TP-2008-215547, December, 2008.

3. Hollis, B. R., Horvath, T. J., Berger, K. T., Coblish, J. J., Norris, J. D., Lillard, R. P, and Kirk, B. S., "Aeroheating Testing and Predictions for Project Orion CEV at Turbulent Conditions," AIAA Paper 2008-1226, 46th AIAA Aerospace Sciences Meeting and Exhibit, Reno, NV, Jan. 7-10, 2008.

4. Liechty, D. S., "Aerothermodynamic Testing of Protuberances and Penetrations on the NASA Cycle I Crew Exploration Vehicle Heat," AIAA Paper 2008-1240, 46th AIAA Aerospace Sciences Meeting and Exhibit, Reno, NV, Jan. 7-10, 2008.

5. Berger, K. T., "Aerothermodynamic Testing of the Cycle I Crew Exploration Vehicle Crew Module in the LaRC 20-Inch Mach 6 and 31-Inch Mach 10 Tunnels," AIAA Paper 2008-1225, 46th AIAA Aerospace Sciences Meeting and Exhibit, Reno, NV, Jan. 7-10, 2008.

6. Berry, S. A., Bouslog, S. A., Brauckmann, G. J. and Caram, J. M., "Shuttle Orbiter Experimental Boundary-Layer Transition Results with Isolated Roughness," *Journal of Spacecraft & Rocket*s, Vol. 35, No. 3, May-June 1998, pp. 241-248.

7. Coblish, J. J., and Davenport, A. H., "Recent Efforts at AEDC's Von Karman Facility and Hypervelocity Wind Tunnel 9 to Enhance Facility Compatibility", AIAA Paper 2002-2787, 22nd AIAA Aerodynamic Measurement Technology and Ground Testing Conference, June 24-26, 2002.

8. Burns, G. W., Scroger, M. G., Strouse, G. F., Croarkin, M. C., and Guthrie, W. F., "Temperature-Electromotive Force Reference Functions and Tables for the Letter-Designated Thermocouple Types Based on ITS-90," NIST Monograph 175, 1993.

9. Micol, J. R., "Langley Aerothermodynamic Facilities Complex: Enhancements and Testing Capabilities," AIAA Paper 1998-0147, 36th AIAA Aerospace Sciences Meeting & Exhibit, Reno, NV, Jan. 12-15, 1998.

10. Hollis, B. R., "User's Manual for the One-Dimensional Hypersonic Aero-Thermodynamic (1DHEAT) Data Reduction Code," NASA CR-4691, August 1995.

11. Hollis, B. R. and Collier, A. S., "Turbulent Aeroheating Testing of Mars Science Laboratory Entry Vehicle in Perfect-Gas Nitrogen," AIAA Paper 2007-1208, 45th AIAA Aerospace Sciences Meeting and Exhibit, Reno, NV, Jan. 8-11, 2007.

12. Gnoffo, P. A., "An Upwind-Biased, Point-Implicit Algorithm for Viscous, Compressible Perfect-Gas Flows," NASA TP-2953, February 1990.

13. Cheatwood, F. M., and Gnoffo, P. A., "User's Manual for the Langley Aerothermodynamic Upwind Relaxation Algorithm (LAURA)," NASA TM 4674, April, 1996.

14. Roe, P. L., "Approximate Riemann Solvers, Parameter Vectors and Difference Schemes," Journal of Computational Physics, Vol. 43, No. 2, 1981, pp. 357-372.

15. Harten, A., "High Resolution Schemes for Hyperbolic Conservation Laws," Journal of Computational Physics, Vol. 49, No. 3, 1983, pp. 357-393.

16. Yee, H. C., "On Symmetric and Upwind TVD Schemes," NASA TM 88325, 1990.

17. Cheatwood, F. M., and Thompson, R. A., "The Addition of Algebraic Turbulence Modeling to Program LAURA," NASA TM-107758, April 1993.

18. Anderson, J. D. Jr., *Hypersonic and High-Temperature Gas Dynamics*, McGraw-Hill Book Company, New York, 1989.

19. Amar, A. J., Calvert, N., Horvath, T. J., Hollis, B. R., Berger, K. T., and Berry, S. A., "Protuberance Boundary Layer Transition Test for Project Orion CEV at Mach 6," AIAA Paper 2008-1227, 46th AIAA Aerospace Sciences Meeting and Exhibit, Reno, NV, Jan. 7-10, 2008.

20. Hollis, B. R., Liechty, D. S., Wright, M. J., Holden, M. S., Wadhams, T. P., and MacLean, M., "Transition Onset and Turbulent Heating Measurements for the Mars Science Laboratory Entry Vehicle," AIAA Paper 2005-1437, 43rd Aerospace Sciences Meeting and Exhibit, Reno, NV, January 10-13, 2008.

21. Shimshi, J. P. and Walberg, G. D., "An Investigation of Aerodynamic Heating to Spherically Blunted Cones at Angle of Attack," AIAA Paper 1993-2764, 28th AIAA Thermophysics Conference, Orlando, FL, January 6-9, 1993.

22. Petersen, F., Server, D., and Carroll, H., "Heat Transfer and Pressure Distributions at M = 8 on 0.029 Scale Models of the Viking Entry Vehicle," NASA CR-132413, July 1972.

Table 1. Gage locations

Gage	x(m)	y(m)	z(m)	x/R	y/R	z/R	Local thickness (m)	Local radius (m)	Location
1	0.0175	-0.0845	0.0000	0.1971	-0.9500	0.0000	0.0062	0.0089	Heat Shield
2	0.0164	-0.0622	-0.0533	0.1841	-0.7000	-0.6000	0.0067	0.2134	Heat Shield
3	0.0105	-0.0622	0.0222	0.1180	-0.7000	0.2500	0.0095	0.2134	Heat Shield
4	0.0138	-0.0356	-0.0667	0.1556	-0.4000	-0.7500	0.0093	0.2134	Heat Shield
5	0.0030	-0.0356	0.0000	0.0336	-0.4000	0.0000	0.0095	0.2134	Heat Shield
6	0.0056	-0.0356	0.0333	0.0635	-0.4000	0.3750	0.0095	0.2134	Heat Shield
7	0.0138	-0.0356	0.0667	0.1556	-0.4000	0.7500	0.0093	0.2134	Heat Shield
8	0.0175	-0.0133	0.0834	0.1971	-0.1500	0.9379	0.0062	0.0089	Heat Shield
9	0.0051	-0.0133	-0.0445	0.0575	-0.1500	-0.5000	0.0095	0.2134	Heat Shield
10	0.0016	-0.0133	0.0222	0.0178	-0.1500	0.2500	0.0095	0.2134	Heat Shield
11	0.0051	-0.0133	0.0445	0.0575	-0.1500	0.5000	0.0095	0.2134	Heat Shield
12	0.0111	-0.0133	0.0667	0.1251	-0.1500	0.7500	0.0095	0.2134	Heat Shield
13	0.0175	0.0000	-0.0845	0.1971	0.0000	-0.9500	0.0062	0.0089	Centerline Heat Shield
14	0.0156	0.0000	-0.0800	0.1751	0.0000	-0.9000	0.0075	0.2134	Centerline Heat Shield
15	0.0138	0.0000	-0.0756	0.1556	0.0000	-0.8500	0.0093	0.2134	Centerline Heat Shield
16	0.0122	0.0000	-0.0711	0.1373	0.0000	-0.8000	0.0095	0.2134	Centerline Heat Shield
17	0.0107	0.0000	-0.0667	0.1202	0.0000	-0.7500	0.0095	0.2134	Centerline Heat Shield
18	0.0093	0.0000	-0.0622	0.1043	0.0000	-0.7000	0.0095	0.2134	Centerline Heat Shield
19	0.0080	0.0000	-0.0578	0.0897	0.0000	-0.6500	0.0095	0.2134	Centerline Heat Shield
20	0.0068	0.0000	-0.0533	0.0762	0.0000	-0.6000	0.0095	0.2134	Centerline Heat Shield
21	0.0057	0.0000	-0.0489	0.0639	0.0000	-0.5500	0.0095	0.2134	Centerline Heat Shield
22	0.0047	0.0000	-0.0445	0.0527	0.0000	-0.5000	0.0095	0.2134	Centerline Heat Shield
23	0.0038	0.0000	-0.0400	0.0426	0.0000	-0.4500	0.0095	0.2134	Centerline Heat Shield
24	0.0030	0.0000	-0.0356	0.0336	0.0000	-0.4000	0.0095	0.2134	Centerline Heat Shield
25	0.0023	0.0000	-0.0311	0.0257	0.0000	-0.3500	0.0095	0.2134	Centerline Heat Shield
26	0.0017	0.0000	-0.0267	0.0188	0.0000	-0.3000	0.0095	0.2134	Centerline Heat Shield
27	0.0012	0.0000	-0.0222	0.0131	0.0000	-0.2500	0.0095	0.2134	Centerline Heat Shield
28	0.0003	0.0000	-0.0111	0.0033	0.0000	-0.1251	0.0100	0.2134	Centerline Heat Shield
29	0.0000	0.0000	0.0000	0.0000	0.0000	0.0000	0.0150	0.2134	Centerline Heat Shield
30	0.0000	0.0000	0.0044	0.0005	0.0000	0.0500	0.0095	0.2134	Centerline Heat Shield
31	0.0002	0.0000	0.0089	0.0021	0.0000	0.1000	0.0095	0.2134	Centerline Heat Shield
32	0.0004	0.0000	0.0133	0.0047	0.0000	0.1500	0.0095	0.2134	Centerline Heat Shield
33	0.0007	0.0000	0.0178	0.0083	0.0000	0.2000	0.0095	0.2134	Centerline Heat Shield
34	0.0012	0.0000	0.0222	0.0131	0.0000	0.2500	0.0095	0.2134	Centerline Heat Shield
35	0.0017	0.0000	0.0267	0.0188	0.0000	0.3000	0.0095	0.2134	Centerline Heat Shield
36	0.0023	0.0000	0.0311	0.0257	0.0000	0.3500	0.0095	0.2134	Centerline Heat Shield
37	0.0030	0.0000	0.0356	0.0336	0.0000	0.4000	0.0095	0.2134	Centerline Heat Shield
38	0.0038	0.0000	0.0400	0.0426	0.0000	0.4500	0.0095	0.2134	Centerline Heat Shield
39	0.0047	0.0000	0.0445	0.0527	0.0000	0.5000	0.0095	0.2134	Centerline Heat Shield
40	0.0057	0.0000	0.0489	0.0639	0.0000	0.5500	0.0095	0.2134	Centerline Heat Shield
41	0.0068	0.0000	0.0533	0.0762	0.0000	0.6000	0.0095	0.2134	Centerline Heat Shield
42	0.0080	0.0000	0.0578	0.0897	0.0000	0.6500	0.0095	0.2134	Centerline Heat Shield
43	0.0093	0.0000	0.0622	0.1043	0.0000	0.7000	0.0095	0.2134	Centerline Heat Shield
44	0.0107	0.0000	0.0667	0.1202	0.0000	0.7500	0.0095	0.2134	Centerline Heat Shield
45	0.0122	0.0000	0.0711	0.1373	0.0000	0.8000	0.0095	0.2134	Centerline Heat Shield
46	0.0138	0.0000	0.0756	0.1556	0.0000	0.8500	0.0093	0.2134	Centerline Heat Shield
47	0.0156	0.0000	0.0800	0.1751	0.0000	0.9000	0.0075	0.2134	Centerline Heat Shield
48	0.0175	0.0000	0.0845	0.1971	0.0000	0.9500	0.0062	0.0089	Centerline Heat Shield
49	0.0175	0.0133	-0.0834	0.1971	0.1500	-0.9379	0.0062	0.0089	Heat Shield
50	0.0111	0.0133	-0.0667	0.1251	0.1500	-0.7500	0.0095	0.2134	Heat Shield
51	0.0051	0.0133	-0.0445	0.0575	0.1500	-0.5000	0.0095	0.2134	Heat Shield
52	0.0004	0.0133	0.0000	0.0047	0.1500	0.0000	0.0112	0.2134	Heat Shield
53	0.0016	0.0133	0.0222	0.0178	0.1500	0.2500	0.0095	0.2134	Heat Shield
54	0.0030	0.0133	0.0333	0.0342	0.1500	0.3750	0.0095	0.2134	Heat Shield
55	0.0051	0.0133	0.0445	0.0575	0.1500	0.5000	0.0095	0.2134	Heat Shield
56	0.0078	0.0133	0.0556	0.0882	0.1500	0.6250	0.0095	0.2134	Heat Shield

Gage	x(m)	y(m)	z(m)	x/R	y/R	z/R	Local thickness (m)	Local radius (m)	Location
57	0.0111	0.0133	0.0667	0.1251	0.1500	0.7500	0.0095	0.2134	Heat Shield
58	0.0143	0.0133	0.0756	0.1606	0.1500	0.8500	0.0088	0.2134	Heat Shield
59	0.0175	0.0133	0.0834	0.1971	0.1500	0.9379	0.0062	0.0089	Heat Shield
60	0.0014	0.0244	0.0000	0.0158	0.2750	0.0000	0.0095	0.2134	Heat Shield
61	0.0026	0.0244	0.0222	0.0289	0.2750	0.2500	0.0095	0.2134	Heat Shield
62	0.0040	0.0244	0.0333	0.0455	0.2750	0.3750	0.0095	0.2134	Heat Shield
63	0.0061	0.0244	0.0445	0.0688	0.2750	0.5000	0.0095	0.2134	Heat Shield
64	0.0088	0.0244	0.0556	0.0992	0.2750	0.6250	0.0095	0.2134	Heat Shield
65	0.0122	0.0244	0.0667	0.1369	0.2750	0.7500	0.0095	0.2134	Heat Shield
66	0.0153	0.0244	0.0756	0.1725	0.2750	0.8500	0.0077	0.2134	Heat Shield
67	0.0138	0.0356	-0.0667	0.1556	0.4000	-0.7500	0.0093	0.2134	Heat Shield
68	0.0056	0.0356	-0.0333	0.0635	0.4000	-0.3750	0.0096	0.2134	Heat Shield
69	0.0032	0.0356	-0.0089	0.0357	0.4000	-0.1000	0.0112	0.2134	Heat Shield
70	0.0030	0.0356	0.0000	0.0336	0.4000	0.0000	0.0095	0.2134	Heat Shield
71	0.0042	0.0356	0.0222	0.0468	0.4000	0.2500	0.0095	0.2134	Heat Shield
72	0.0056	0.0356	0.0333	0.0635	0.4000	0.3750	0.0095	0.2134	Heat Shield
73	0.0077	0.0356	0.0445	0.0870	0.4000	0.5000	0.0095	0.2134	Heat Shield
74	0.0105	0.0356	0.0556	0.1176	0.4000	0.6250	0.0095	0.2134	Heat Shield
75	0.0138	0.0356	0.0667	0.1556	0.4000	0.7500	0.0093	0.2134	Heat Shield
76	0.0069	0.0489	0.0222	0.0773	0.5500	0.2500	0.0095	0.2134	Heat Shield
77	0.0105	0.0489	0.0445	0.1180	0.5500	0.5000	0.0095	0.2134	Heat Shield
78	0.0164	0.0622	-0.0533	0.1841	0.7000	-0.6000	0.0067	0.2134	Heat Shield
79	0.0093	0.0622	0.0000	0.1043	0.7000	0.0000	0.0095	0.2134	Heat Shield
80	0.0105	0.0622	0.0222	0.1180	0.7000	0.2500	0.0095	0.2134	Heat Shield
81	0.0164	0.0622	0.0533	0.1841	0.7000	0.6000	0.0067	0.2134	Heat Shield
82	0.0175	0.0845	0.0000	0.1971	0.9500	0.0000	0.0062	0.0089	Heat Shield
83	0.0508	-0.0445	-0.0595	0.5711	-0.5000	-0.6688	0.0158	0.0743	Aft body, wind-side
84	0.0508	-0.0222	-0.0708	0.5711	-0.2500	-0.7967	0.0158	0.0743	Aft body, wind-side
85	0.0508	0.0000	-0.0742	0.5711	0.0000	-0.8351	0.0158	0.0743	Aft body, wind-side
86	0.0508	0.0222	-0.0708	0.5711	0.2500	-0.7967	0.0158	0.0743	Aft body, wind-side
87	0.0508	0.0445	-0.0595	0.5711	0.5000	-0.6688	0.0158	0.0743	Aft body, wind-side
88	0.0698	-0.0445	-0.0435	0.7849	-0.5000	-0.4890	0.0095	0.0622	Aft body, wind-side
89	0.0698	-0.0222	-0.0581	0.7849	-0.2500	-0.6530	0.0095	0.0622	Aft body, wind-side
90	0.0698	0.0000	-0.0622	0.7849	0.0000	-0.6992	0.0095	0.0622	Aft body, wind-side
91	0.0698	0.0222	-0.0581	0.7849	0.2500	-0.6530	0.0095	0.0622	Aft body, wind-side
92	0.0698	0.0445	-0.0435	0.7849	0.5000	-0.4889	0.0095	0.0622	Aft body, wind-side
93	0.0975	0.0000	-0.0445	1.0969	0.0000	-0.5002	0.0095	0.0487	Aft body, wind-side
94	0.0508	-0.0222	0.0708	0.5711	-0.2500	0.7967	0.0158	0.0743	Aft body, leeside
95	0.0508	0.0000	0.0742	0.5711	0.0000	0.8351	0.0158	0.0743	Aft body, leeside
96	0.0508	0.0222	0.0708	0.5711	0.2500	0.7967	0.0158	0.0743	Aft body, leeside
97	0.0698	-0.0222	0.0581	0.7849	-0.2500	0.6530	0.0095	0.0622	Aft body, leeside
98	0.0698	0.0000	0.0622	0.7849	0.0000	0.7000	0.0095	0.0622	Aft body, leeside
99	0.0698	0.0222	0.0581	0.7849	0.2500	0.6530	0.0095	0.0622	Aft body, leeside
100	0.0975	0.0000	0.0445	1.0969	0.0000	0.5000	0.0095	0.0487	Aft body, leeside
101	0.1087	0.0000	0.0373	1.2233	0.0000	0.4200	0.0182	0.0422	Aft body, leeside

Table 2. Test 6931 Run Matrix (Chronological)

Run	α (deg)	Re_∞ (1/ft)	Re_∞ (1/m)	$Re_{\infty,D}$	Mach	P_∞ (Pa)	T_∞ (K)	ρ_∞ (kg/m^3)	U_∞ (m/s)	H_0-H_{300K} (J/kg)	Trips
1	28	2.01E+06	6.61E+06	1.17E+06	6.0	552	61.9	3.103E-02	946.0	2.090E+05	clean
2	28	3.02E+06	9.91E+06	1.76E+06	6.0	841	62.6	4.680E-02	950.6	2.140E+05	clean
3	28	3.91E+06	1.28E+07	2.28E+06	6.0	1109	63.4	6.103E-02	956.2	2.200E+05	clean
4	28	5.09E+06	1.67E+07	2.97E+06	6.0	1446	63.5	7.956E-02	956.0	2.200E+05	clean
5	28	5.89E+06	1.93E+07	3.44E+06	6.0	1677	63.4	9.220E-02	955.9	2.200E+05	clean
6	28	7.37E+06	2.42E+07	4.30E+06	6.0	2132	64.2	1.160E-01	960.4	2.249E+05	clean
7	32	2.01E+06	6.61E+06	1.17E+06	6.0	552	61.9	3.103E-02	946.0	2.090E+05	clean
8	32	3.02E+06	9.91E+06	1.76E+06	6.0	841	62.6	4.680E-02	950.6	2.140E+05	clean
9	32	3.91E+06	1.28E+07	2.28E+06	6.0	1109	63.4	6.103E-02	956.2	2.200E+05	clean
10	32	5.09E+06	1.67E+07	2.97E+06	6.0	1446	63.5	7.956E-02	956.0	2.200E+05	clean
11	32	5.89E+06	1.93E+07	3.44E+06	6.0	1677	63.4	9.220E-02	955.9	2.200E+05	clean
12	32	7.37E+06	2.42E+07	4.30E+06	6.0	2132	64.2	1.160E-01	960.4	2.249E+05	clean
13	24	3.91E+06	1.28E+07	2.28E+06	6.0	1109	63.4	6.103E-02	956.2	2.200E+05	clean
14	24	5.09E+06	1.67E+07	2.97E+06	6.0	1446	63.5	7.956E-02	956.0	2.200E+05	clean
15	24	5.89E+06	1.93E+07	3.44E+06	6.0	1677	63.4	9.220E-02	955.9	2.200E+05	clean
16	24	7.37E+06	2.42E+07	4.30E+06	6.0	2132	64.2	1.160E-01	960.4	2.249E+05	clean
17	24	1.01E+06	3.30E+06	5.89E+05	5.9	292	63.7	1.600E-02	943.7	2.088E+05	clean
18	24	3.91E+06	1.28E+07	2.28E+06	6.0	1109	63.4	6.103E-02	956.2	2.200E+05	clean
19	24	2.01E+06	6.61E+06	1.17E+06	6.0	552	61.9	3.103E-02	946.0	2.090E+05	clean
20	0	3.02E+06	9.91E+06	1.76E+06	6.0	841	62.6	4.680E-02	950.6	2.140E+05	clean
21	24	3.02E+06	9.91E+06	1.76E+06	6.0	841	62.6	4.680E-02	950.6	2.140E+05	clean
22	28	1.01E+06	3.30E+06	5.89E+05	5.9	292	63.7	1.600E-02	943.7	2.088E+05	clean
23	32	1.01E+06	3.30E+06	5.89E+05	5.9	292	63.7	1.600E-02	943.7	2.088E+05	clean
24	28	2.01E+06	6.61E+06	1.17E+06	6.0	552	61.9	3.103E-02	946.0	2.090E+05	clean
25	20	2.01E+06	6.61E+06	1.17E+06	6.0	552	61.9	3.103E-02	946.0	2.090E+05	clean
26	20	3.02E+06	9.91E+06	1.76E+06	6.0	841	62.6	4.680E-02	950.6	2.140E+05	clean
27	20	1.01E+06	3.30E+06	5.89E+05	5.9	292	63.7	1.600E-02	943.7	2.088E+05	clean
28	20	1.01E+06	3.30E+06	5.89E+05	5.9	292	63.7	1.600E-02	943.7	2.088E+05	clean
29	20	3.91E+06	1.28E+07	2.28E+06	6.0	1109	63.4	6.103E-02	956.2	2.200E+05	clean
30	20	5.09E+06	1.67E+07	2.97E+06	6.0	1446	63.5	7.956E-02	956.0	2.200E+05	clean
31	20	5.89E+06	1.93E+07	3.44E+06	6.0	1677	63.4	9.220E-02	955.9	2.200E+05	clean
32	20	7.37E+06	2.42E+07	4.30E+06	6.0	2132	64.2	1.160E-01	960.4	2.249E+05	clean
33	24-32	3.02E+06	9.91E+06	1.76E+06	6.0	841	62.6	4.680E-02	950.6	2.140E+05	clean
34	24-32	3.91E+06	1.28E+07	2.28E+06	6.0	1109	63.4	6.103E-02	956.2	2.200E+05	clean
~~35~~	~~24~~	~~5.09E+06~~	~~1.67E+07~~	~~2.97E+06~~	~~6.0~~	~~1446~~	~~63.5~~	~~7.956E-02~~	~~956.0~~	~~2.200E+05~~	bad run
36	24-32	5.09E+06	1.67E+07	2.97E+06	6.0	1446	63.5	7.956E-02	956.0	2.200E+05	clean
37	24-32	5.89E+06	1.93E+07	3.44E+06	6.0	1677	63.4	9.220E-02	955.9	2.200E+05	clean
38	24-32	7.37E+06	2.42E+07	4.30E+06	6.0	2132	64.2	1.160E-01	960.4	2.249E+05	clean
39	16-24	3.02E+06	9.91E+06	1.76E+06	6.0	841	62.6	4.680E-02	950.6	2.140E+05	clean
40	16-24	3.91E+06	1.28E+07	2.28E+06	6.0	1109	63.4	6.103E-02	956.2	2.200E+05	clean
41	16-24	5.09E+06	1.67E+07	2.97E+06	6.0	1446	63.5	7.956E-02	956.0	2.200E+05	clean
42	16-24	5.89E+06	1.93E+07	3.44E+06	6.0	1677	63.4	9.220E-02	955.9	2.200E+05	Clean
43	16-24	7.37E+06	2.42E+07	4.30E+06	6.0	2132	64.2	1.160E-01	960.4	2.249E+05	Clean
44	23-32	7.37E+06	2.42E+07	4.30E+06	6.0	2132	64.2	1.160E-01	960.4	2.249E+05	0.0115 inch
45	23-32	5.89E+06	1.93E+07	3.44E+06	6.0	1677	63.4	9.220E-02	955.9	2.200E+05	0.0115 inch
46	23-32	5.09E+06	1.67E+07	2.97E+06	6.0	1446	63.5	7.956E-02	956.0	2.200E+05	0.0115 inch
47	23-32	3.91E+06	1.28E+07	2.28E+06	6.0	1109	63.4	6.103E-02	956.2	2.200E+05	0.0115 inch
48	23-32	3.02E+06	9.91E+06	1.76E+06	6.0	841	62.6	4.680E-02	950.6	2.140E+05	0.0115 inch
49	23-32	7.37E+06	2.42E+07	4.30E+06	6.0	2132	64.2	1.160E-01	960.4	2.249E+05	0.0045 inch
50	24-32	5.89E+06	1.93E+07	3.44E+06	6.0	1677	63.4	9.220E-02	955.9	2.200E+05	0.0045 inch
51	24-32	5.09E+06	1.67E+07	2.97E+06	6.0	1446	63.5	7.956E-02	956.0	2.200E+05	0.0045 inch
52	24-32	3.91E+06	1.28E+07	2.28E+06	6.0	1109	63.4	6.103E-02	956.2	2.200E+05	0.0045 inch
53	24-32	3.02E+06	9.91E+06	1.76E+06	6.0	841	62.6	4.680E-02	950.6	2.140E+05	0.0045 inch
54	24-32	7.37E+06	2.42E+07	4.30E+06	6.0	2132	64.2	1.160E-01	960.4	2.249E+05	0.0065 inch
55	24-32	5.89E+06	1.93E+07	3.44E+06	6.0	1677	63.4	9.220E-02	955.9	2.200E+05	0.0065 inch
56	24-32	5.09E+06	1.67E+07	2.97E+06	6.0	1446	63.5	7.956E-02	956.0	2.200E+05	0.0065 inch
57	24-32	3.91E+06	1.28E+07	2.28E+06	6.0	1109	63.4	6.103E-02	956.2	2.200E+05	0.0065 inch

Run	α (deg)	Re_∞ (1/ft)	Re_∞ (1/m)	$Re_{\infty,D}$	Mach	P_∞ (Pa)	T_∞ (K)	ρ_∞ (kg/m^3)	U_∞ (m/s)	H_0-H_{300K} (J/kg)	Trips
58	24-32	3.02E+06	9.91E+06	1.76E+06	6.0	841	62.6	4.680E-02	950.6	2.140E+05	0.0065 inch
59	24-32	2.01E+06	6.61E+06	1.17E+06	6.0	552	61.9	3.103E-02	946.0	2.090E+05	0.0065 inch
60	23-32	7.37E+06	2.42E+07	4.30E+06	6.0	2132	64.2	1.160E-01	960.4	2.249E+05	0.0115 inch
61	15-24	7.37E+06	2.42E+07	4.30E+06	6.0	2132	64.2	1.160E-01	960.4	2.249E+05	0.0045 inch
62	15-24	5.89E+06	1.93E+07	3.44E+06	6.0	1677	63.4	9.220E-02	955.9	2.200E+05	0.0045 inch
63	15-24	7.37E+06	2.42E+07	4.30E+06	6.0	2132	64.2	1.160E-01	960.4	2.249E+05	0.0115 inch
64	15-24	5.89E+06	1.93E+07	3.44E+06	6.0	1677	63.4	9.220E-02	955.9	2.200E+05	0.0115 inch
65	15-24	5.09E+06	1.67E+07	2.97E+06	6.0	1446	63.5	7.956E-02	956.0	2.200E+05	0.0115 inch
66	15-24	3.91E+06	1.28E+07	2.28E+06	6.0	1109	63.4	6.103E-02	956.2	2.200E+05	0.0115 inch
67	28	7.37E+06	2.42E+07	4.30E+06	6.0	2132	64.2	1.160E-01	960.4	2.249E+05	0.0115 inch
68	32-23	7.37E+06	2.42E+07	4.30E+06	6.0	2132	64.2	1.160E-01	960.4	2.249E+05	0.0115 inch

Table 3. Test 6931 Run Matrix (Sorted)

Run	α (deg)	Re_∞ (1/ft)	Re_∞ (1/m)	$Re_{\infty,D}$	Mach	P_∞ (Pa)	T_∞ (K)	ρ_∞ (kg/m^3)	U_∞ (m/s)	H_0-H_{300K} (J/kg)	Trips
Clean-body, static angle-of-attack runs											
20	0	3.02E+06	9.91E+06	1.76E+06	6.0	841	62.6	4.680E-02	950.6	2.140E+05	clean
27	20	1.01E+06	3.30E+06	5.89E+05	5.9	292	63.7	1.600E-02	943.7	2.088E+05	clean
28	20	1.01E+06	3.30E+06	5.89E+05	5.9	292	63.7	1.600E-02	943.7	2.088E+05	clean
25	20	2.01E+06	6.61E+06	1.17E+06	6.0	552	61.9	3.103E-02	946.0	2.090E+05	clean
26	20	3.02E+06	9.91E+06	1.76E+06	6.0	841	62.6	4.680E-02	950.6	2.140E+05	clean
29	20	3.91E+06	1.28E+07	2.28E+06	6.0	1109	63.4	6.103E-02	956.2	2.200E+05	clean
30	20	5.09E+06	1.67E+07	2.97E+06	6.0	1446	63.5	7.956E-02	956.0	2.200E+05	clean
31	20	5.89E+06	1.93E+07	3.44E+06	6.0	1677	63.4	9.220E-02	955.9	2.200E+05	clean
32	20	7.37E+06	2.42E+07	4.30E+06	6.0	2132	64.2	1.160E-01	960.4	2.249E+05	clean
17	24	1.01E+06	3.30E+06	5.89E+05	5.9	292	63.7	1.600E-02	943.7	2.088E+05	clean
19	24	2.01E+06	6.61E+06	1.17E+06	6.0	552	61.9	3.103E-02	946.0	2.090E+05	clean
21	24	3.02E+06	9.91E+06	1.76E+06	6.0	841	62.6	4.680E-02	950.6	2.140E+05	clean
13	24	3.91E+06	1.28E+07	2.28E+06	6.0	1109	63.4	6.103E-02	956.2	2.200E+05	clean
18	24	3.91E+06	1.28E+07	2.28E+06	6.0	1109	63.4	6.103E-02	956.2	2.200E+05	clean
14	24	5.09E+06	1.67E+07	2.97E+06	6.0	1446	63.5	7.956E-02	956.0	2.200E+05	clean
15	24	5.89E+06	1.93E+07	3.44E+06	6.0	1677	63.4	9.220E-02	955.9	2.200E+05	clean
16	24	7.37E+06	2.42E+07	4.30E+06	6.0	2132	64.2	1.160E-01	960.4	2.249E+05	clean
22	28	1.01E+06	3.30E+06	5.89E+05	5.9	292	63.7	1.600E-02	943.7	2.088E+05	clean
1	28	2.01E+06	6.61E+06	1.17E+06	6.0	552	61.9	3.103E-02	946.0	2.090E+05	clean
24	28	2.01E+06	6.61E+06	1.17E+06	6.0	552	61.9	3.103E-02	946.0	2.090E+05	clean
2	28	3.02E+06	9.91E+06	1.76E+06	6.0	841	62.6	4.680E-02	950.6	2.140E+05	clean
3	28	3.91E+06	1.28E+07	2.28E+06	6.0	1109	63.4	6.103E-02	956.2	2.200E+05	clean
4	28	5.09E+06	1.67E+07	2.97E+06	6.0	1446	63.5	7.956E-02	956.0	2.200E+05	clean
5	28	5.89E+06	1.93E+07	3.44E+06	6.0	1677	63.4	9.220E-02	955.9	2.200E+05	clean
6	28	7.37E+06	2.42E+07	4.30E+06	6.0	2132	64.2	1.160E-01	960.4	2.249E+05	clean
23	32	1.01E+06	3.30E+06	5.89E+05	5.9	292	63.7	1.600E-02	943.7	2.088E+05	clean
7	32	2.01E+06	6.61E+06	1.17E+06	6.0	552	61.9	3.103E-02	946.0	2.090E+05	clean
8	32	3.02E+06	9.91E+06	1.76E+06	6.0	841	62.6	4.680E-02	950.6	2.140E+05	clean
9	32	3.91E+06	1.28E+07	2.28E+06	6.0	1109	63.4	6.103E-02	956.2	2.200E+05	clean
10	32	5.09E+06	1.67E+07	2.97E+06	6.0	1446	63.5	7.956E-02	956.0	2.200E+05	clean
11	32	5.89E+06	1.93E+07	3.44E+06	6.0	1677	63.4	9.220E-02	955.9	2.200E+05	clean
12	32	7.37E+06	2.42E+07	4.30E+06	6.0	2132	64.2	1.160E-01	960.4	2.249E+05	clean
Clean-body, continuous pitch sweep runs											
~~35~~	~~24~~	~~5.09E+06~~	~~1.67E+07~~	2.97E+06	~~6.0~~	~~1446~~	~~63.5~~	~~7.956E-02~~	~~956.0~~	~~2.200E+05~~	Bad run
39	16-24	3.02E+06	9.91E+06	1.76E+06	6.0	841	62.6	4.680E-02	950.6	2.140E+05	clean
40	16-24	3.91E+06	1.28E+07	2.28E+06	6.0	1109	63.4	6.103E-02	956.2	2.200E+05	clean
41	16-24	5.09E+06	1.67E+07	2.97E+06	6.0	1446	63.5	7.956E-02	956.0	2.200E+05	clean
42	16-24	5.89E+06	1.93E+07	3.44E+06	6.0	1677	63.4	9.220E-02	955.9	2.200E+05	clean
43	16-24	7.37E+06	2.42E+07	4.30E+06	6.0	2132	64.2	1.160E-01	960.4	2.249E+05	clean
33	24-32	3.02E+06	9.91E+06	1.76E+06	6.0	841	62.6	4.680E-02	950.6	2.140E+05	clean
34	24-32	3.91E+06	1.28E+07	2.28E+06	6.0	1109	63.4	6.103E-02	956.2	2.200E+05	clean
36	24-32	5.09E+06	1.67E+07	2.97E+06	6.0	1446	63.5	7.956E-02	956.0	2.200E+05	clean
37	24-32	5.89E+06	1.93E+07	3.44E+06	6.0	1677	63.4	9.220E-02	955.9	2.200E+05	clean
38	24-32	7.37E+06	2.42E+07	4.30E+06	6.0	2132	64.2	1.160E-01	960.4	2.249E+05	clean
Runs with trips											
60	23-32	7.37E+06	2.42E+07	4.30E+06	6.0	2132	64.2	1.160E-01	960.4	2.249E+05	0.0115 inch
53	24-32	3.02E+06	9.91E+06	1.76E+06	6.0	841	62.6	4.680E-02	950.6	2.140E+05	0.0045 inch
52	24-32	3.91E+06	1.28E+07	2.28E+06	6.0	1109	63.4	6.103E-02	956.2	2.200E+05	0.0045 inch
51	24-32	5.09E+06	1.67E+07	2.97E+06	6.0	1446	63.5	7.956E-02	956.0	2.200E+05	0.0045 inch
62	15-24	5.89E+06	1.93E+07	3.44E+06	6.0	1677	63.4	9.220E-02	955.9	2.200E+05	0.0045 inch
50	24-32	5.89E+06	1.93E+07	3.44E+06	6.0	1677	63.4	9.220E-02	955.9	2.200E+05	0.0045 inch
61	15-24	7.37E+06	2.42E+07	4.30E+06	6.0	2132	64.2	1.160E-01	960.4	2.249E+05	0.0045 inch
49	23-32	7.37E+06	2.42E+07	4.30E+06	6.0	2132	64.2	1.160E-01	960.4	2.249E+05	0.0045 inch

Run	α (deg)	Re_∞ (1/ft)	Re_∞ (1/m)	$Re_{\infty,D}$	Mach	P_∞ (Pa)	T_∞ (K)	ρ_∞ (kg/m^3)	U_∞ (m/s)	H_0-H_{300K} (J/kg)	Trips
59	24-32	2.01E+06	6.61E+06	1.17E+06	6.0	552	61.9	3.103E-02	946.0	2.090E+05	0.0065 inch
58	24-32	3.02E+06	9.91E+06	1.76E+06	6.0	841	62.6	4.680E-02	950.6	2.140E+05	0.0065 inch
57	24-32	3.91E+06	1.28E+07	2.28E+06	6.0	1109	63.4	6.103E-02	956.2	2.200E+05	0.0065 inch
56	24-32	5.09E+06	1.67E+07	2.97E+06	6.0	1446	63.5	7.956E-02	956.0	2.200E+05	0.0065 inch
55	24-32	5.89E+06	1.93E+07	3.44E+06	6.0	1677	63.4	9.220E-02	955.9	2.200E+05	0.0065 inch
54	24-32	7.37E+06	2.42E+07	4.30E+06	6.0	2132	64.2	1.160E-01	960.4	2.249E+05	0.0065 inch
48	23-32	3.02E+06	9.91E+06	1.76E+06	6.0	841	62.6	4.680E-02	950.6	2.140E+05	0.0115 inch
66	15-24	3.91E+06	1.28E+07	2.28E+06	6.0	1109	63.4	6.103E-02	956.2	2.200E+05	0.0115 inch
47	23-32	3.91E+06	1.28E+07	2.28E+06	6.0	1109	63.4	6.103E-02	956.2	2.200E+05	0.0115 inch
65	15-24	5.09E+06	1.67E+07	2.97E+06	6.0	1446	63.5	7.956E-02	956.0	2.200E+05	0.0115 inch
46	23-32	5.09E+06	1.67E+07	2.97E+06	6.0	1446	63.5	7.956E-02	956.0	2.200E+05	0.0115 inch
64	15-24	5.89E+06	1.93E+07	3.44E+06	6.0	1677	63.4	9.220E-02	955.9	2.200E+05	0.0115 inch
45	23-32	5.89E+06	1.93E+07	3.44E+06	6.0	1677	63.4	9.220E-02	955.9	2.200E+05	0.0115 inch
67	28	7.37E+06	2.42E+07	4.30E+06	6.0	2132	64.2	1.160E-01	960.4	2.249E+05	0.0115 inch
63	15-24	7.37E+06	2.42E+07	4.30E+06	6.0	2132	64.2	1.160E-01	960.4	2.249E+05	0.0115 inch
44	23-32	7.37E+06	2.42E+07	4.30E+06	6.0	2132	64.2	1.160E-01	960.4	2.249E+05	0.0115 inch
68	32-23	7.37E+06	2.42E+07	4.30E+06	6.0	2132	64.2	1.160E-01	960.4	2.249E+05	0.0115 inch

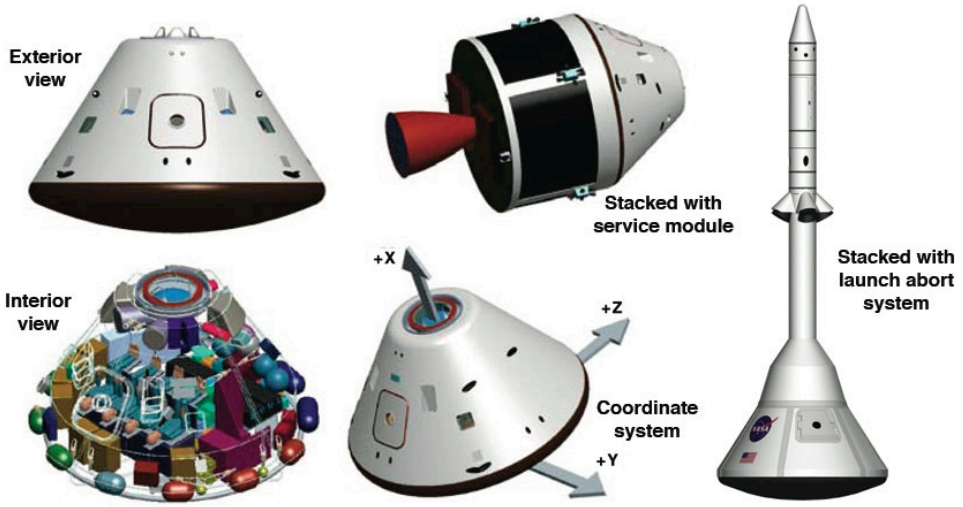

Figure 1. NASA CEV (conceptual artwork)

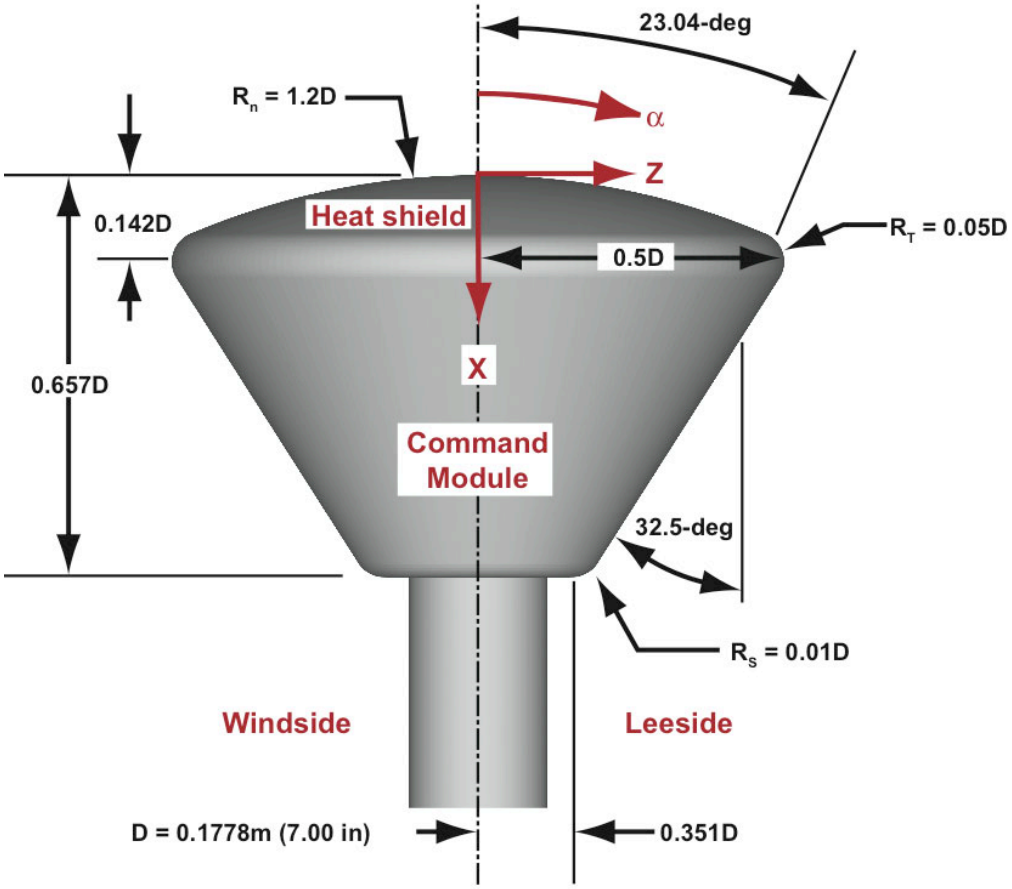

Figure 2. Wind tunnel model dimensions

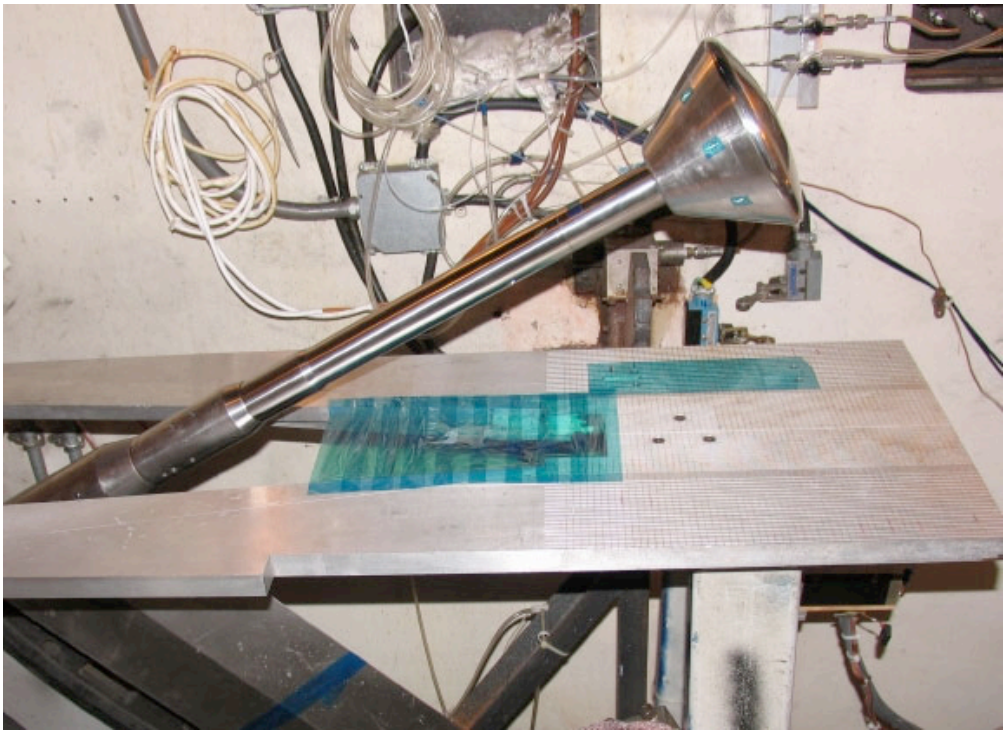

Figure 3. CEV model installed in LaRC 20-Inch Mach 6 Air Tunnel (injection system retracted into model box)

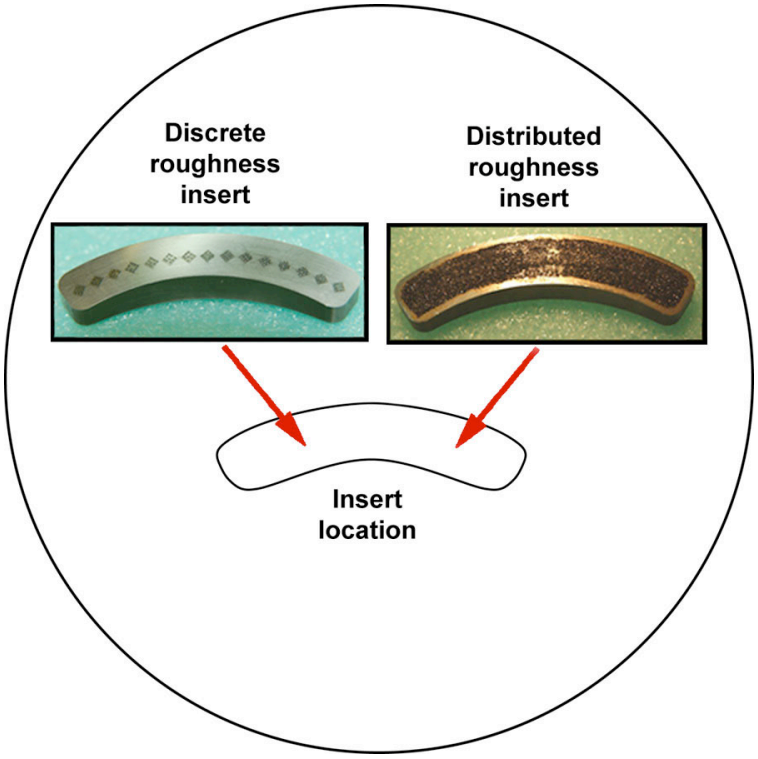

Figure 4. CEV model inserts (not employed in this study)

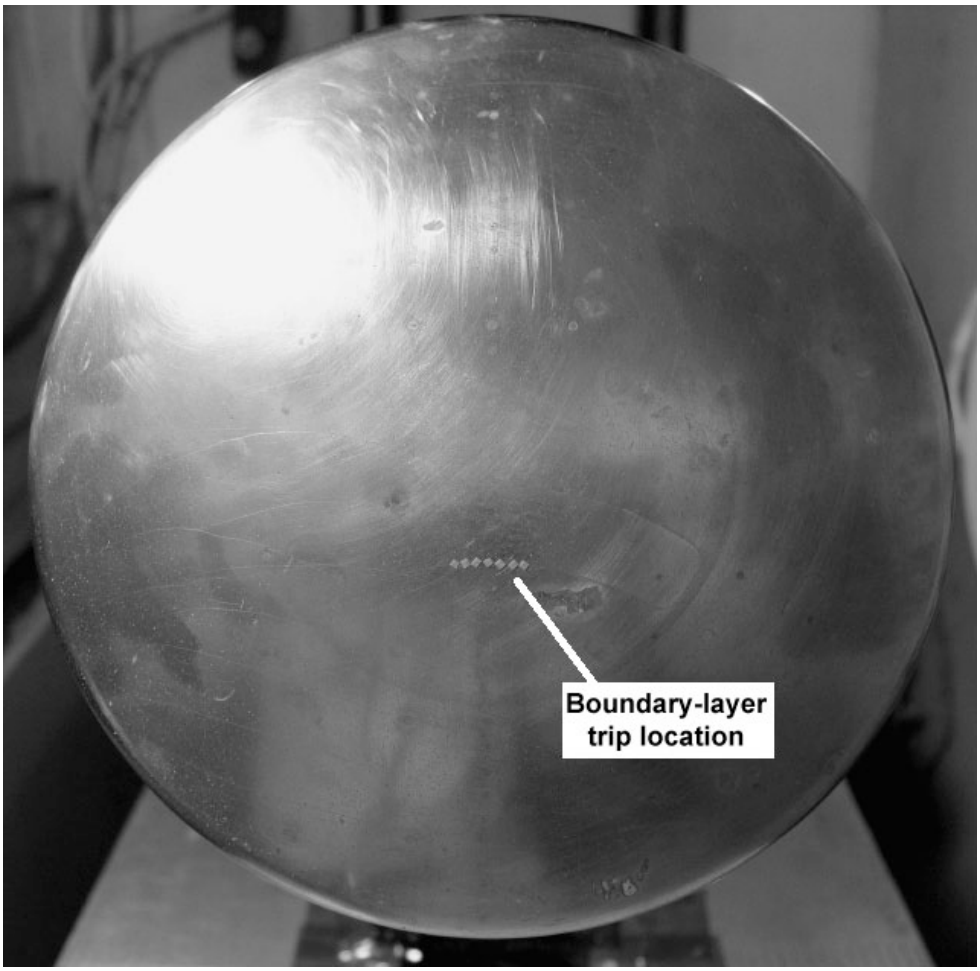

Figure 5. Trip Location on CEV Model

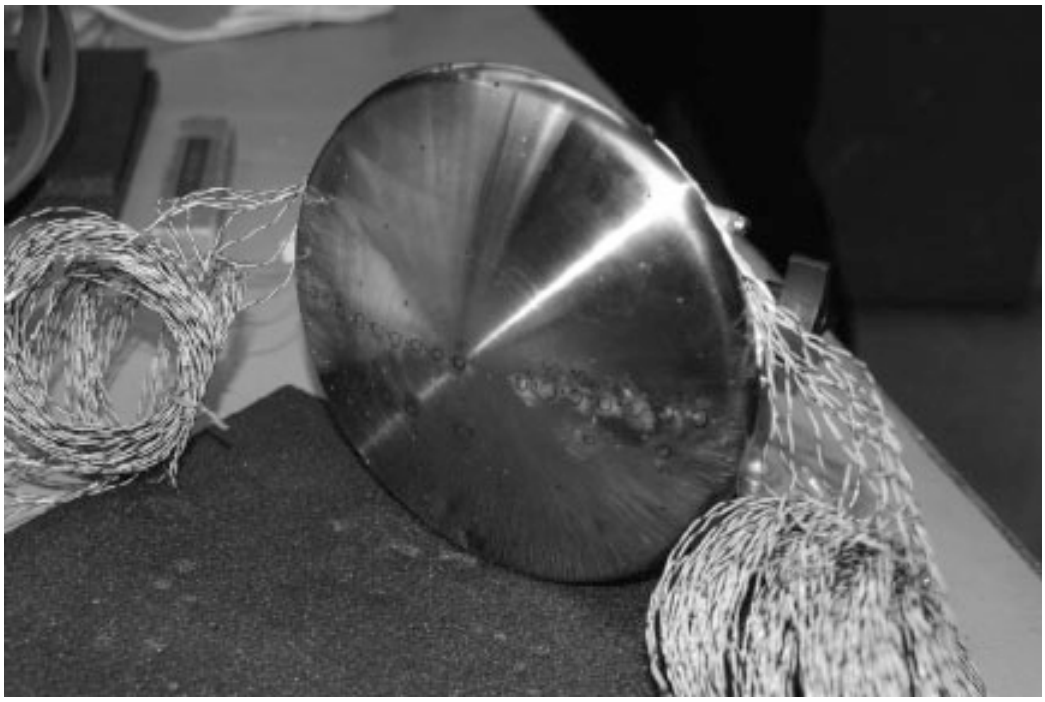

Figure 6. CEV model heat shield during thermocouple installation process

Figure 7. Disassembled CEV model heat shield and aftbody

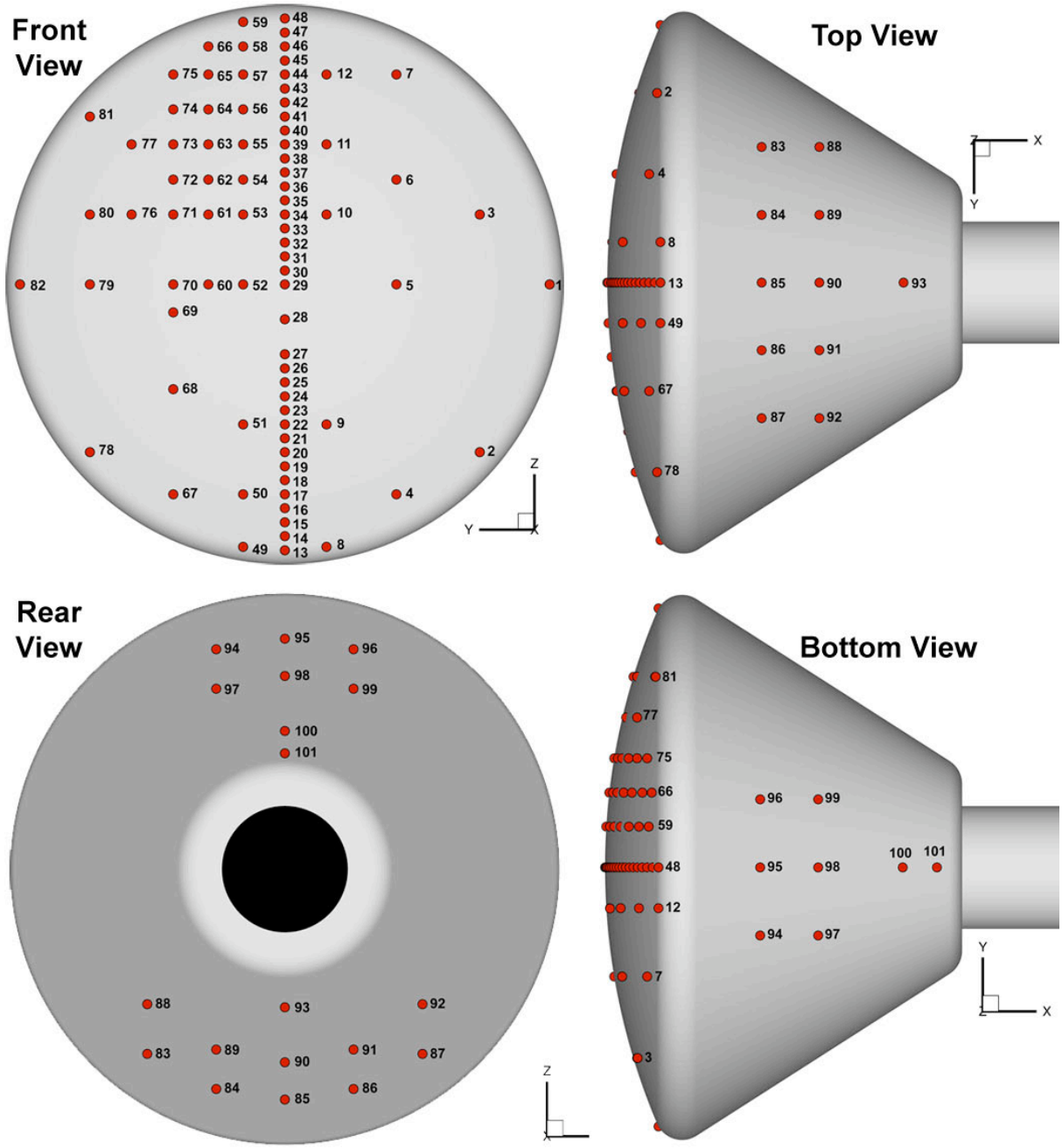

Figure 8. Thermocouple layout on CEV model

Figure 9. LaRC 20-Inch Mach 6 Air Tunnel (with CEV model installed)

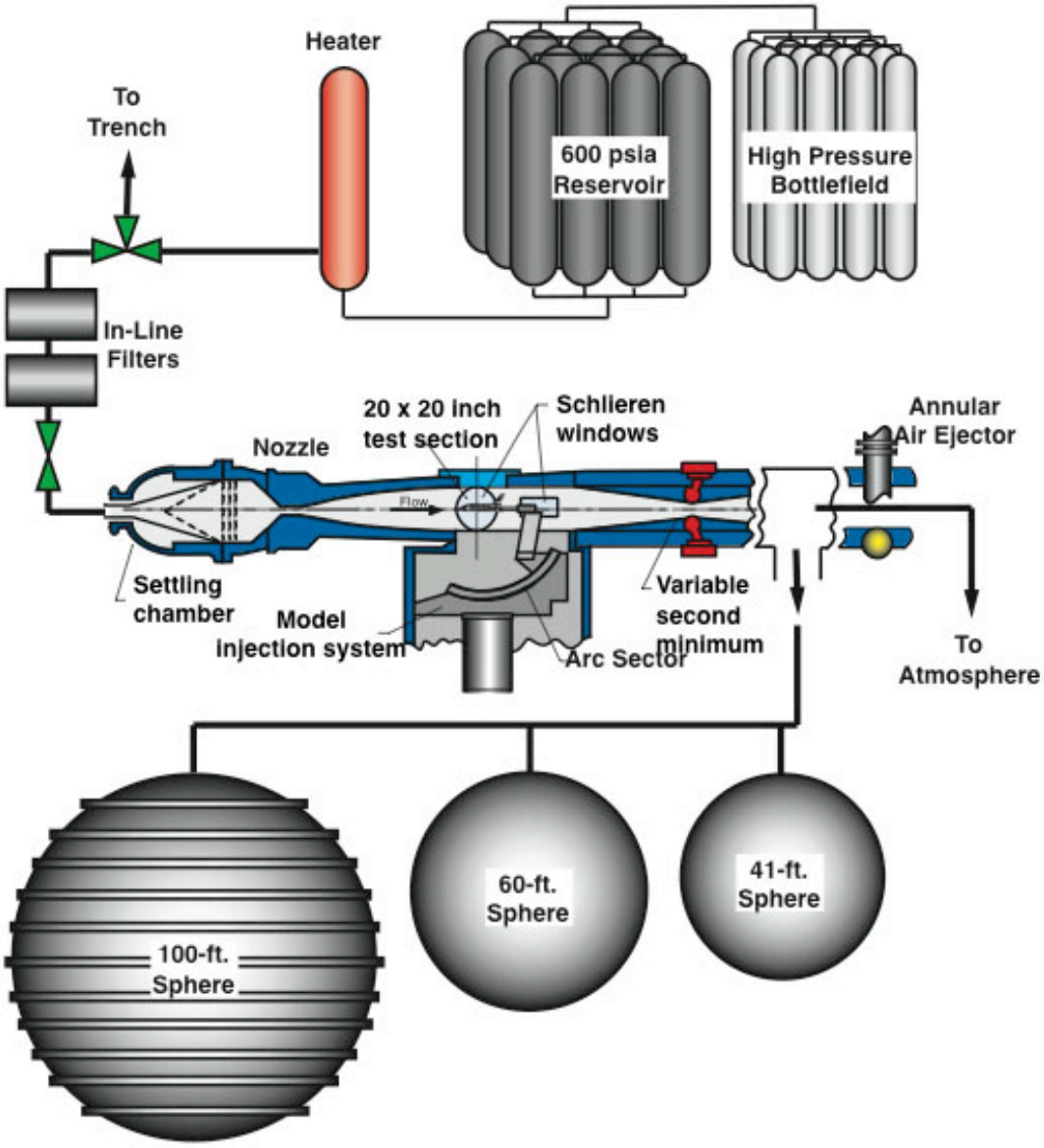

Figure 10. Schematic of LaRC 20-Inch Mach 6 Air Tunnel

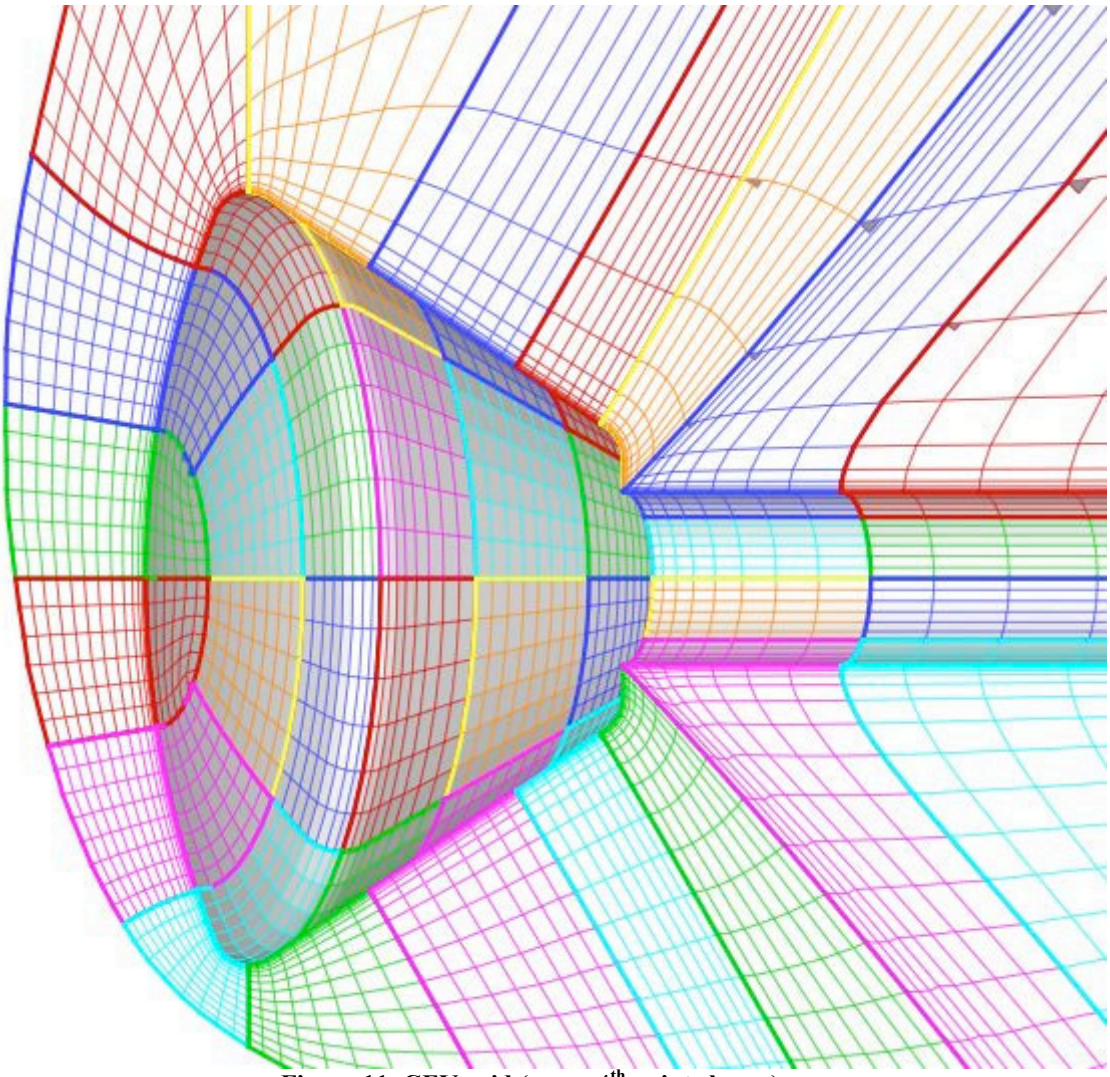

Figure 11. CEV grid (every 4th point shown)

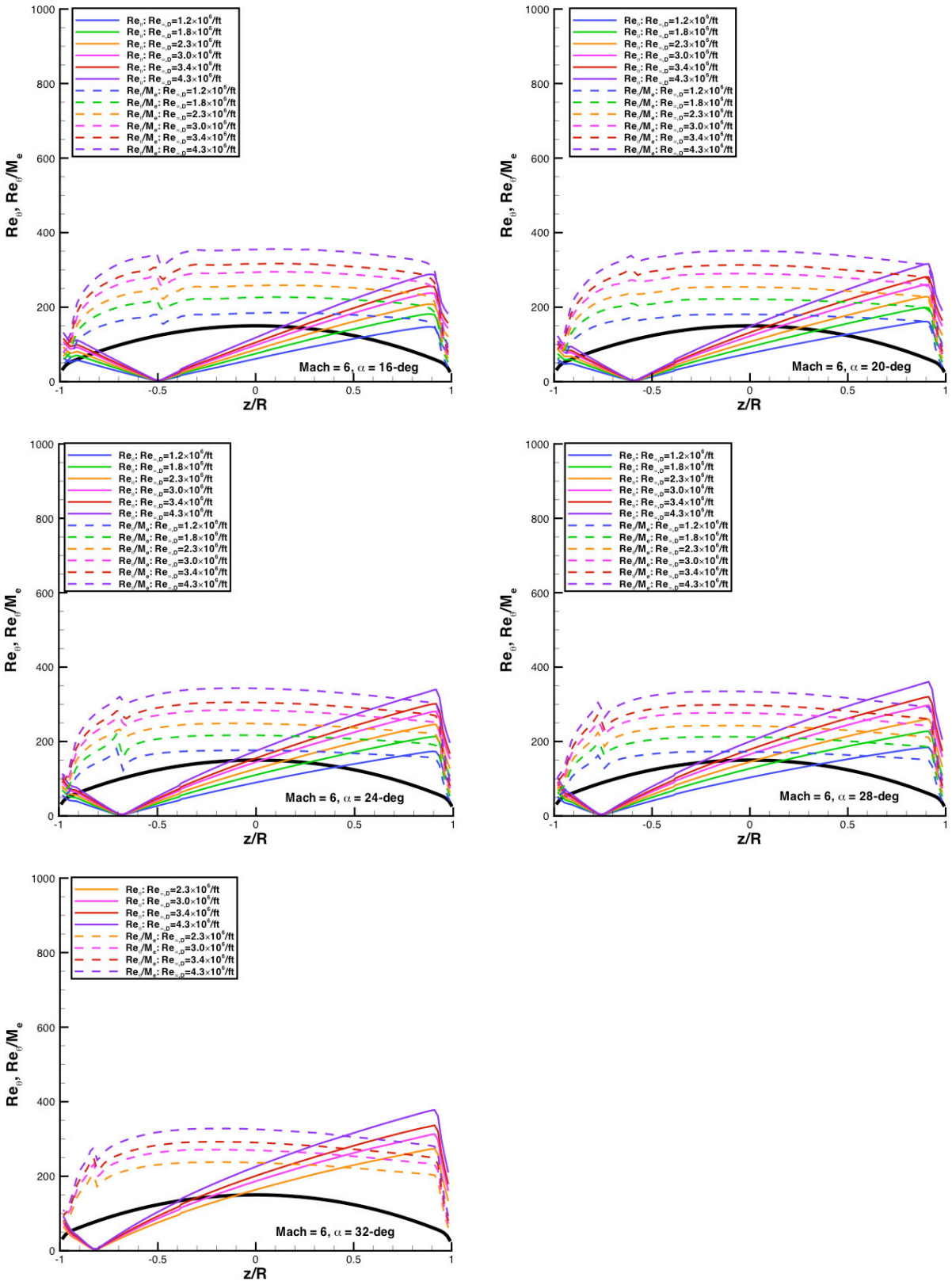

Figure 12. Predicted boundary-layer transition parameters, α = 16-deg to 32-deg

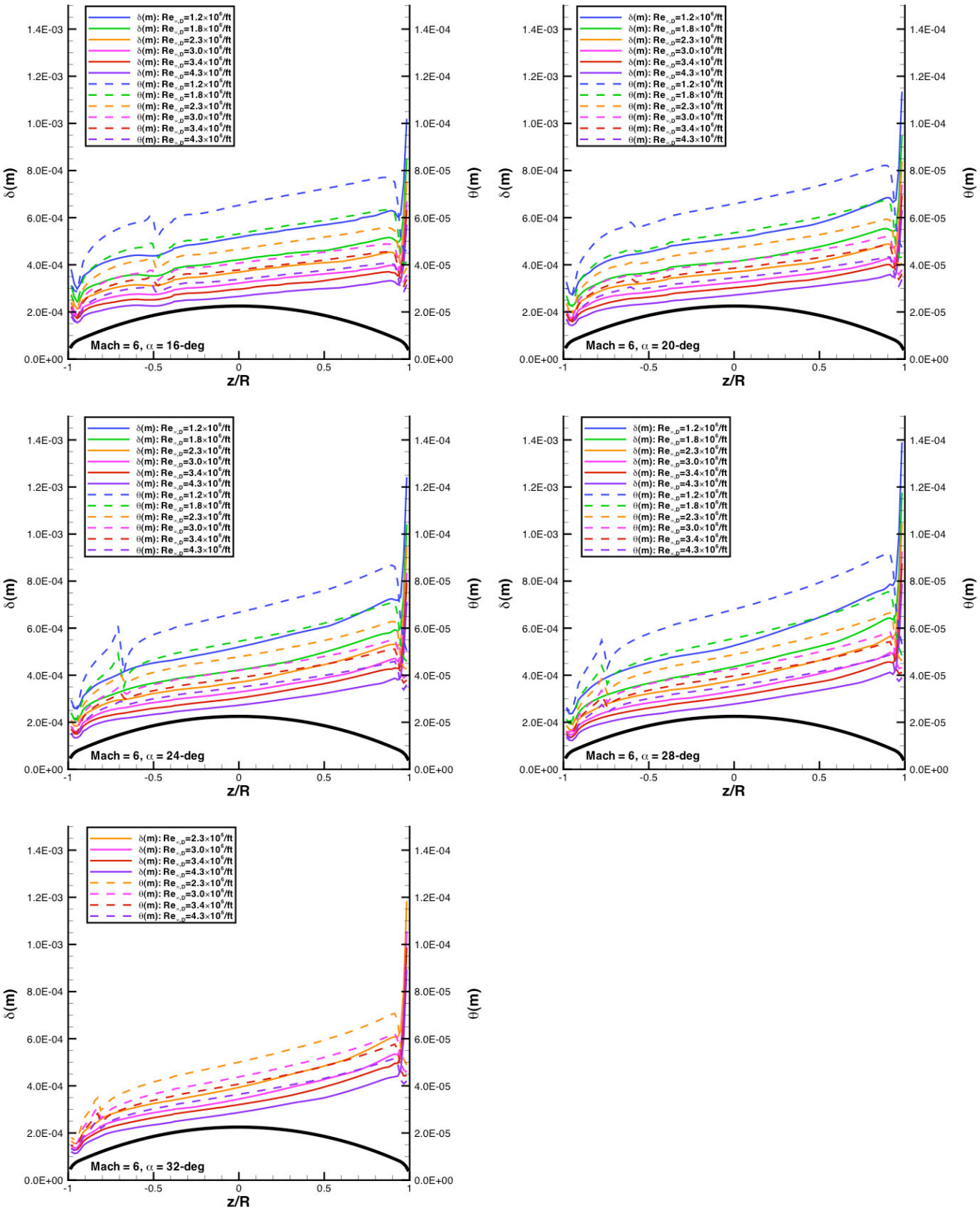

Figure 13. Predicted boundary-layer height parameters, α = 16-deg to 32-deg

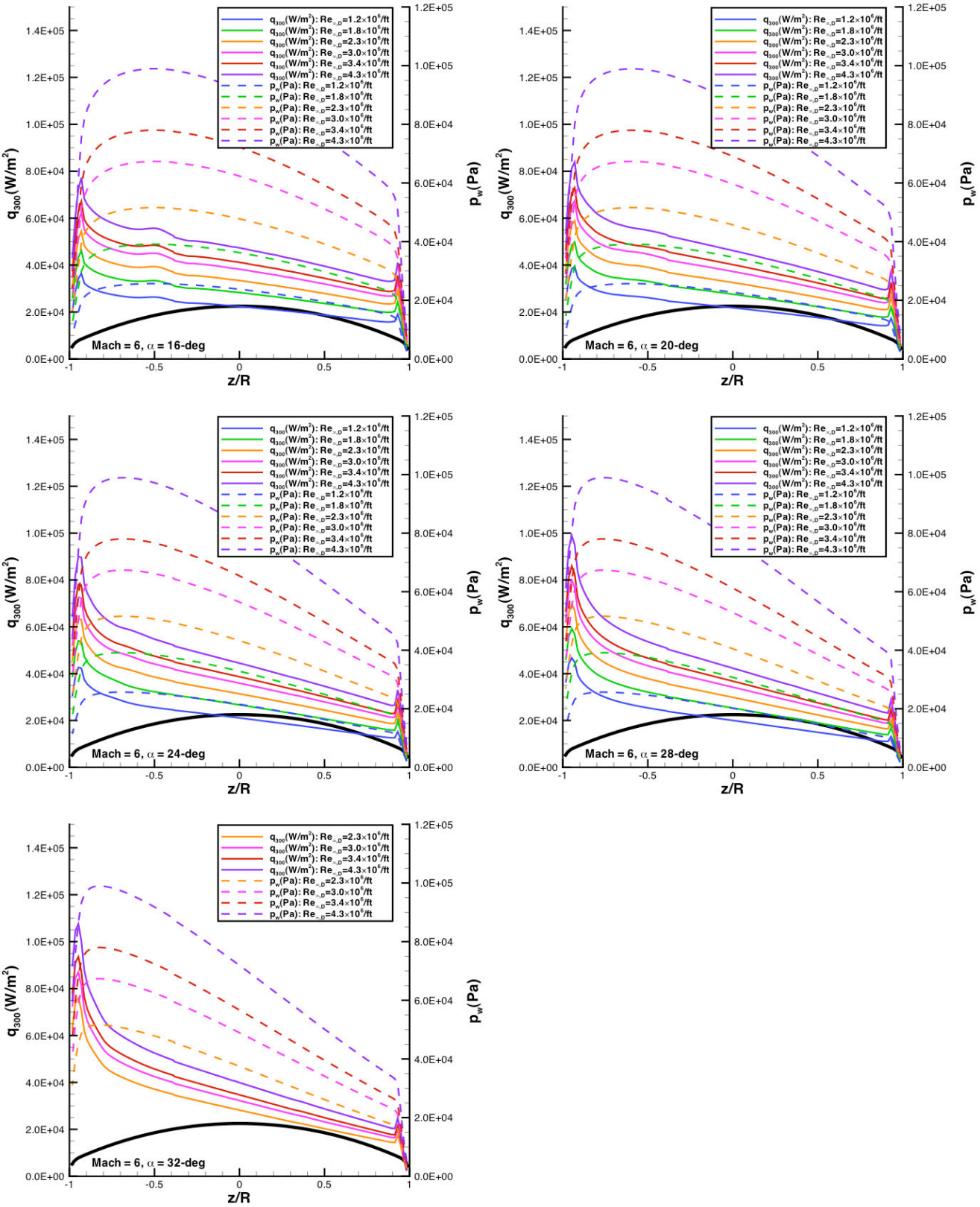

Figure 14. Predicted surface heating and pressure, α = 16-deg to 32-deg

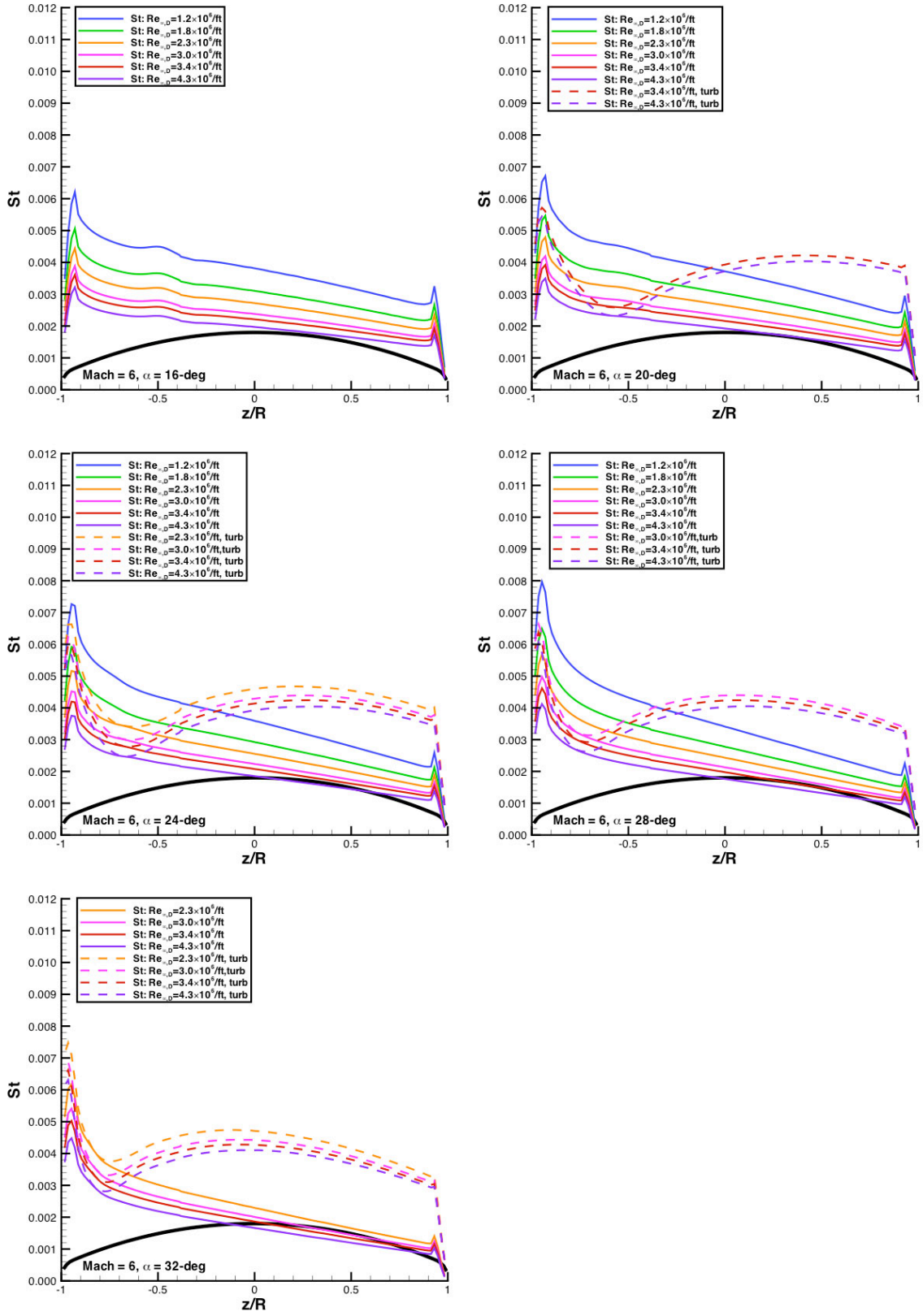

Figure 15. Predicted Stanton numbers, α = 16-deg to 32-deg

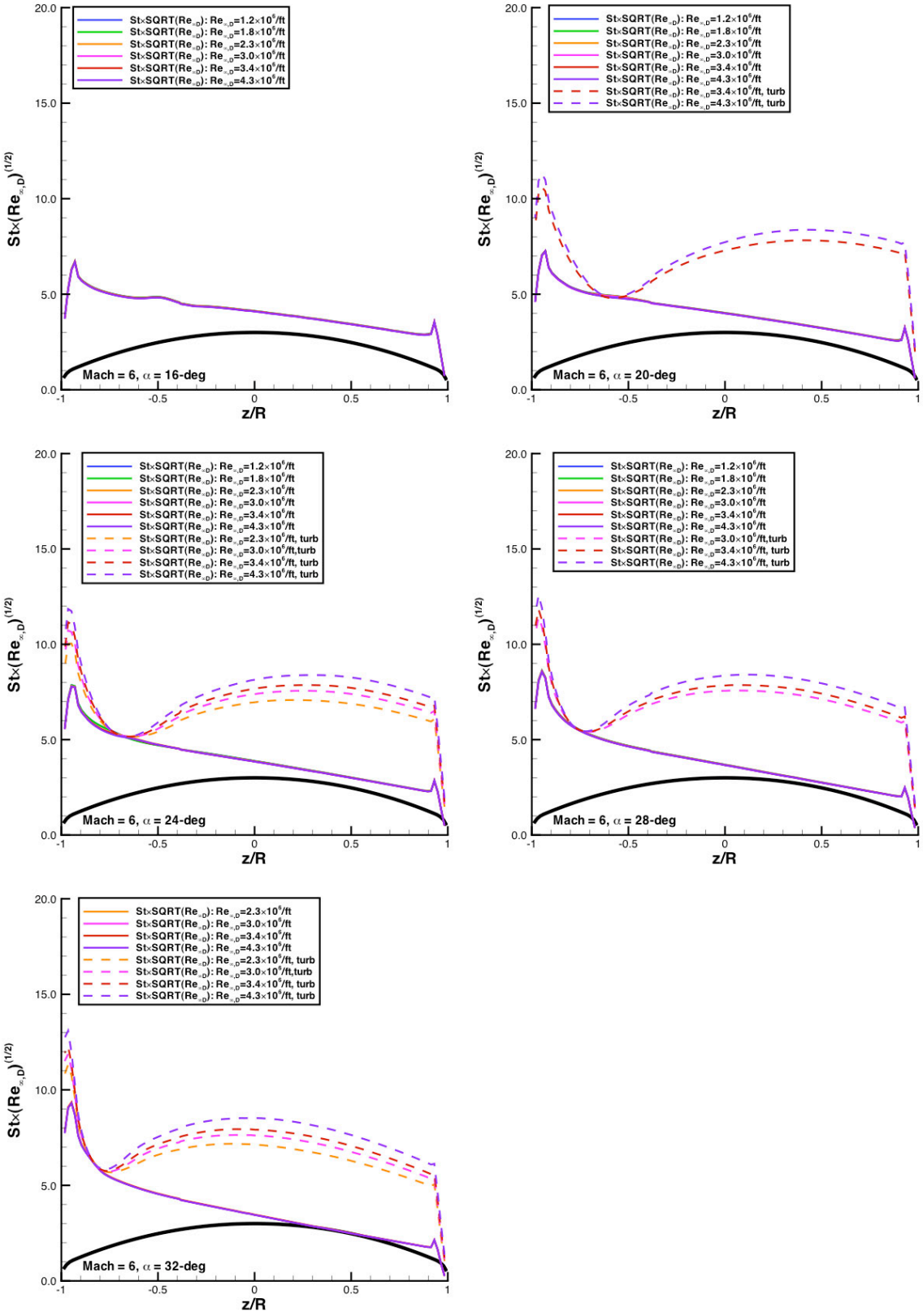

Figure 16. Laminar correlation parameter for predicted heating, α = 16-deg to 32-deg

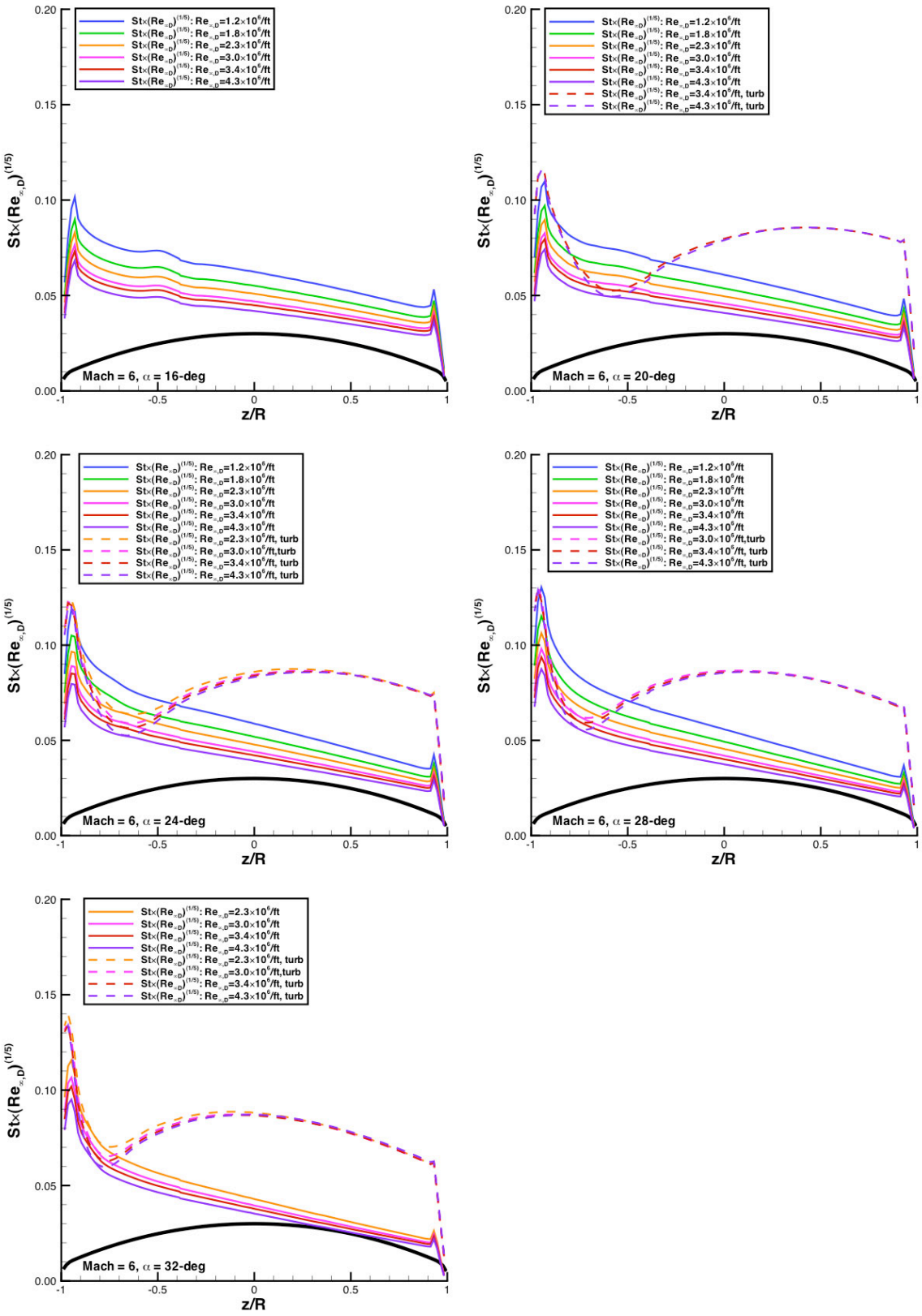

Figure 17. Turbulent correlation parameter for predicted heating, α = 16-deg to 32-deg

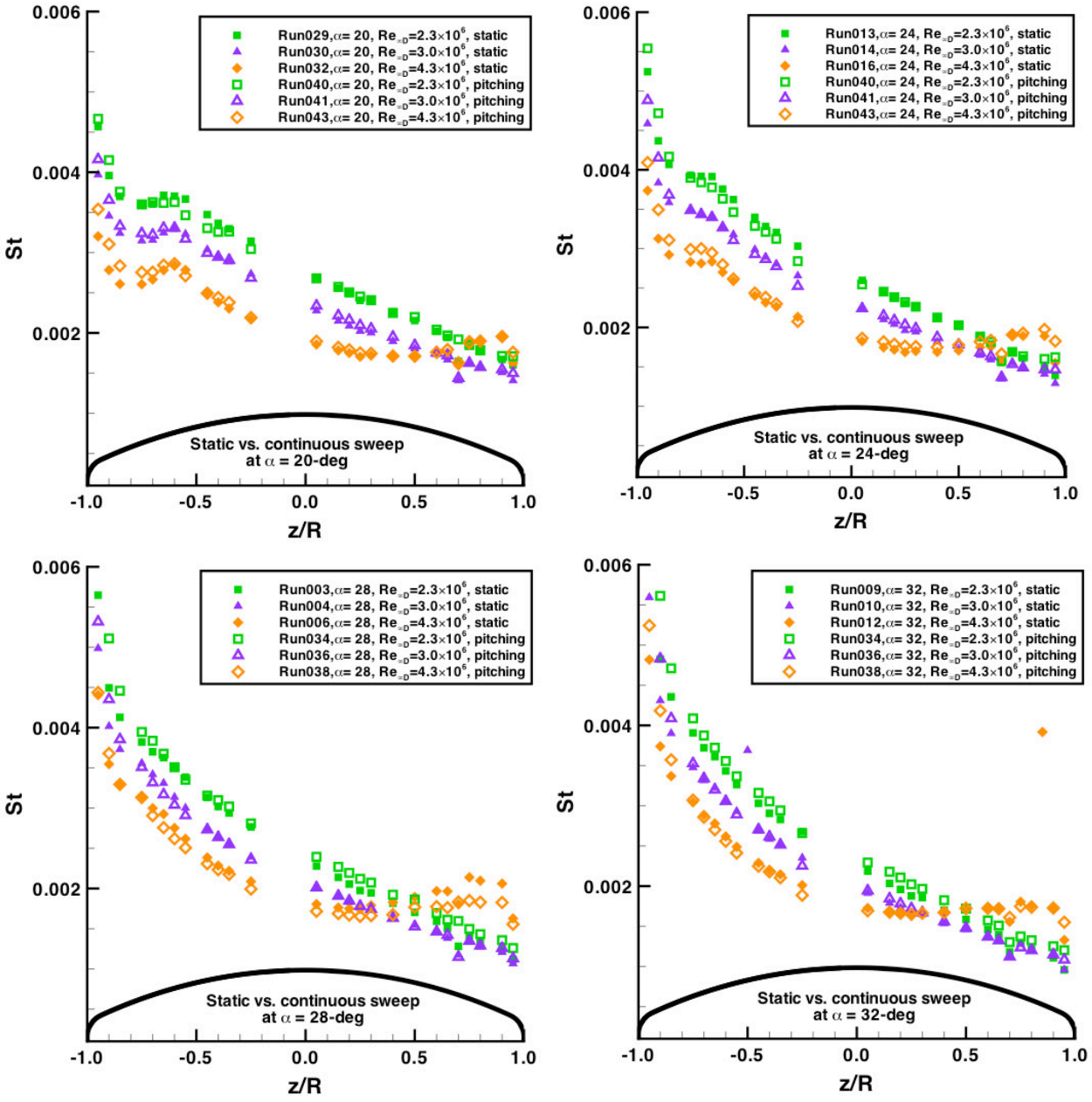

Figure 18. Comparison of static and continuous sweep runs, α = 20-deg to 32-deg

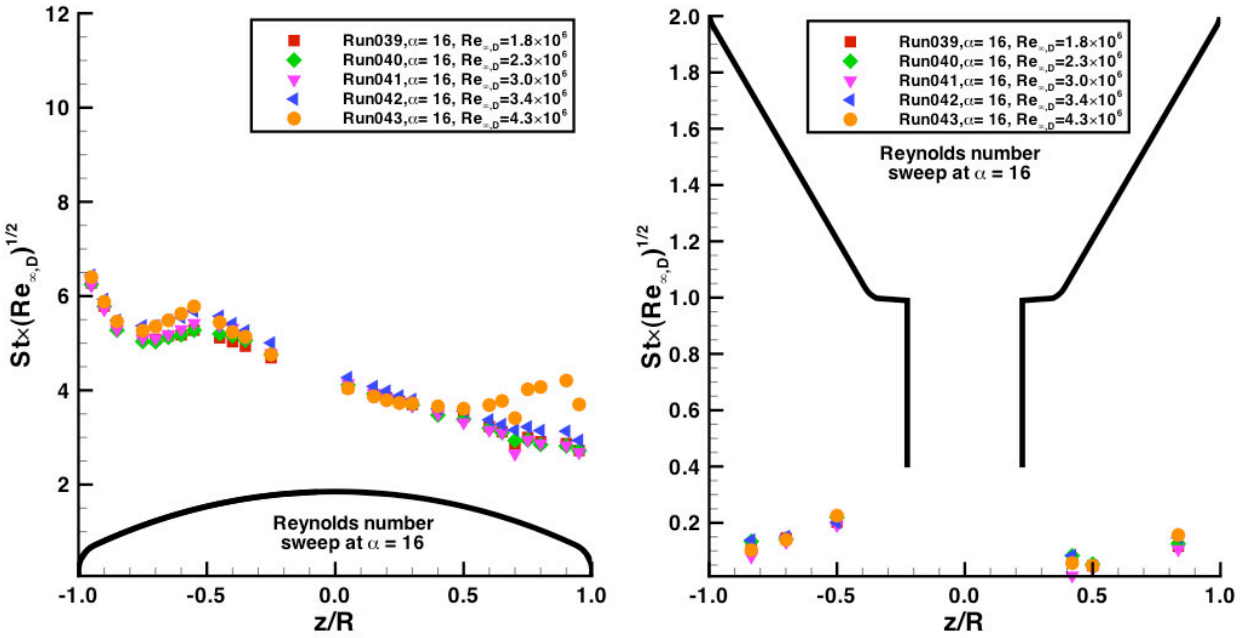

Figure 19. Reynolds numbers effects, pitching runs, α = 16-deg

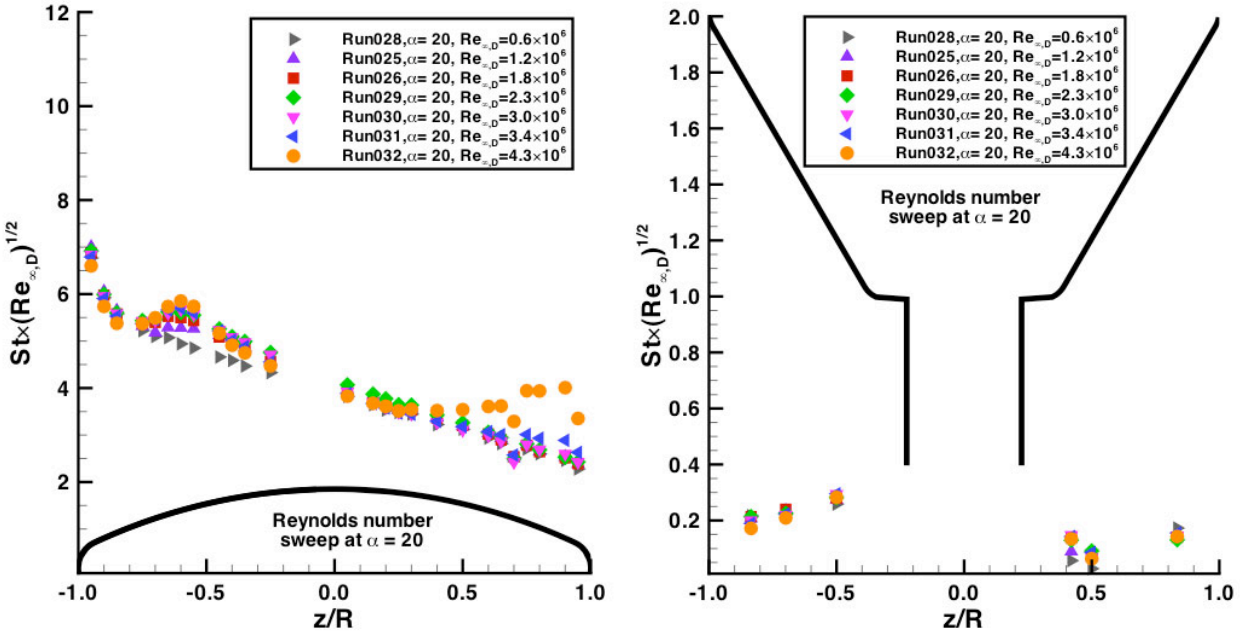

Figure 20. Reynolds numbers effects, static runs, α = 20-deg

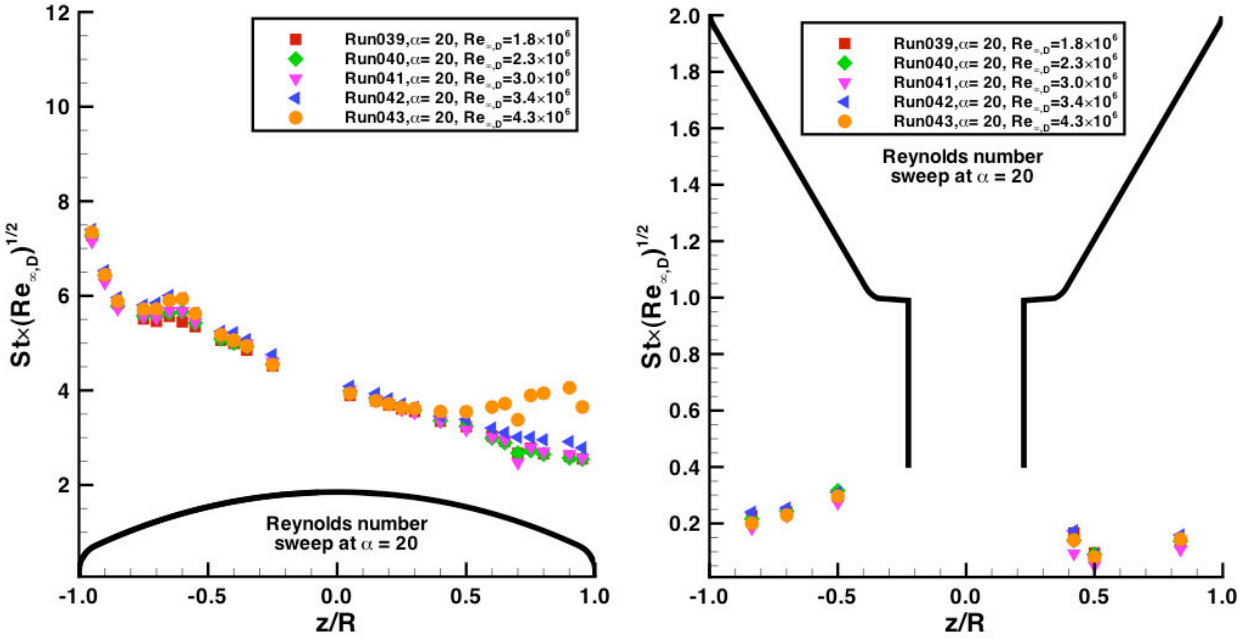

Figure 21. Reynolds numbers effects, pitching runs, α = 20-deg

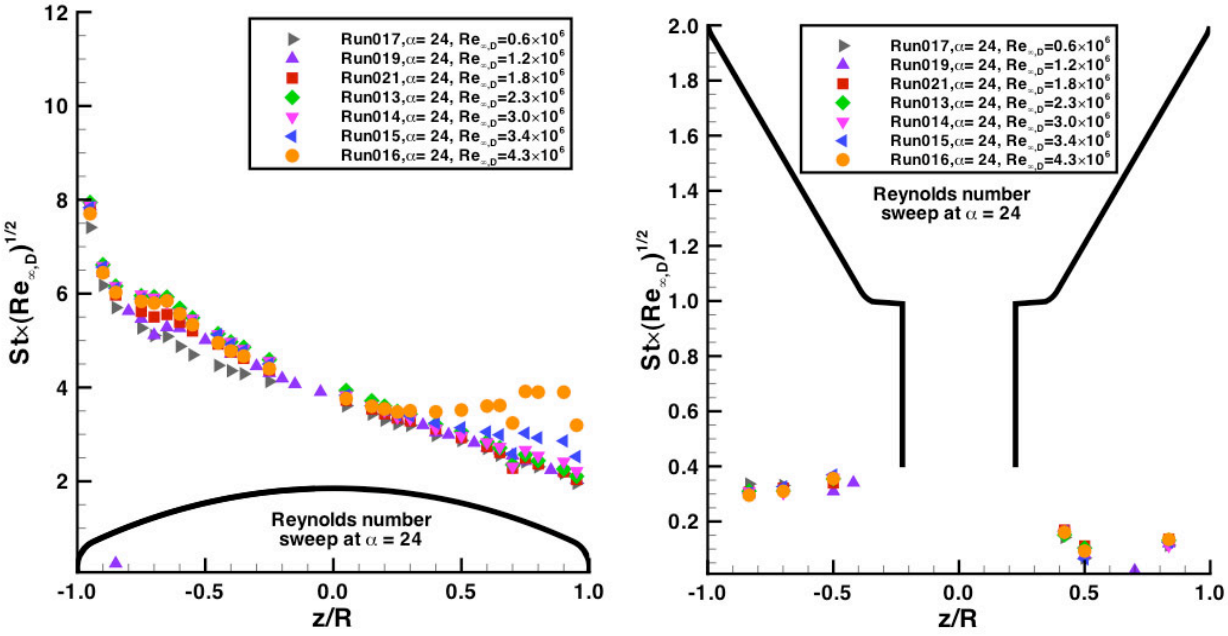

Figure 22. Reynolds numbers effects, static runs, α = 24-deg

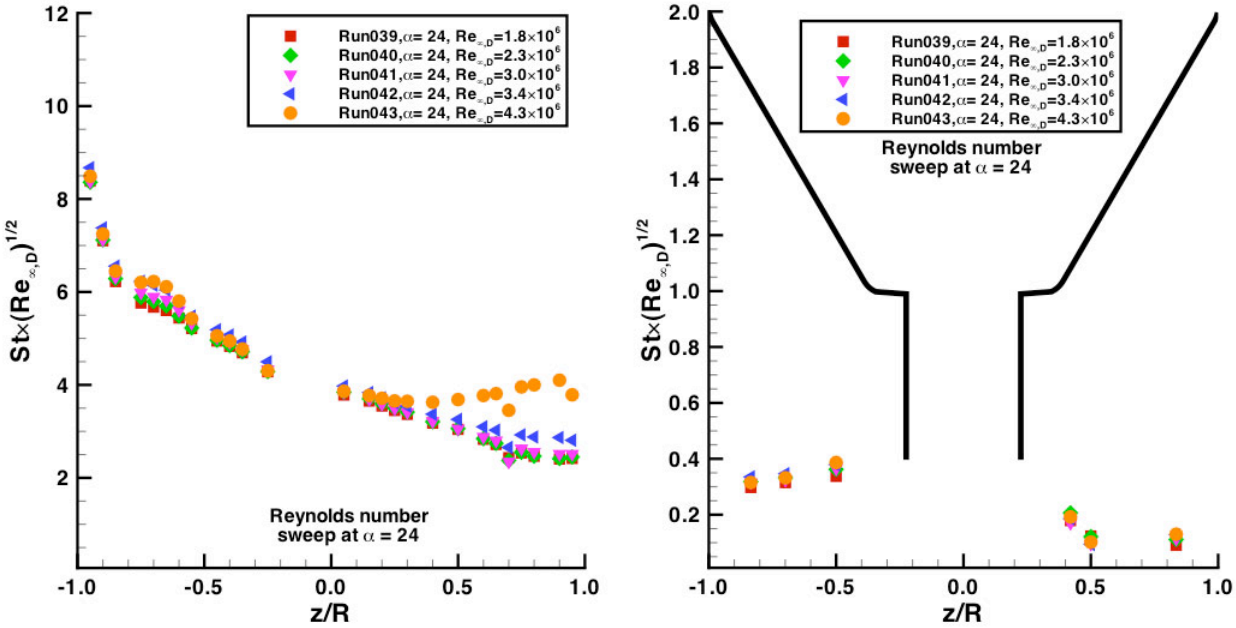

Figure 23. Reynolds numbers effects, pitching runs, α = 24-deg

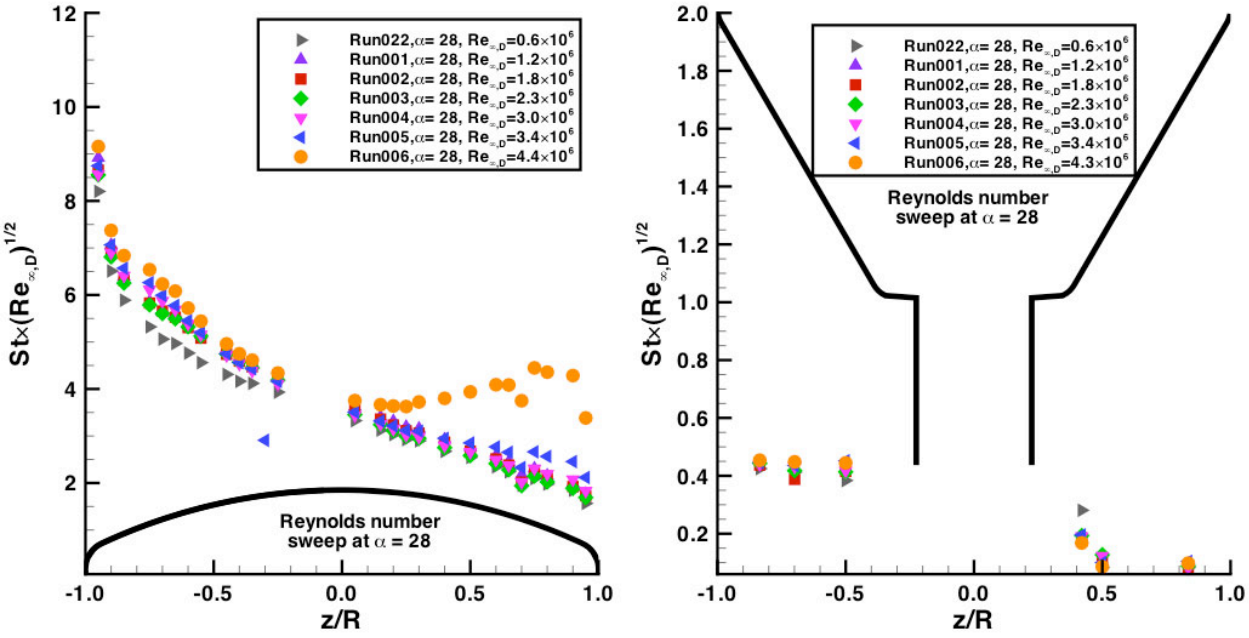

Figure 24. Reynolds numbers effects, static runs, α = 28-deg

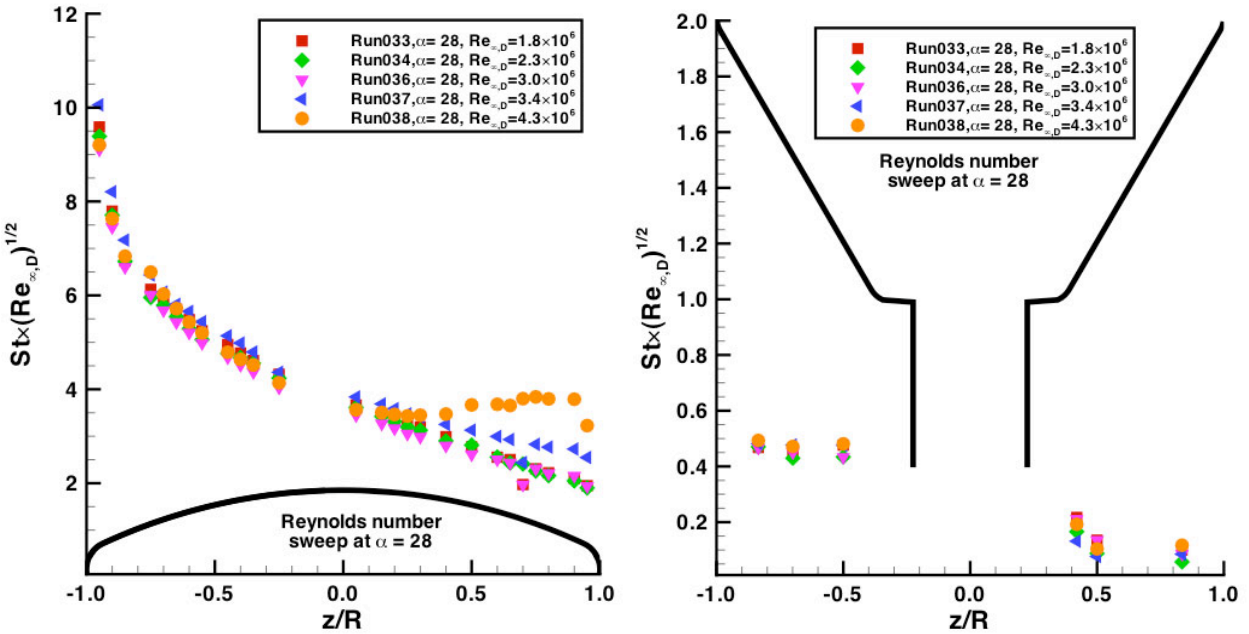

Figure 25. Reynolds numbers effects, pitching runs, α = 28-deg

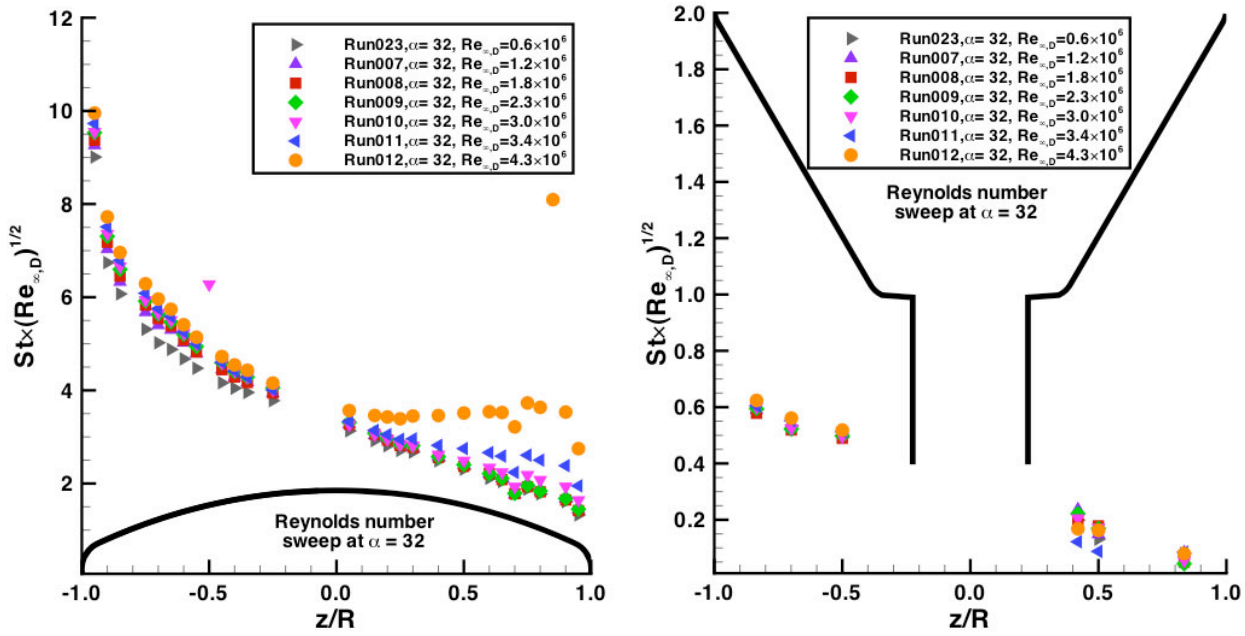

Figure 26. Reynolds numbers effects, static runs, α = 32-deg

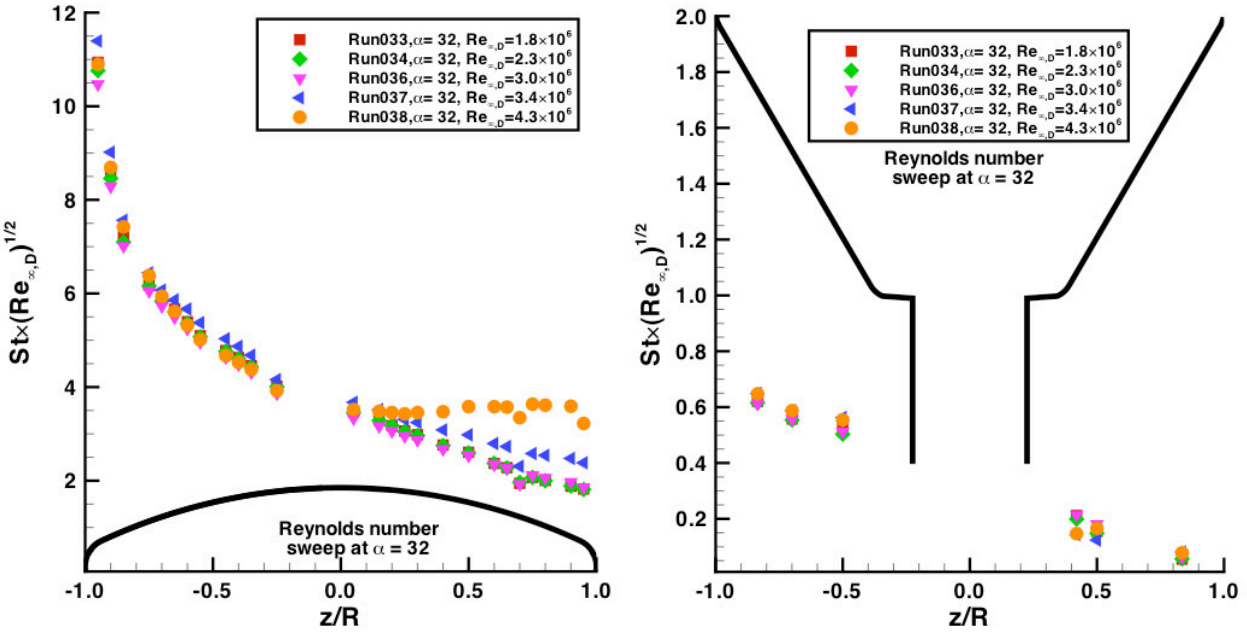

Figure 27. Reynolds numbers effects, pitching runs, α = 32-deg

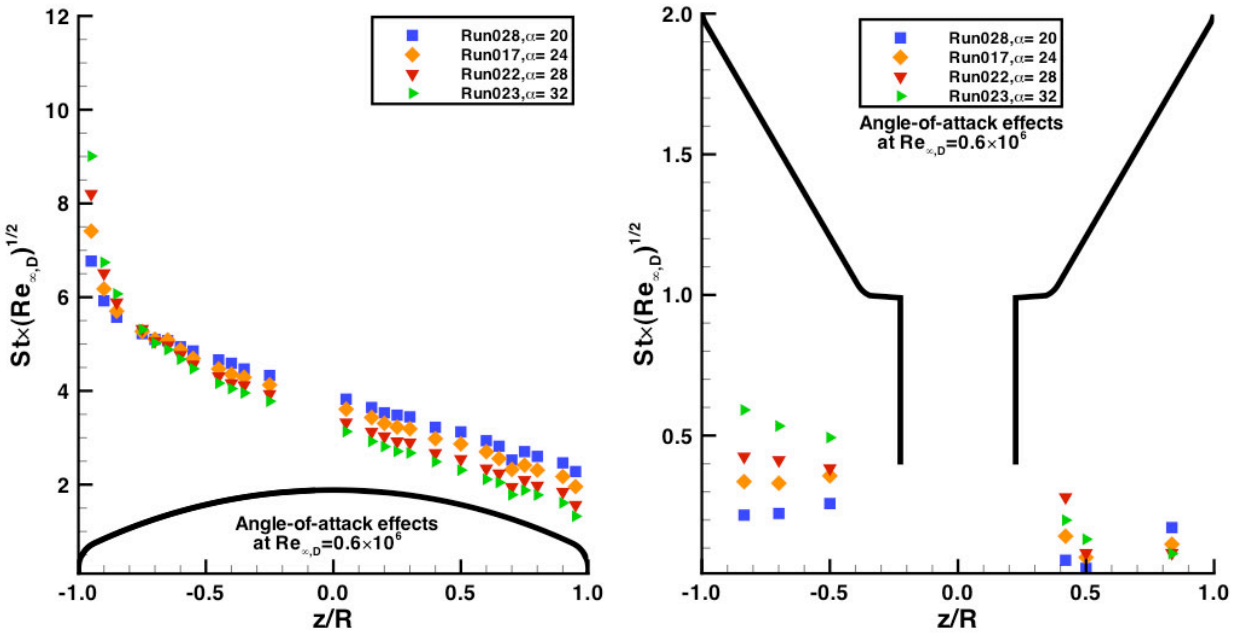

Figure 28. Angle-of-attack effects, $Re_{\infty,D} = 0.6\times10^6$

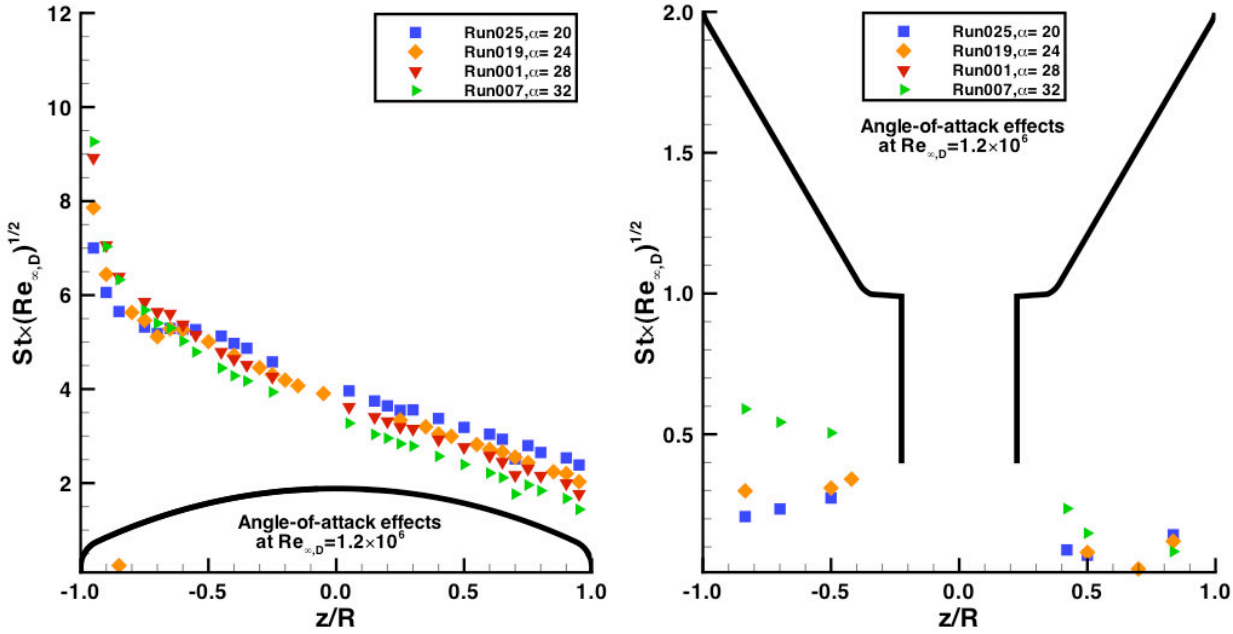

Figure 29. Angle-of-attack effects, $Re_{\infty,D} = 1.2\times10^6$

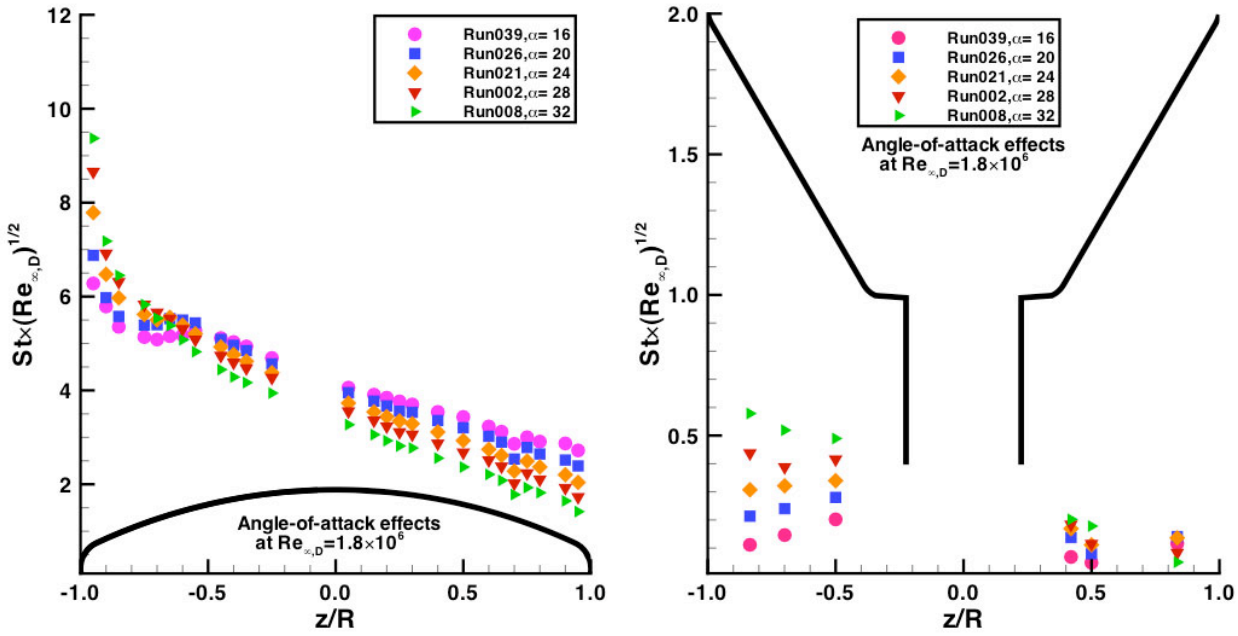

Figure 30. Angle-of-attack effects, $Re_{\infty,D} = 1.8\times10^6$

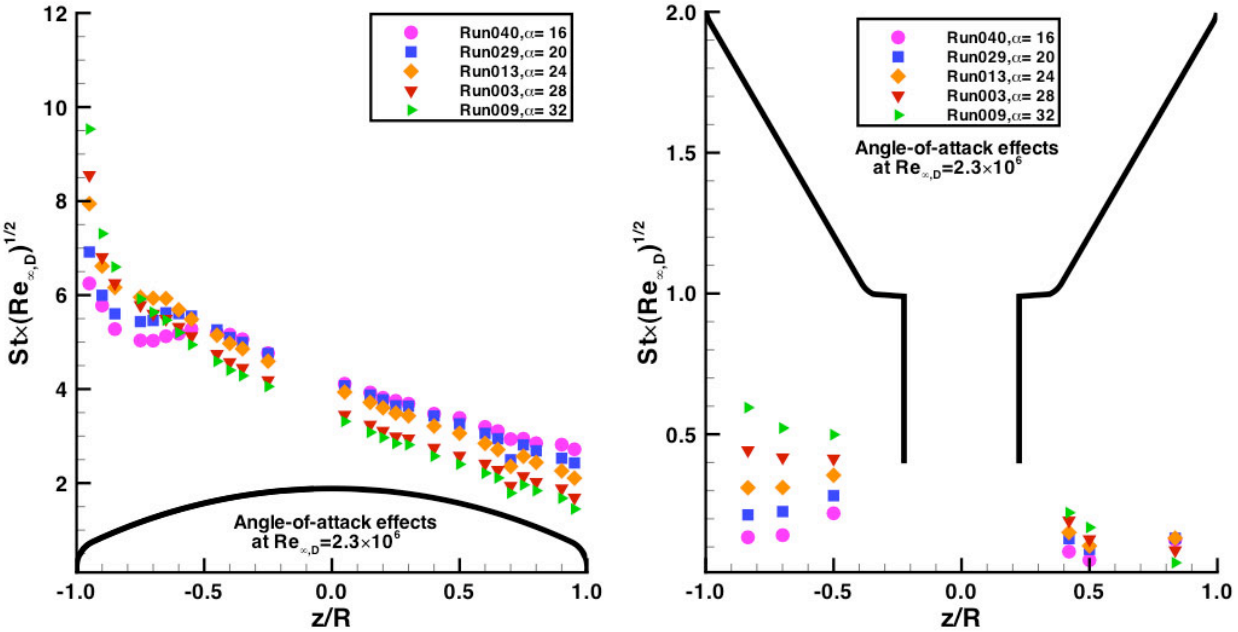

Figure 31. Angle-of-attack effects, $Re_{\infty,D} = 2.3\times10^6$

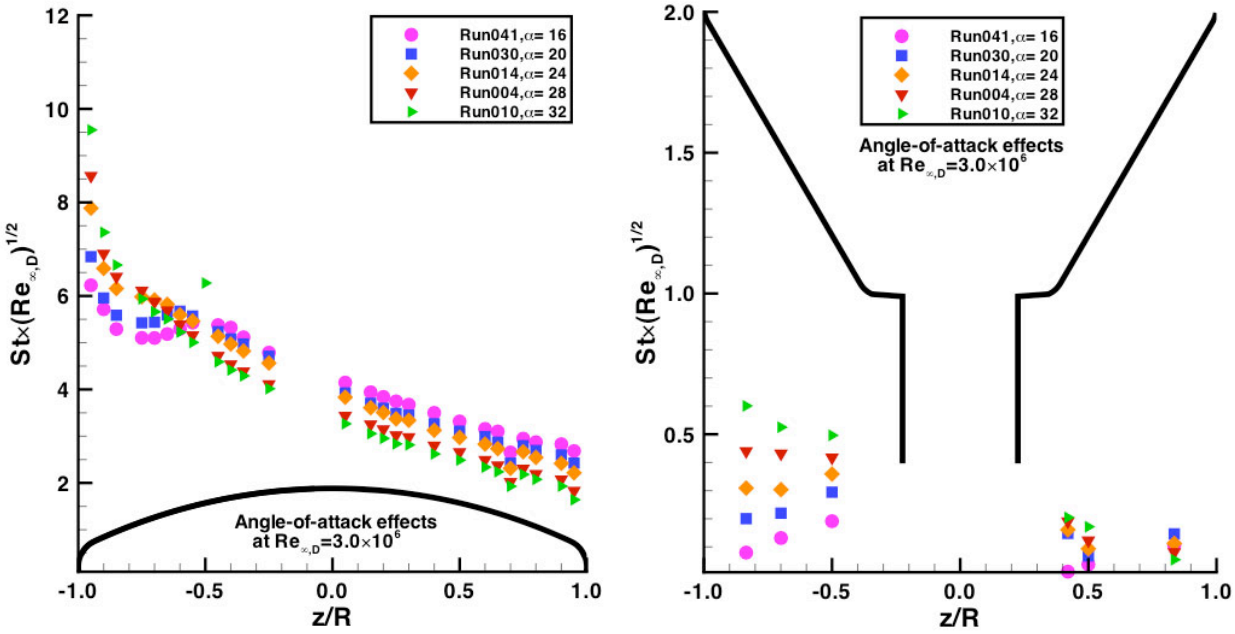

Figure 32. Angle-of-attack effects, $Re_{\infty,D} = 3.0\times10^6$

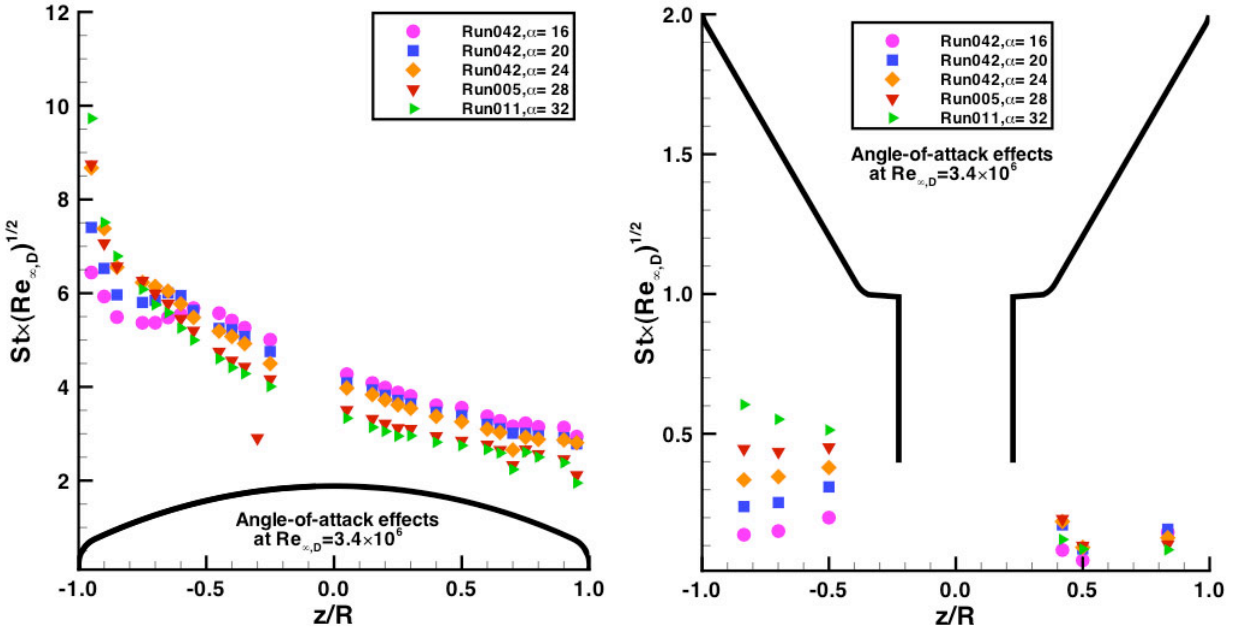

Figure 33. Angle-of-attack effects, $Re_{\infty,D} = 3.4\times10^6$

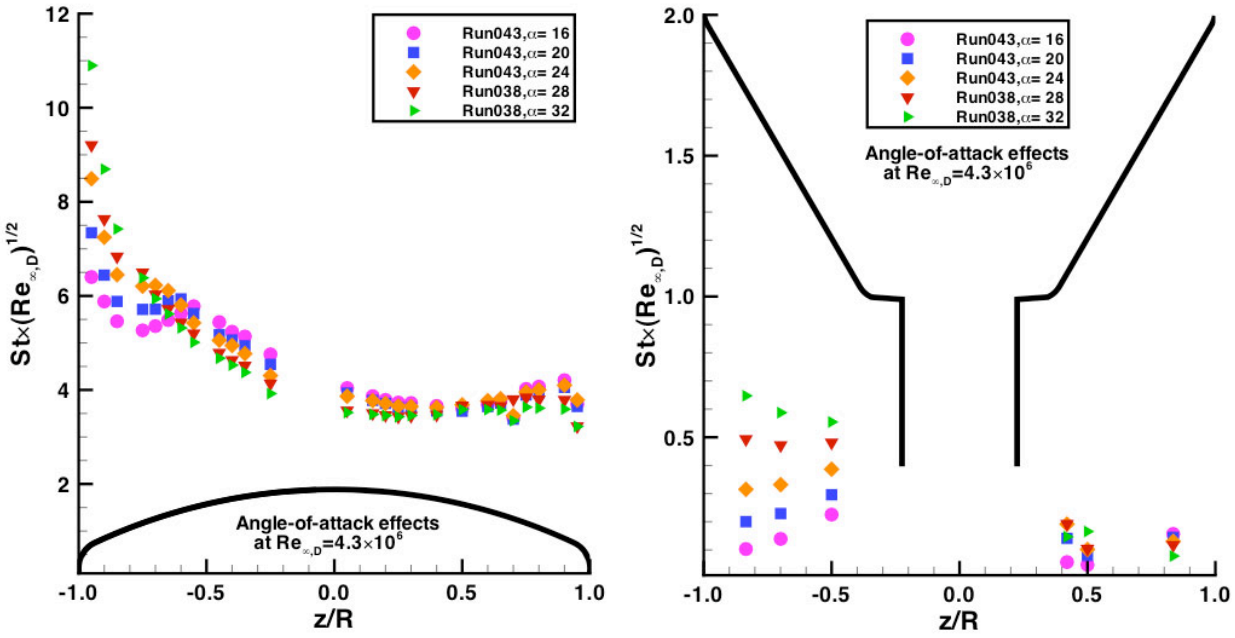

Figure 34. Angle-of-attack effects, $Re_{\infty,D} = 4.3\times10^6$

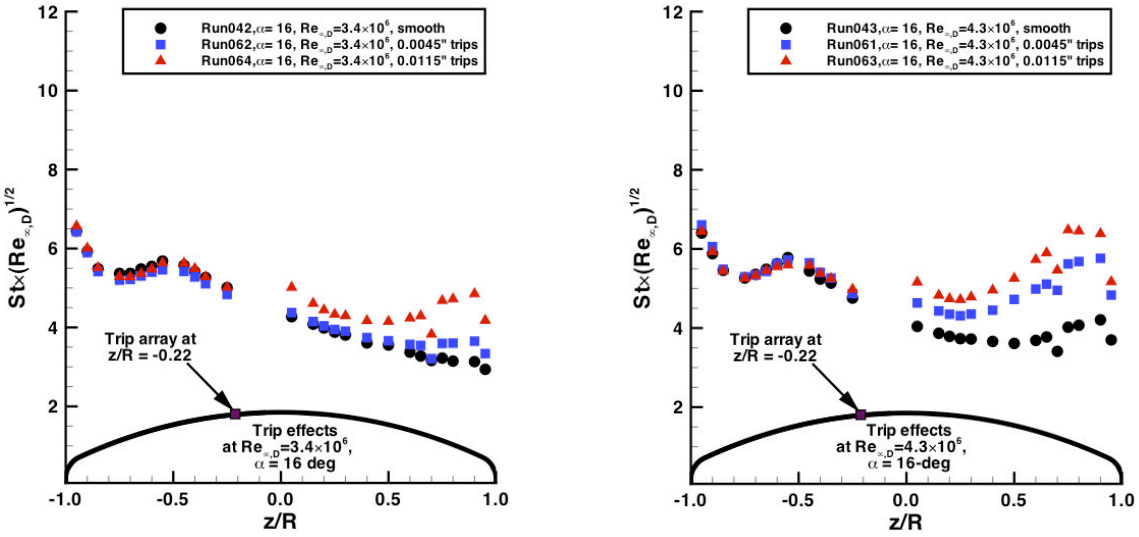

Figure 35. Trip effects at α = 16-deg, $Re_{\infty,D} = 3.4\times10^6$ to 4.3×10^6

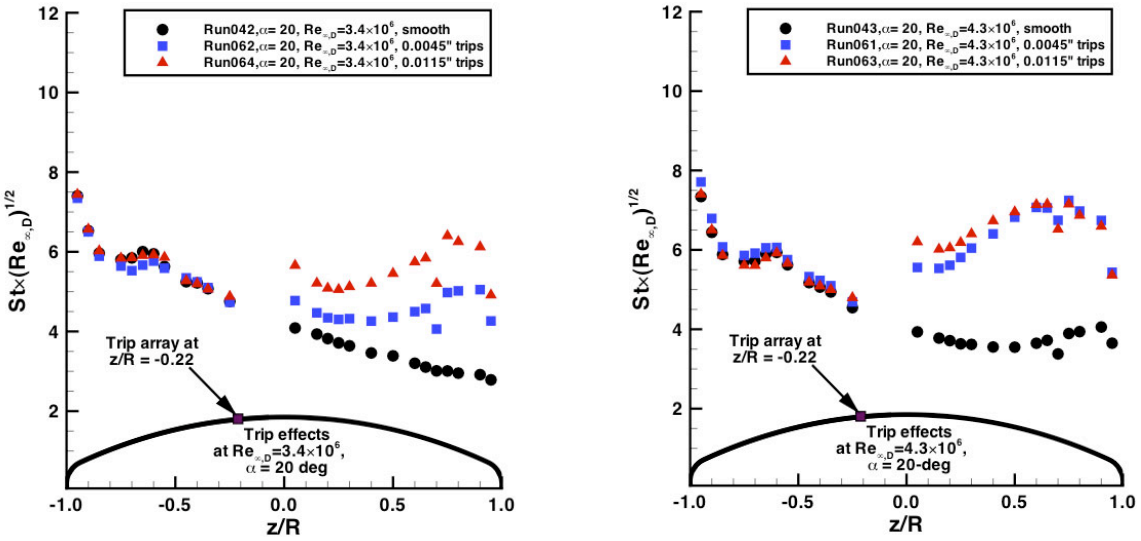

Figure 36. Trip effects at α = 20-deg, $Re_{\infty,D} = 3.4\times10^6$ to 4.3×10^6

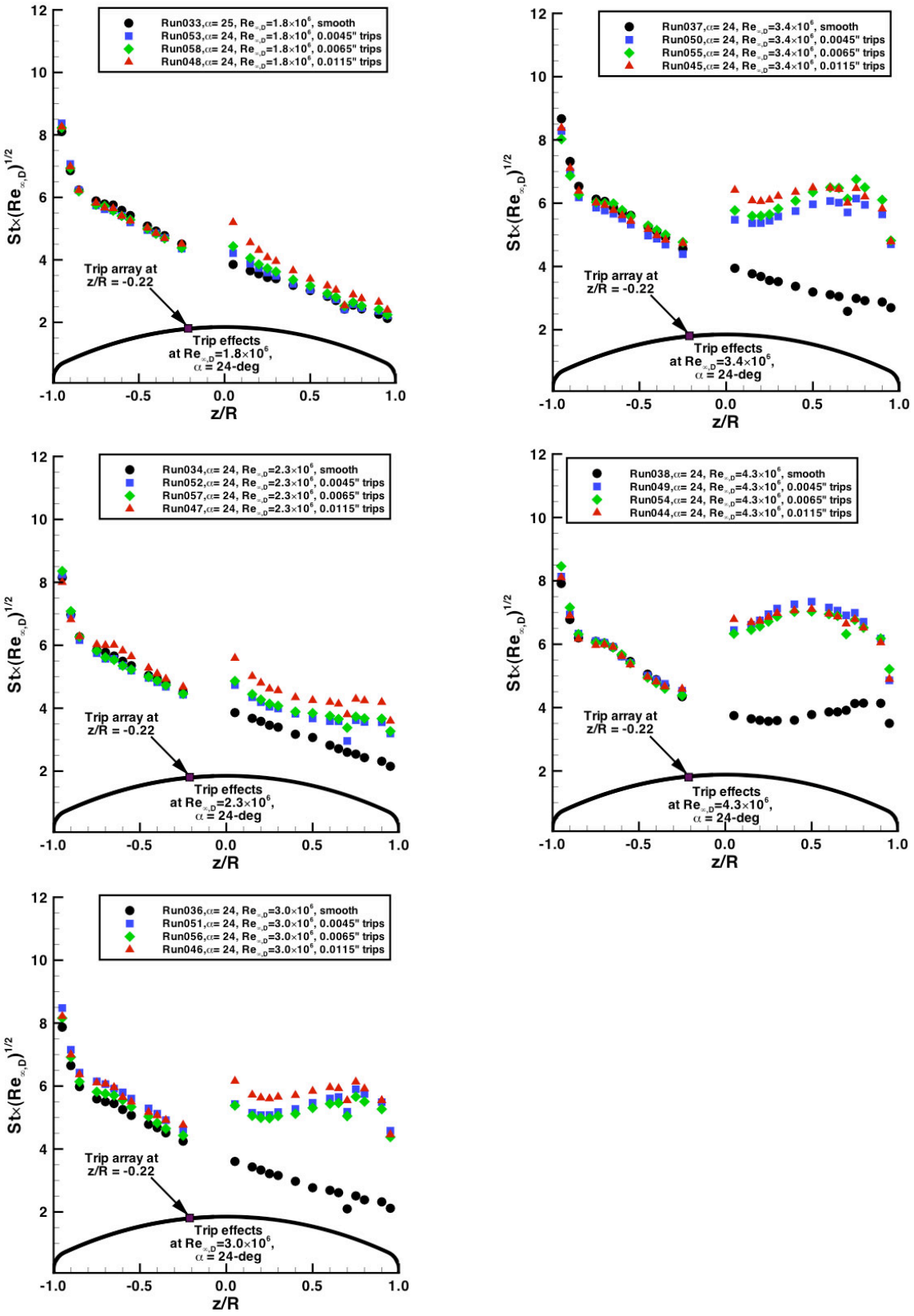

Figure 37. Trip effects at α = 24-deg, $Re_{\infty,D} = 1.8\times10^6$ to 4.3×10^6

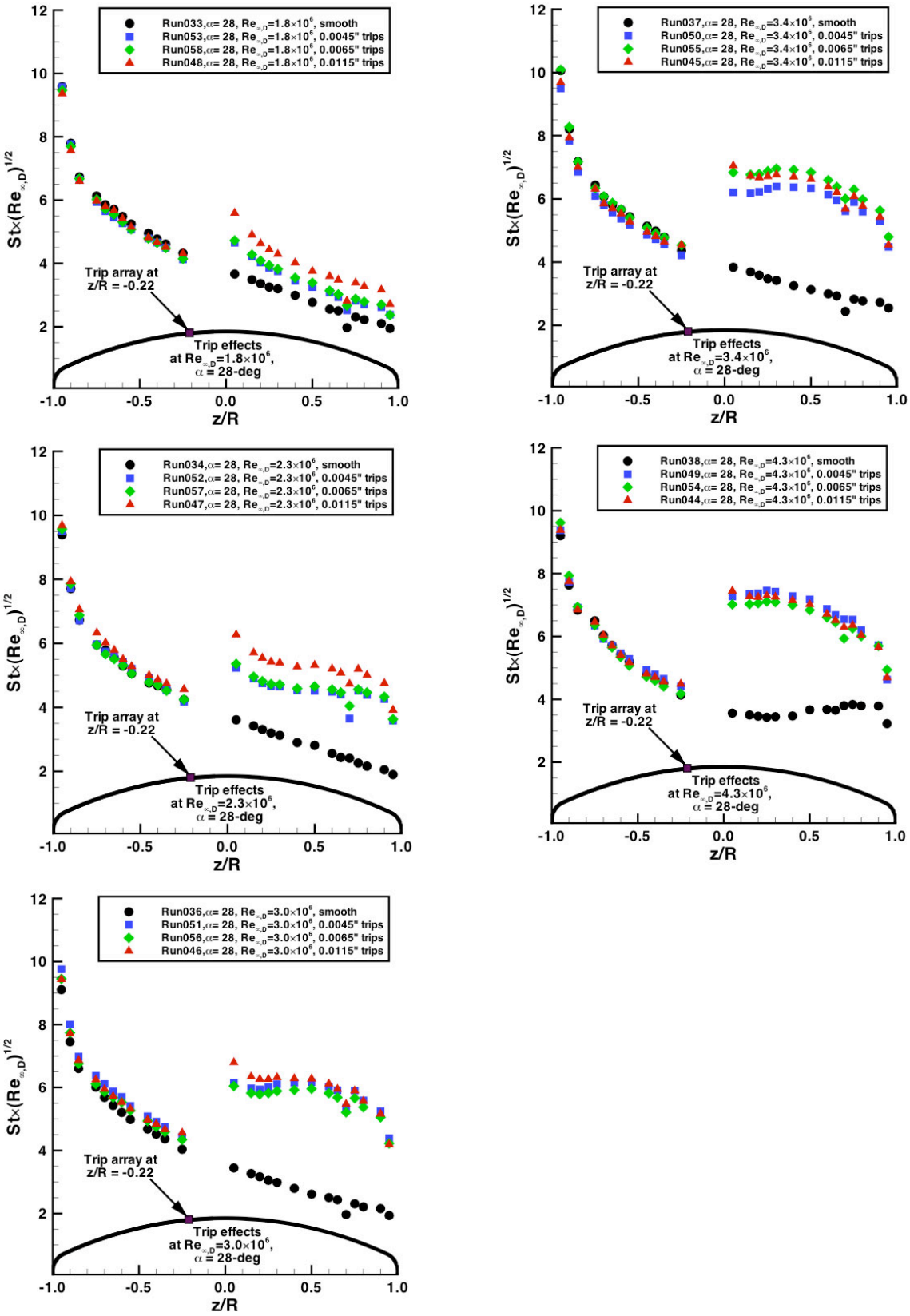

Figure 38. Trip effects at α = 28-deg, $Re_{\infty,D} = 1.8\times10^6$ to 4.3×10^6

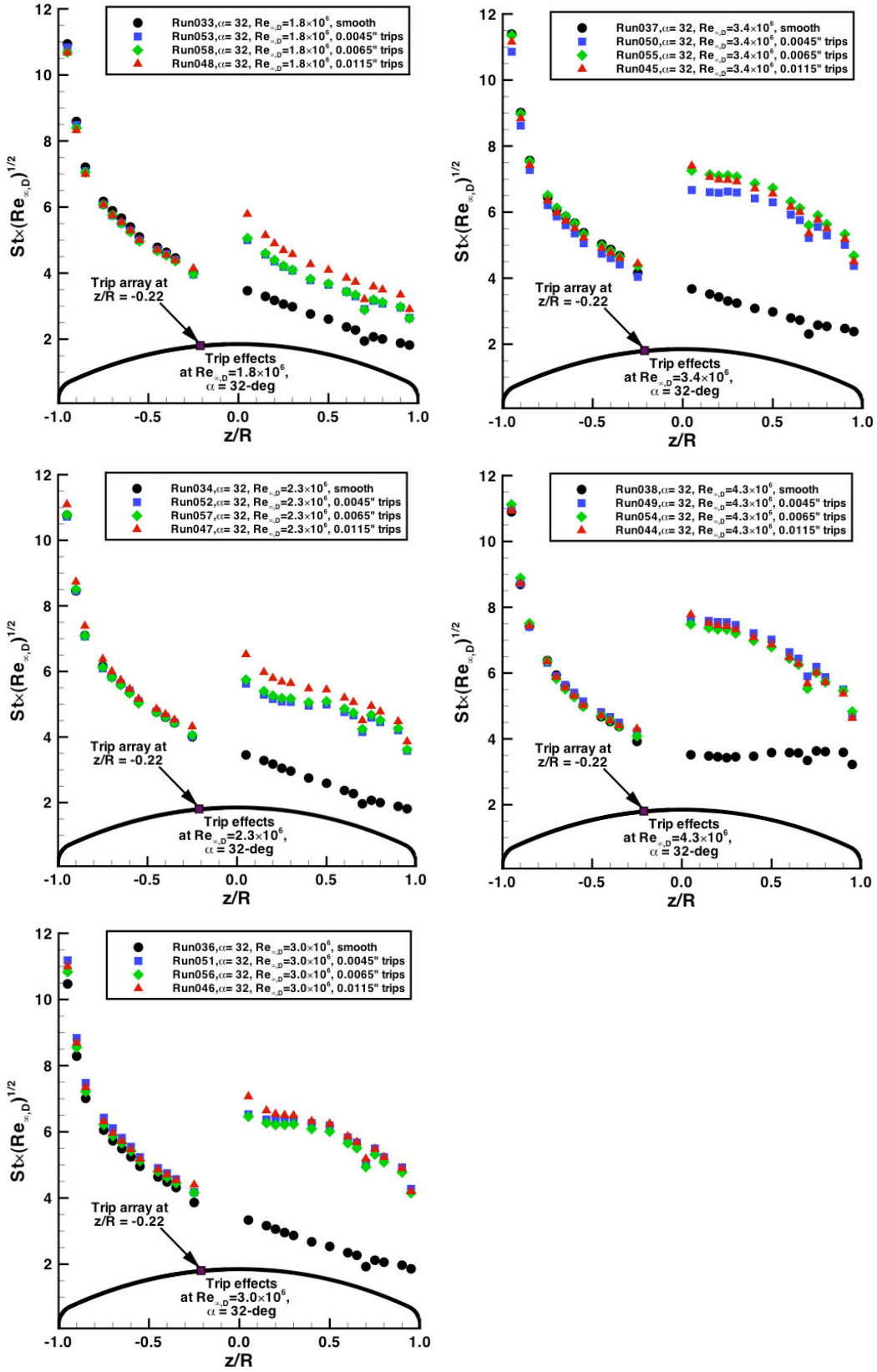

Figure 39. Trip effects at α = 32-deg, $Re_{\infty,D} = 1.8\times10^6$ to 4.3×10^6

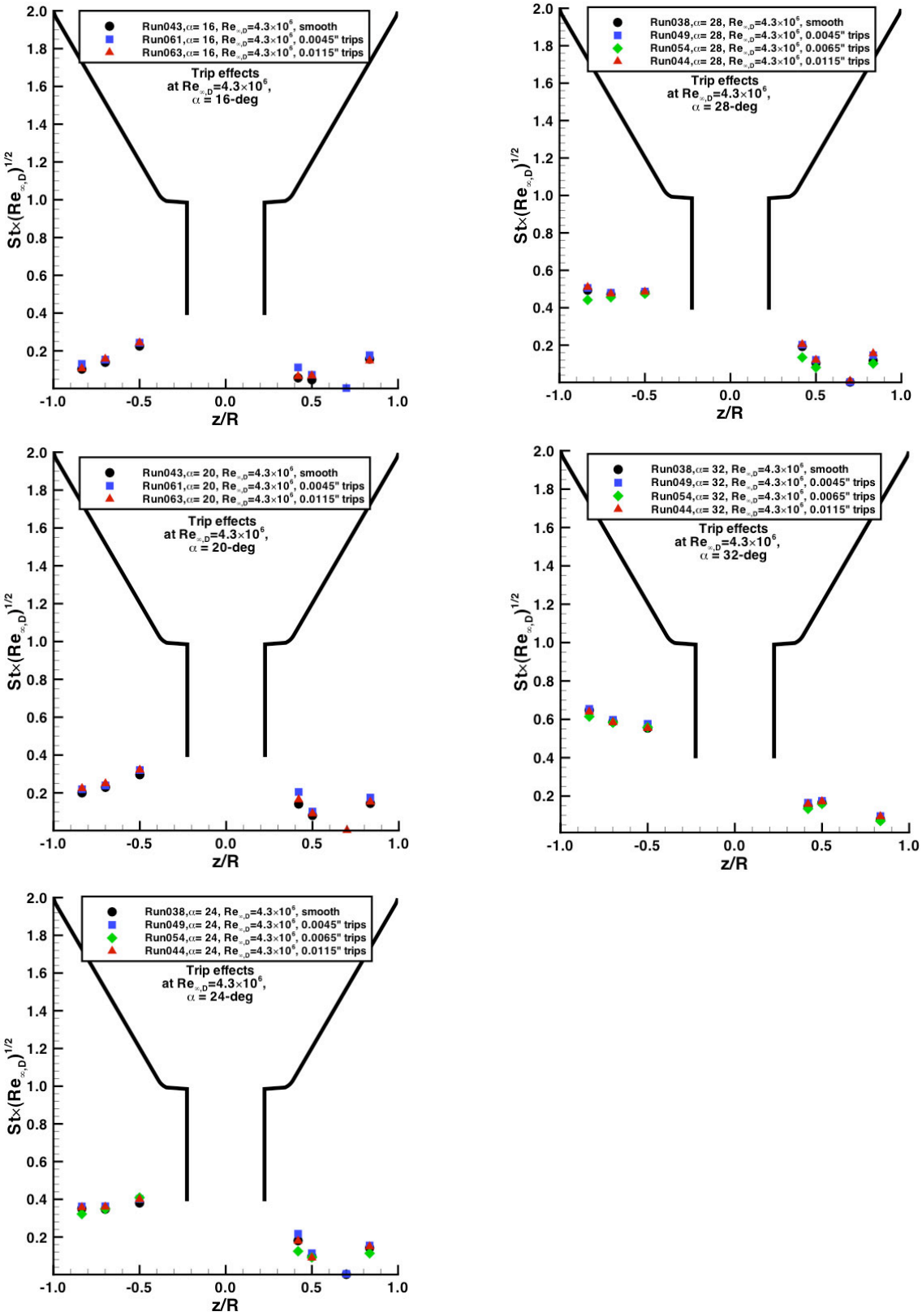

Figure 40. Trip effects on aftbody at $Re_{\infty,D} = 4.3\times10^6$, α = 16-deg to 32-deg

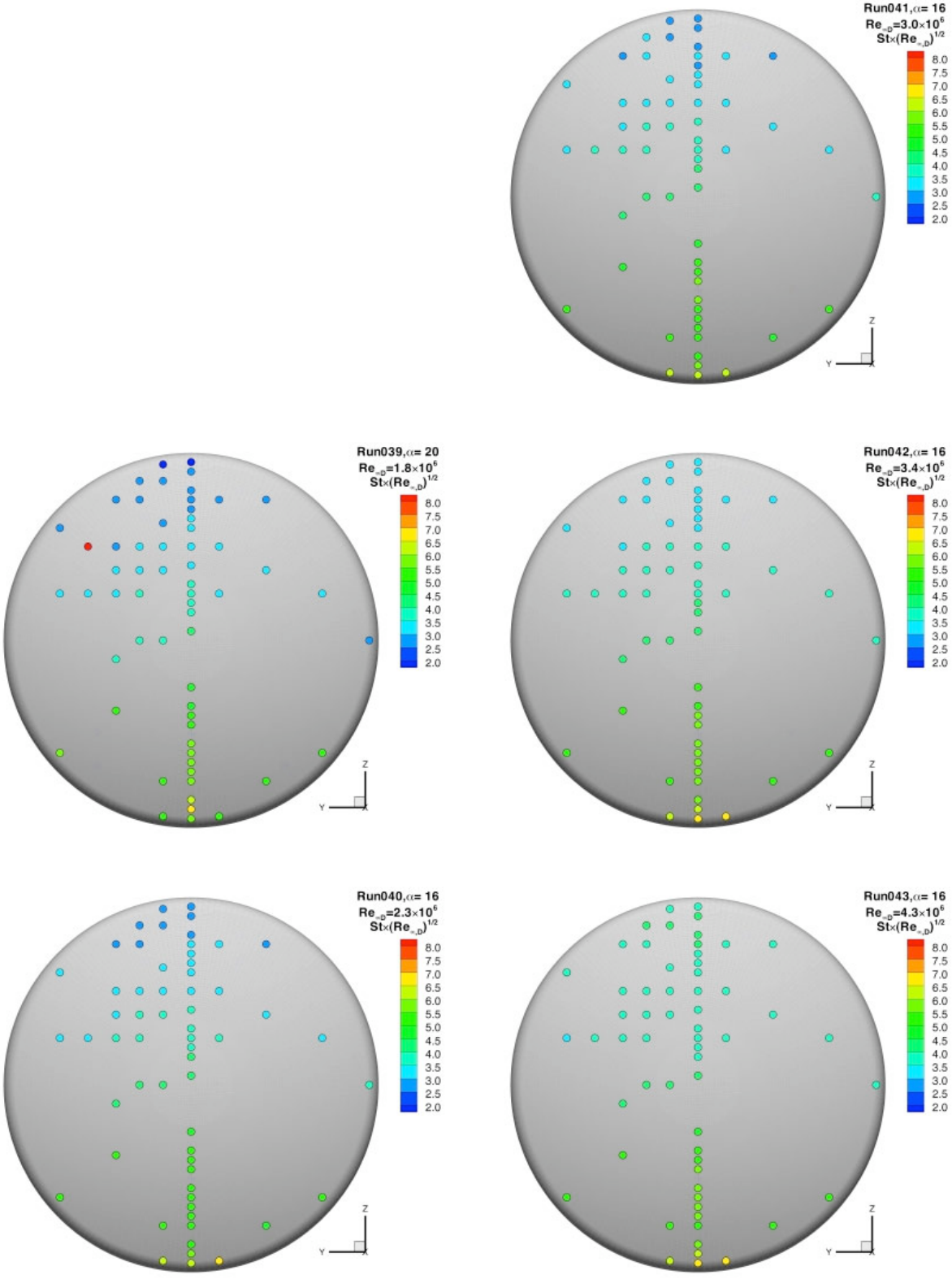

Figure 41. Reynolds numbers effects, α = 16-deg, $Re_{\infty,D} = 1.8\times10^6$ to 4.3×10^6

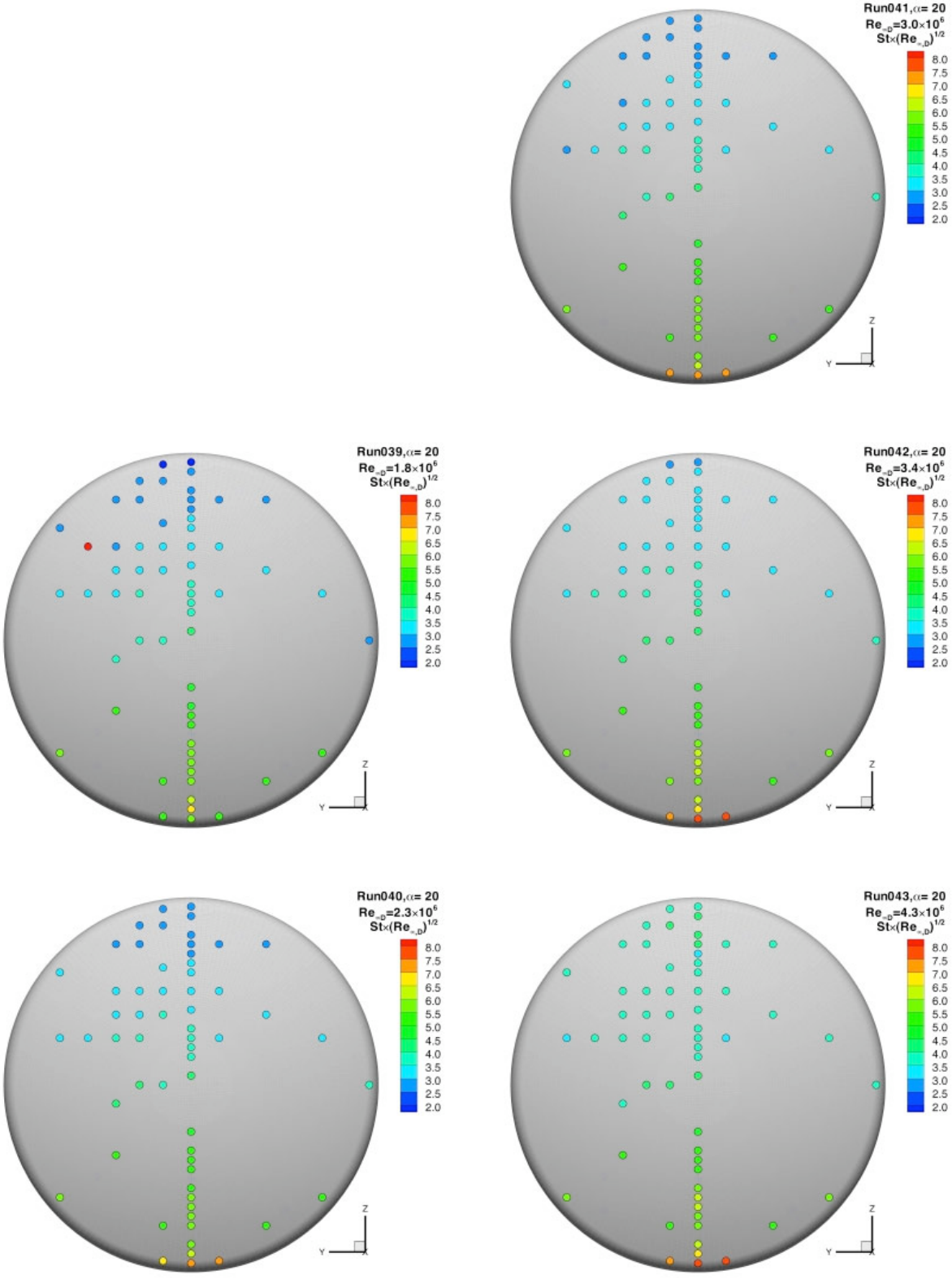

Figure 42. Reynolds numbers effects, α = 20-deg, $Re_{\infty,D} = 1.8\times10^6$ to 4.3×10^6

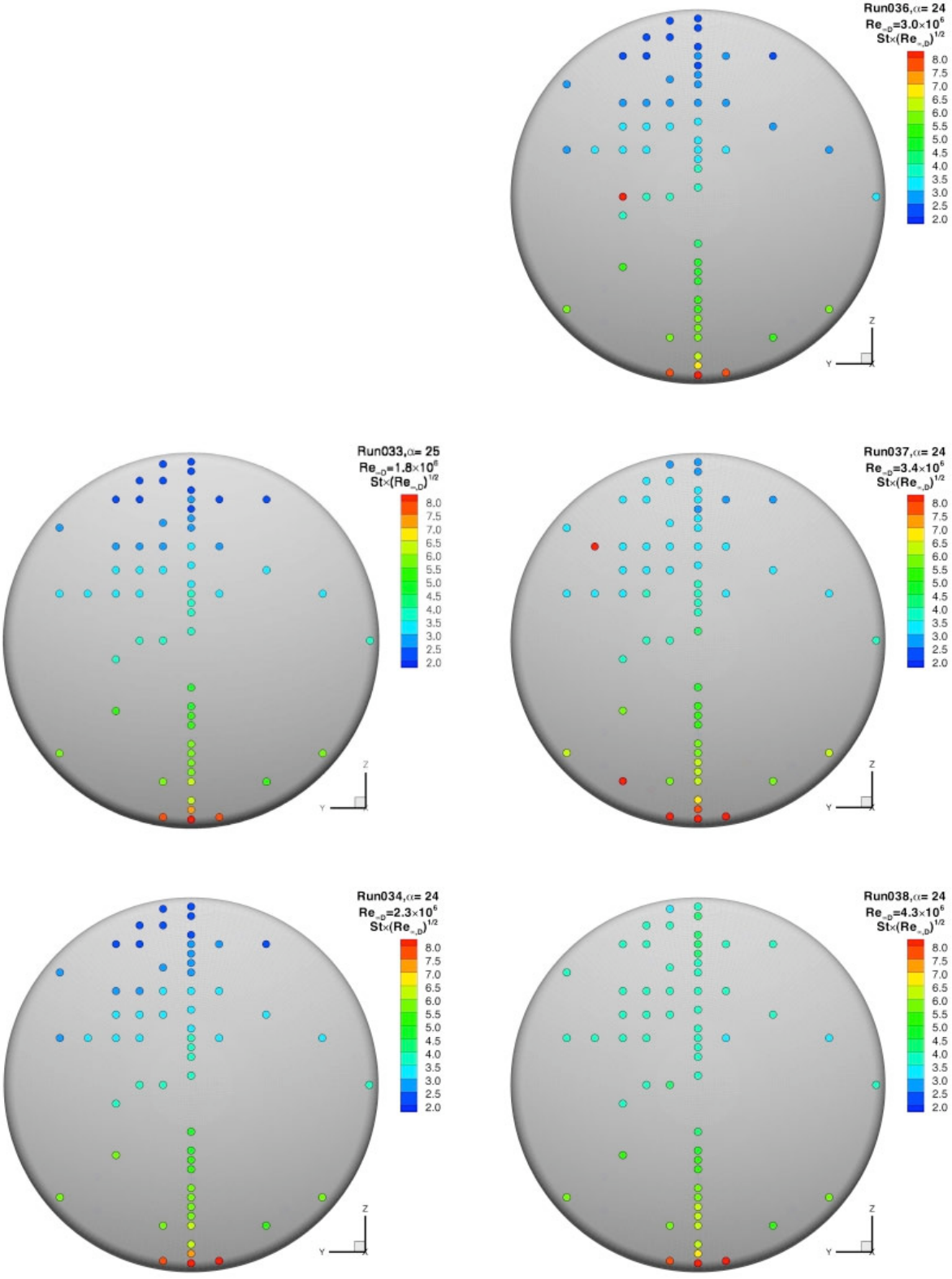

Figure 43. Reynolds numbers effects, α = 24-deg, $Re_{\infty,D} = 1.8\times10^6$ to 4.3×10^6

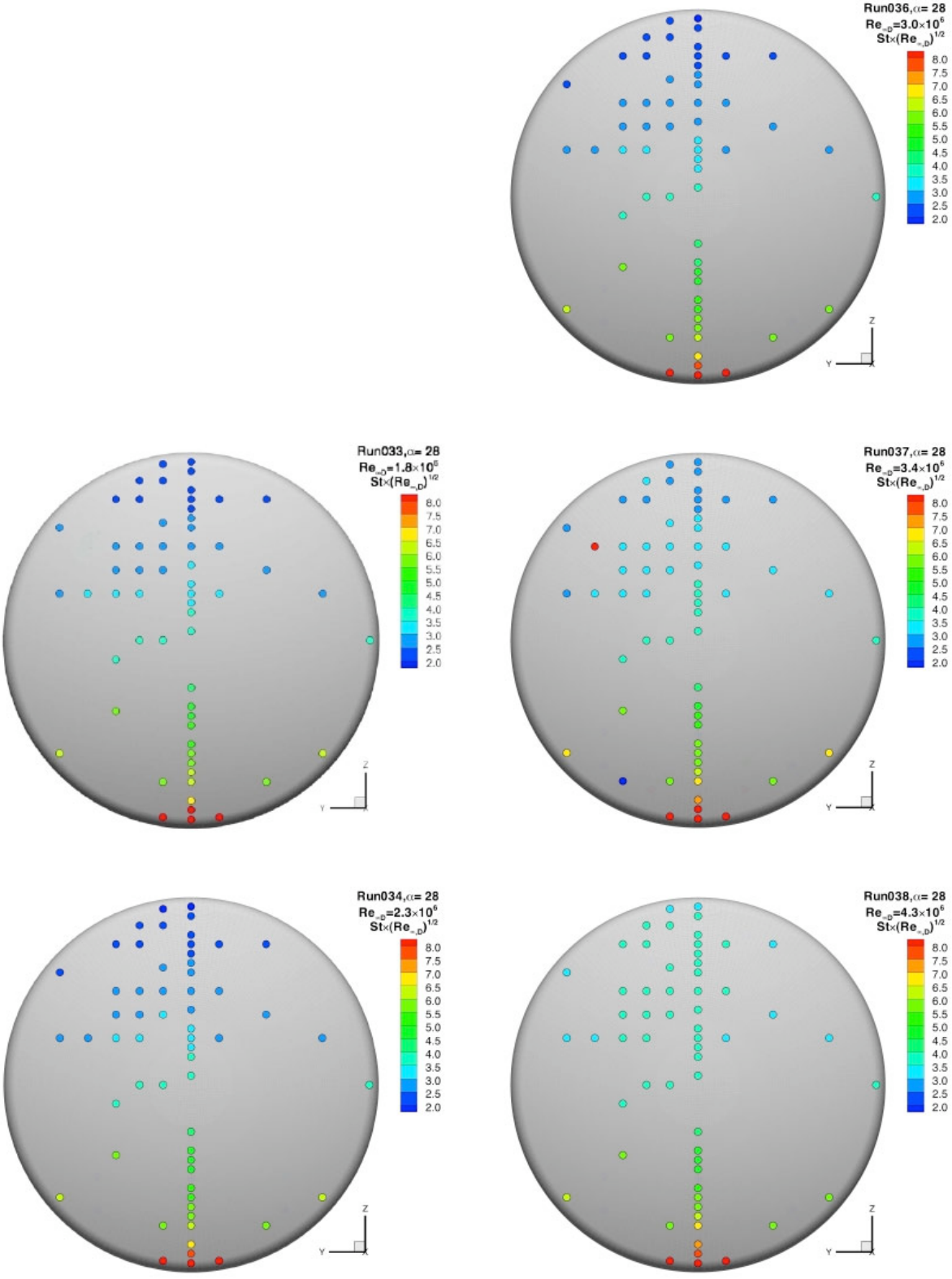

Figure 44. Reynolds numbers effects, α = 28-deg, $Re_{\infty,D} = 1.8\times10^6$ to 4.3×10^6

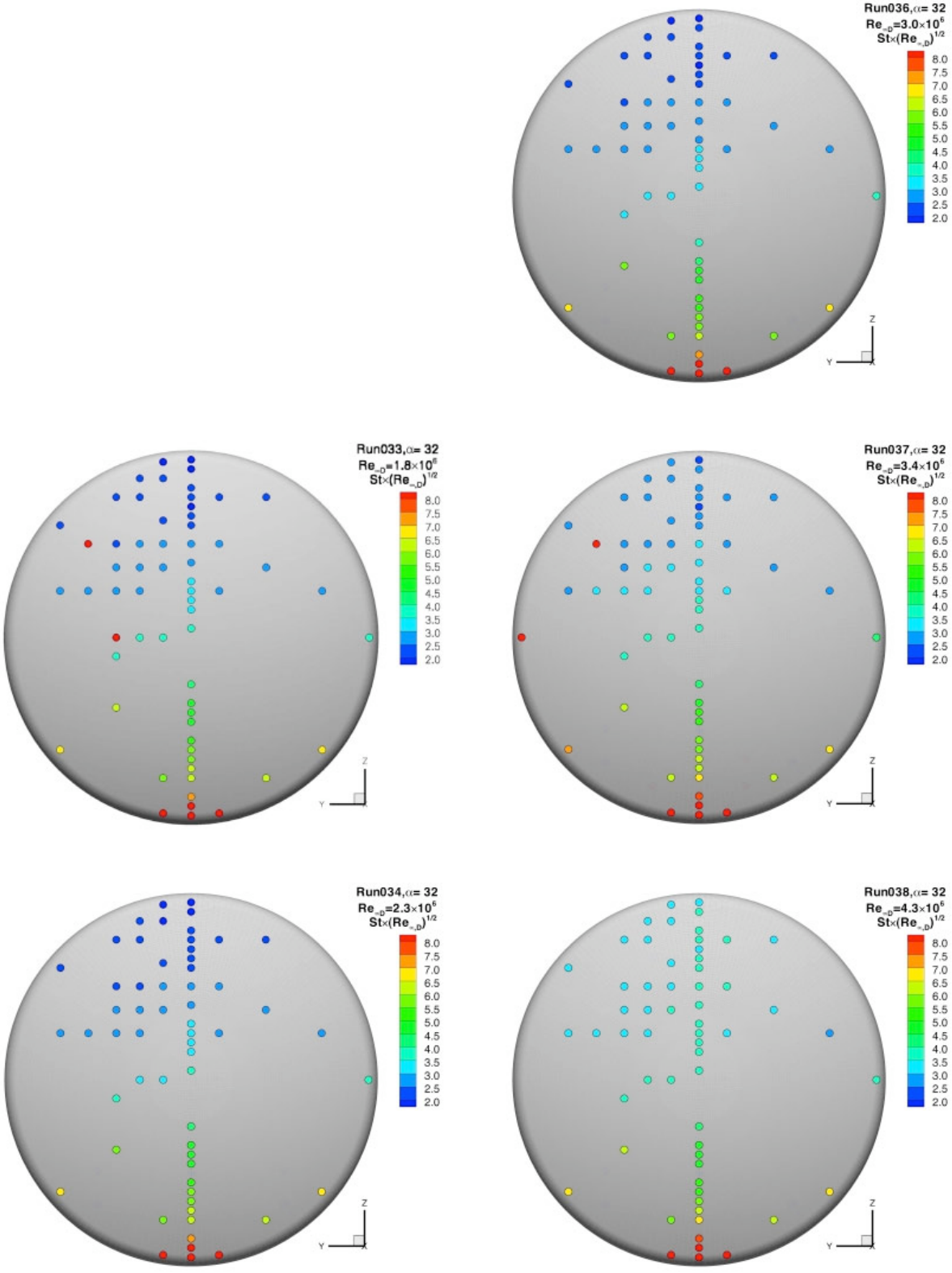

Figure 45. Reynolds numbers effects, α = 32-deg, $Re_{\infty,D} = 1.8\times10^6$ to 4.3×10^6

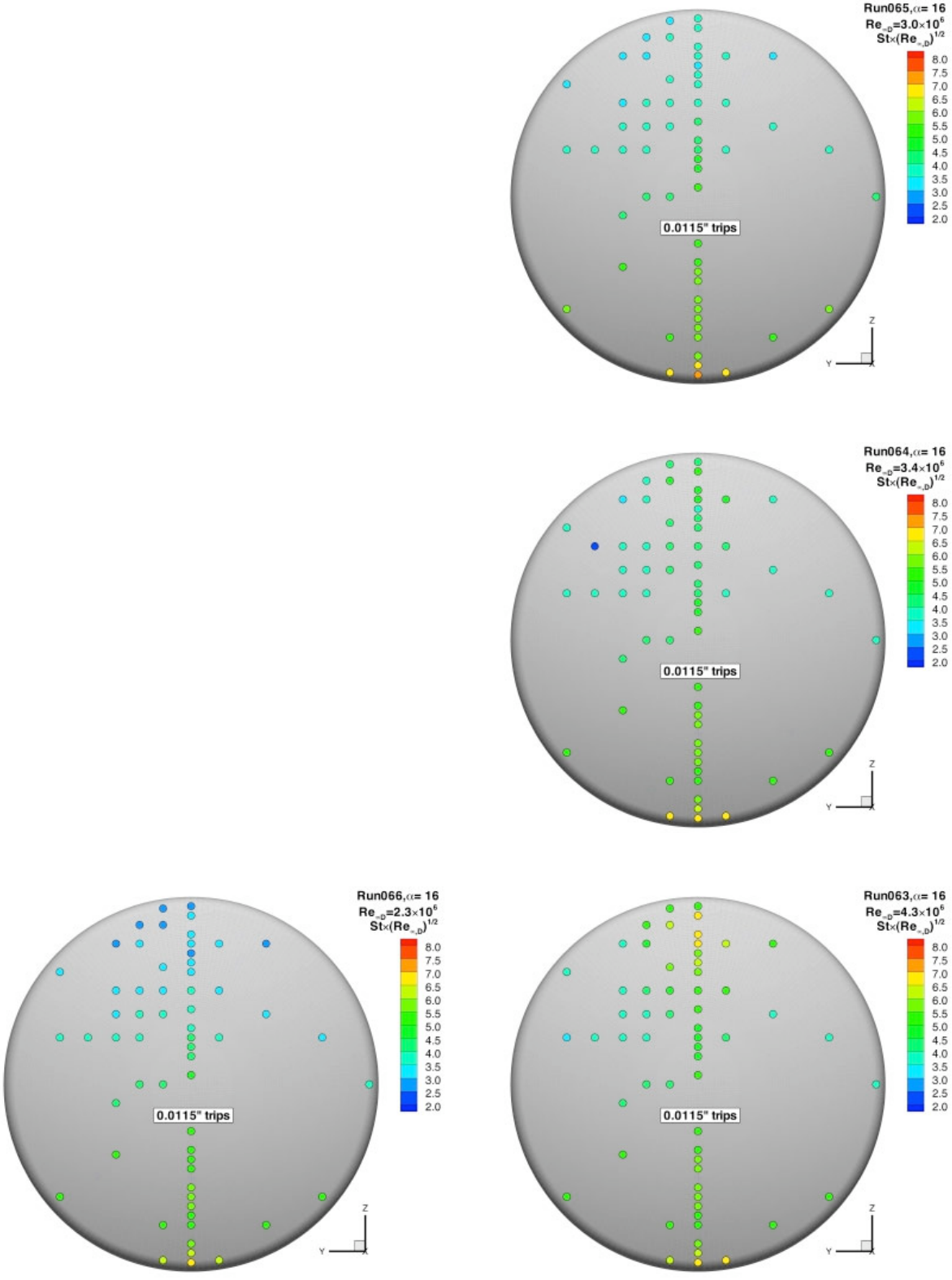

Figure 46. Reynolds numbers effects with trips, α = 16-deg, $Re_{\infty,D} = 2.3\times10^6$ to 4.3×10^6

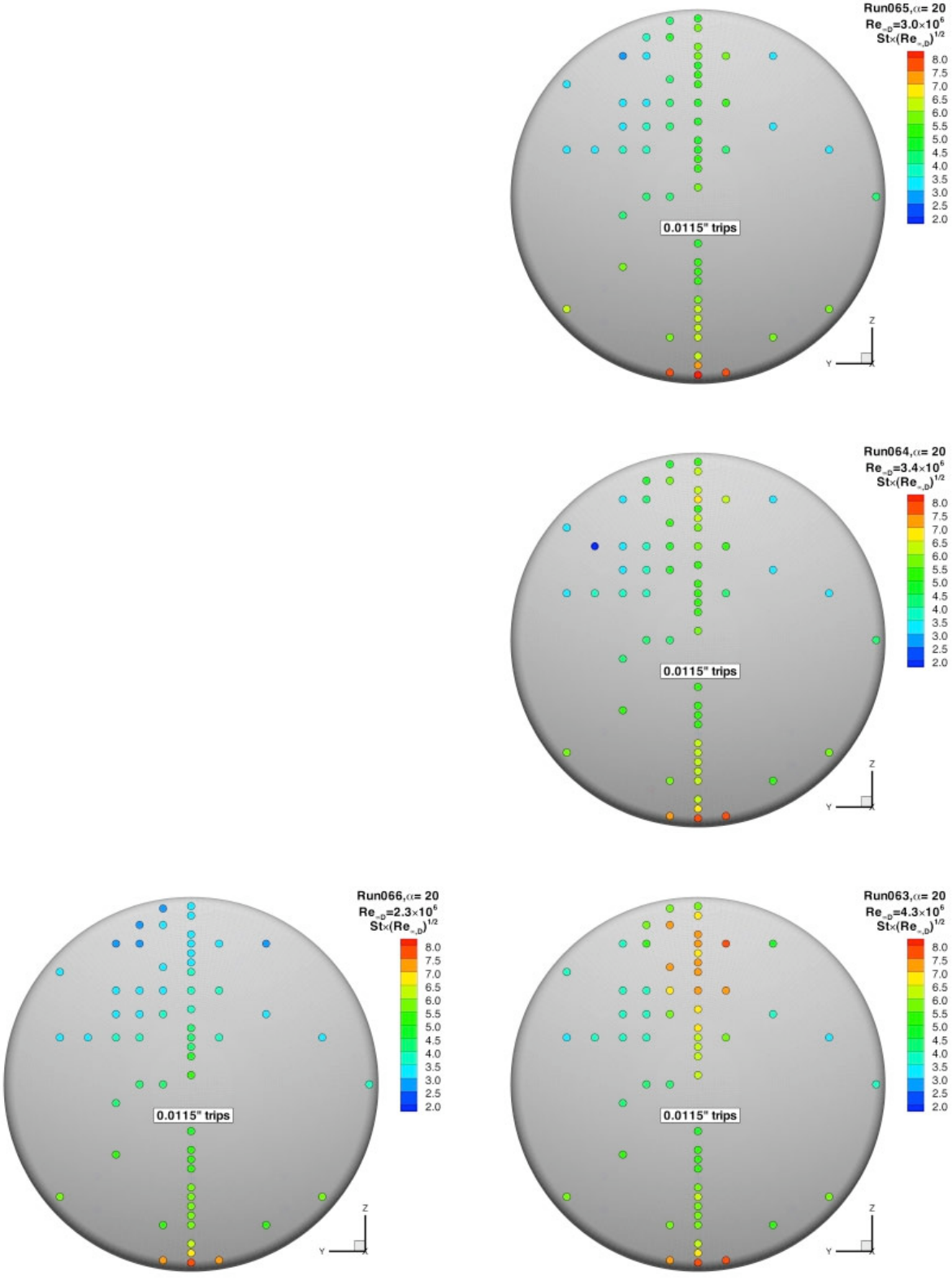

Figure 47. Reynolds numbers effects with trips, α = 20-deg, $Re_{\infty,D} = 2.3\times10^6$ to 4.3×10^6

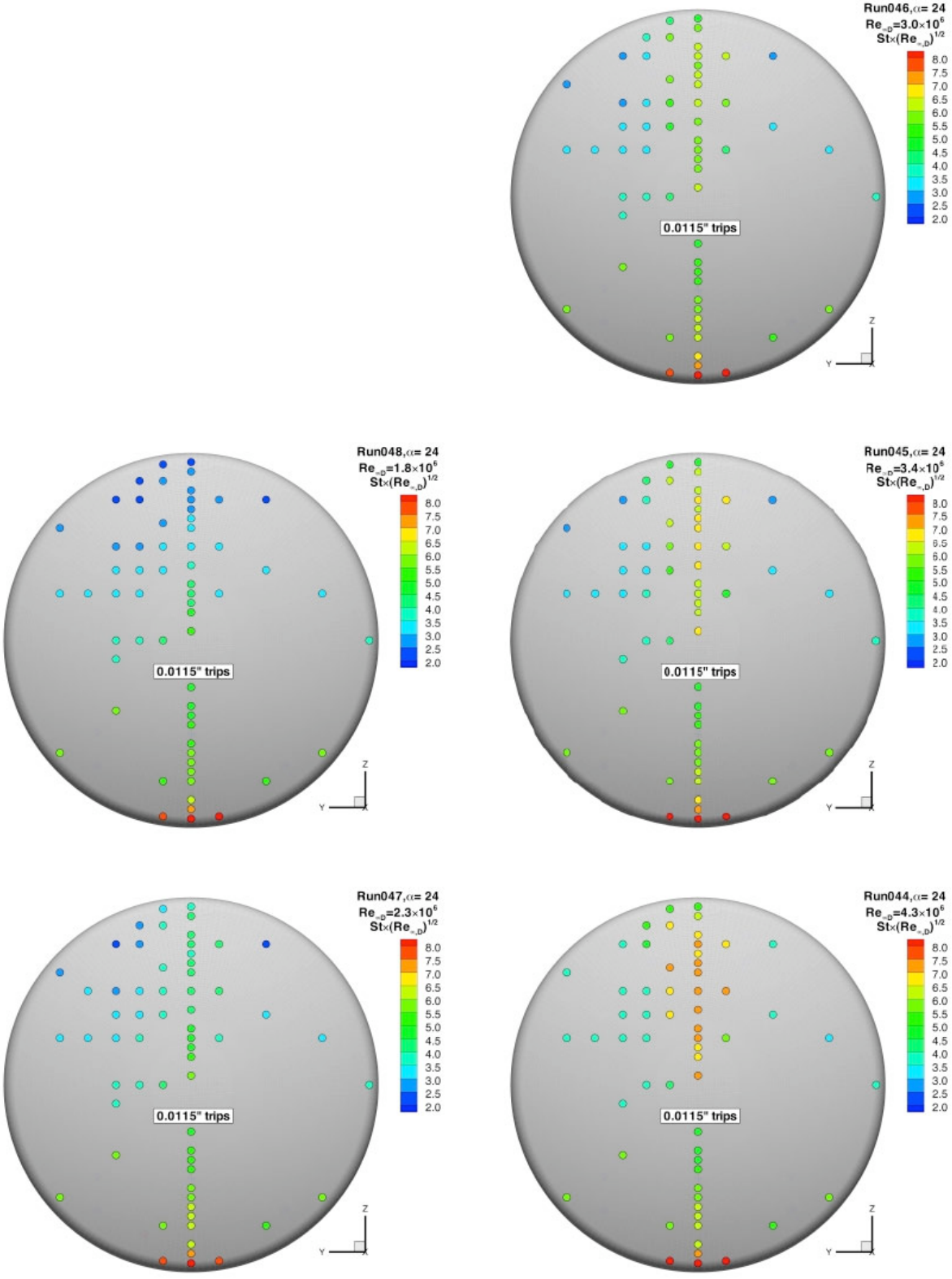

Figure 48. Reynolds numbers effects with trips, α = 24-deg, $Re_{\infty,D} = 1.8\times10^6$ to 4.3×10^6

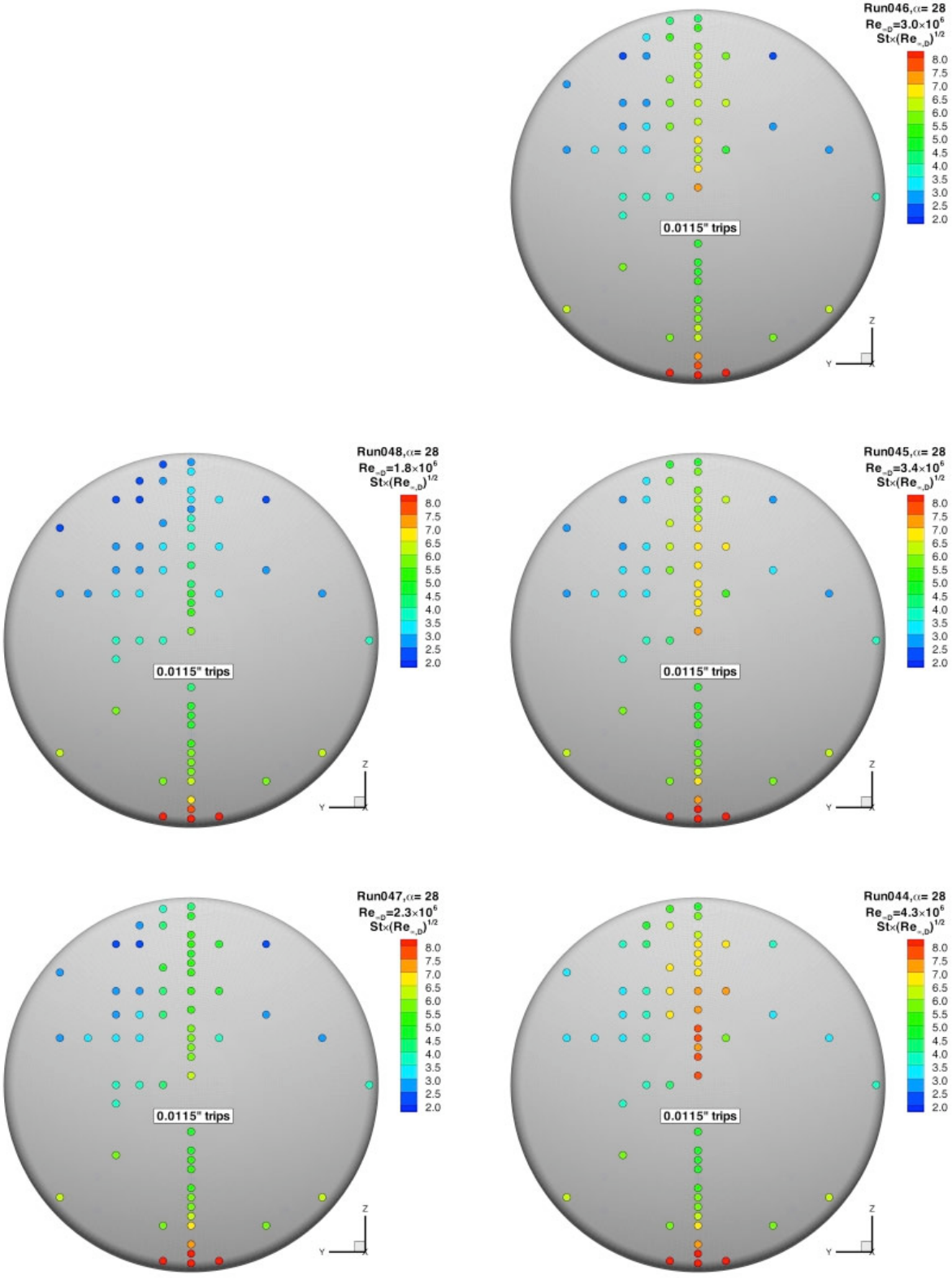

Figure 49. Reynolds numbers effects with trips, α = 28-deg, $Re_{\infty,D} = 1.8\times10^6$ to 4.3×10^6

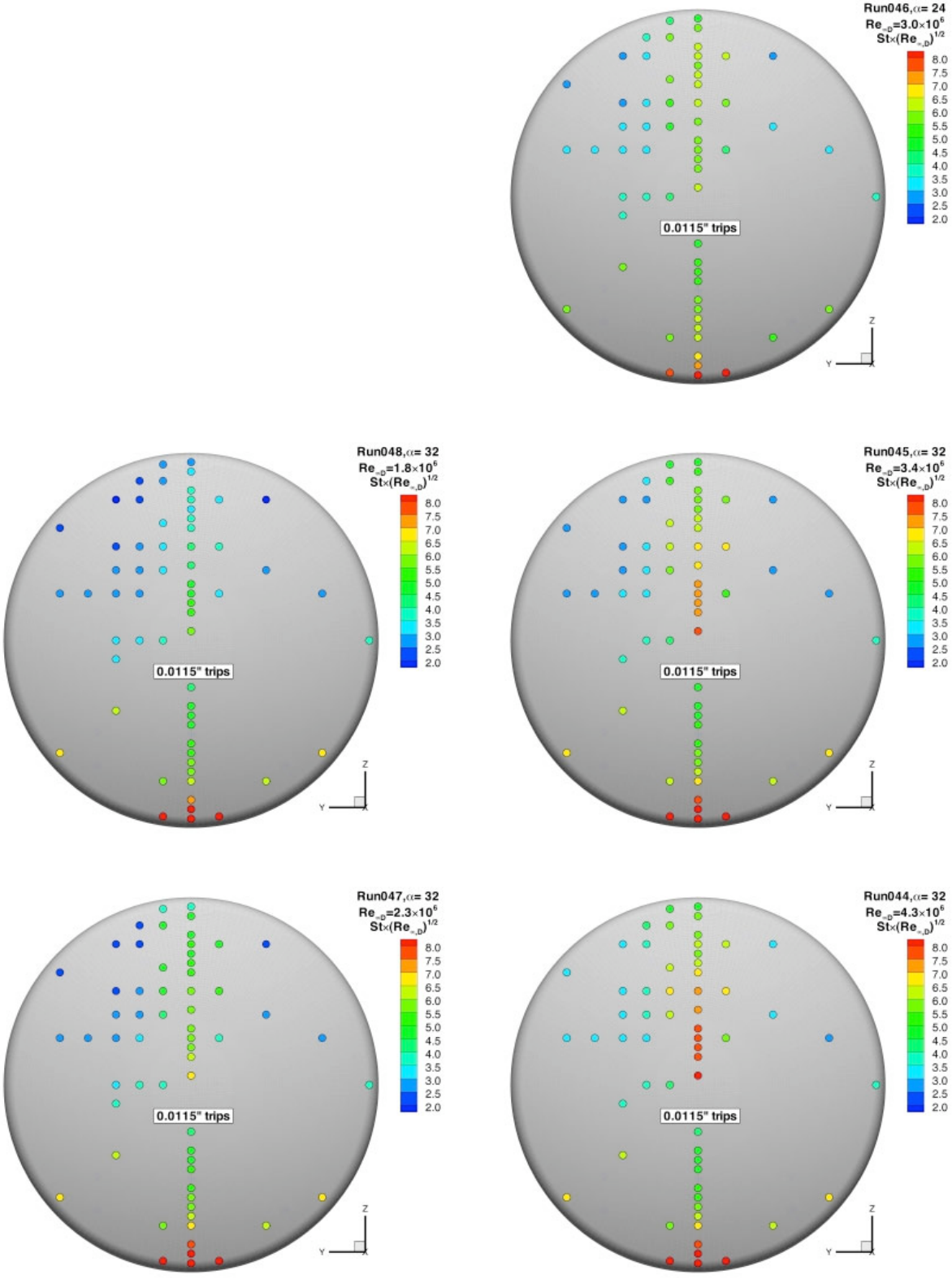

Figure 50. Reynolds numbers effects with trips, α = 32-deg, $Re_{\infty,D} = 1.8\times10^6$ to 4.3×10^6

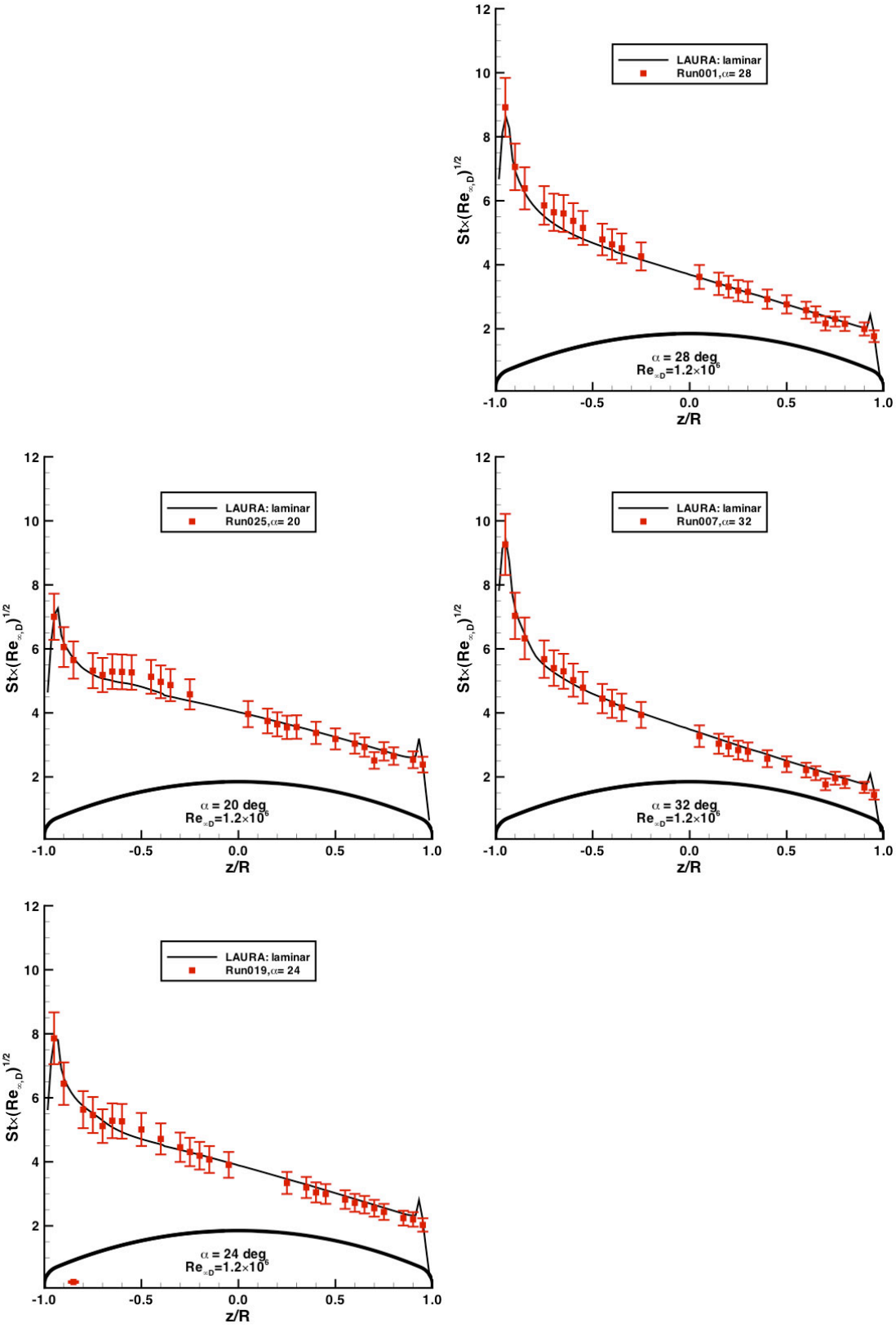

Figure 51. Comparison with laminar predictions, $Re_{\infty,D} = 1.2\times10^6$, α = 20-deg to 32-deg

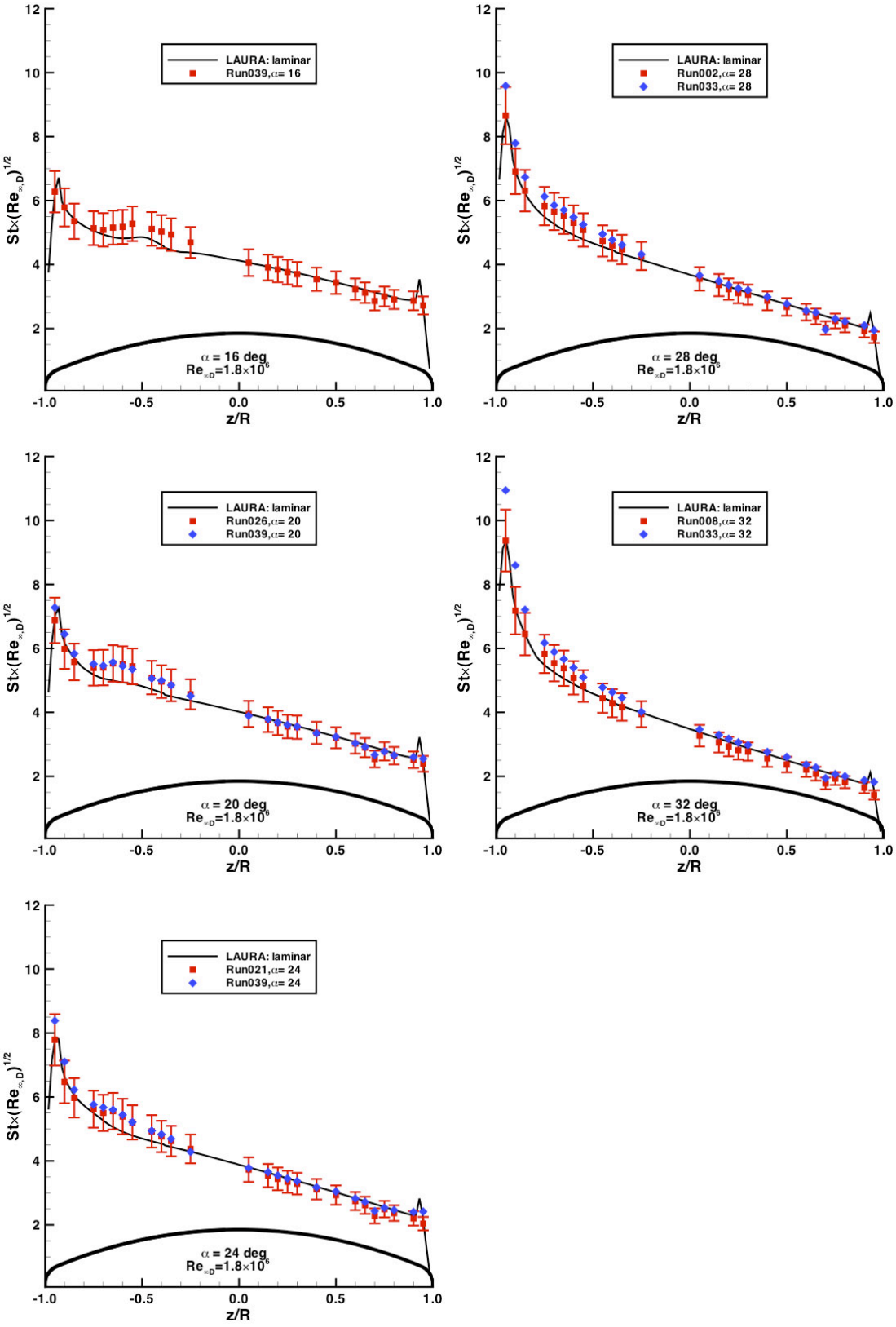

Figure 52. Comparison with laminar predictions, $Re_{\infty,D} = 1.8\times10^6$, α = 16-deg to 32-deg

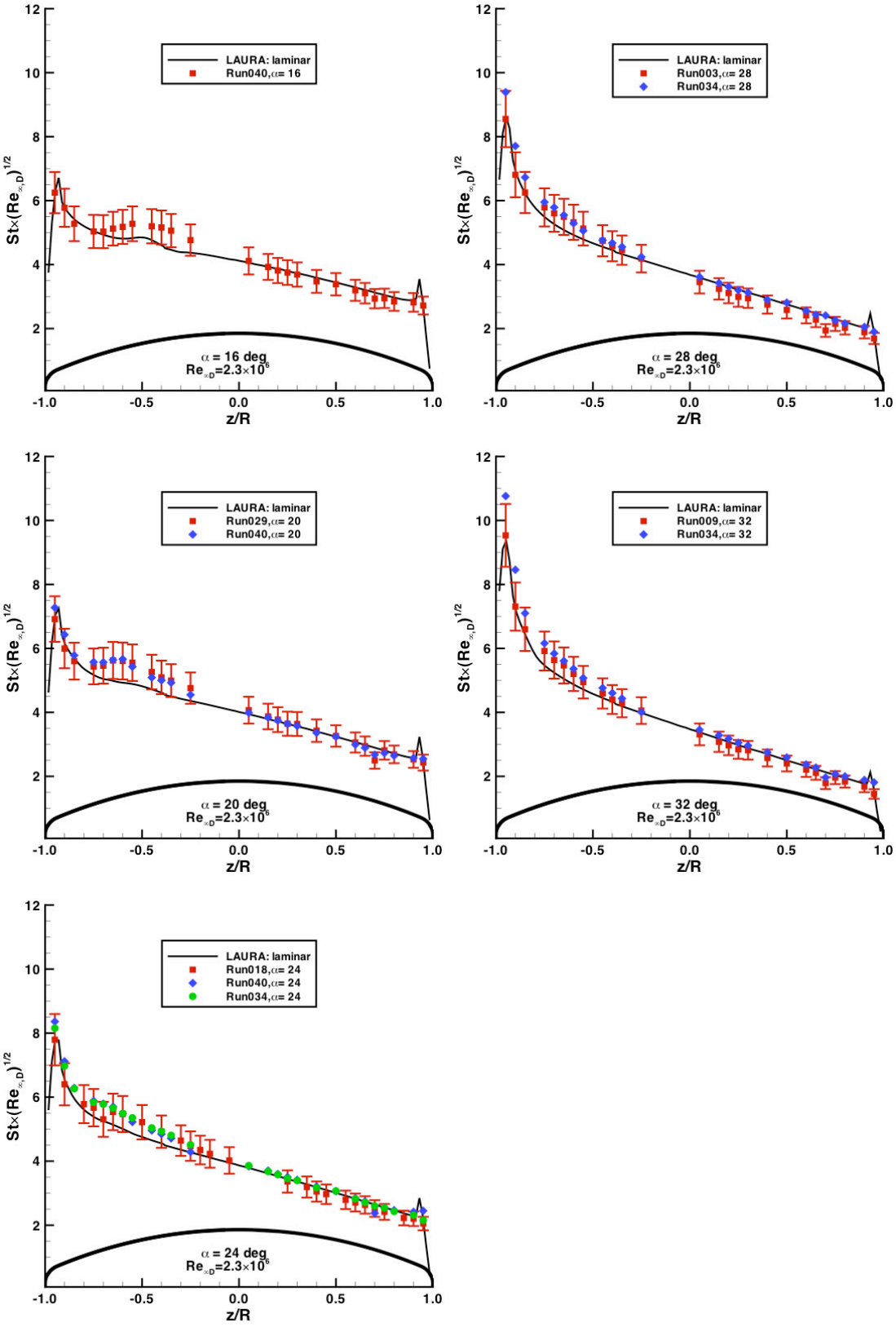

Figure 53. Comparison with laminar predictions, $Re_{\infty,D} = 2.3\times10^6$, α = 16-deg to 32-deg

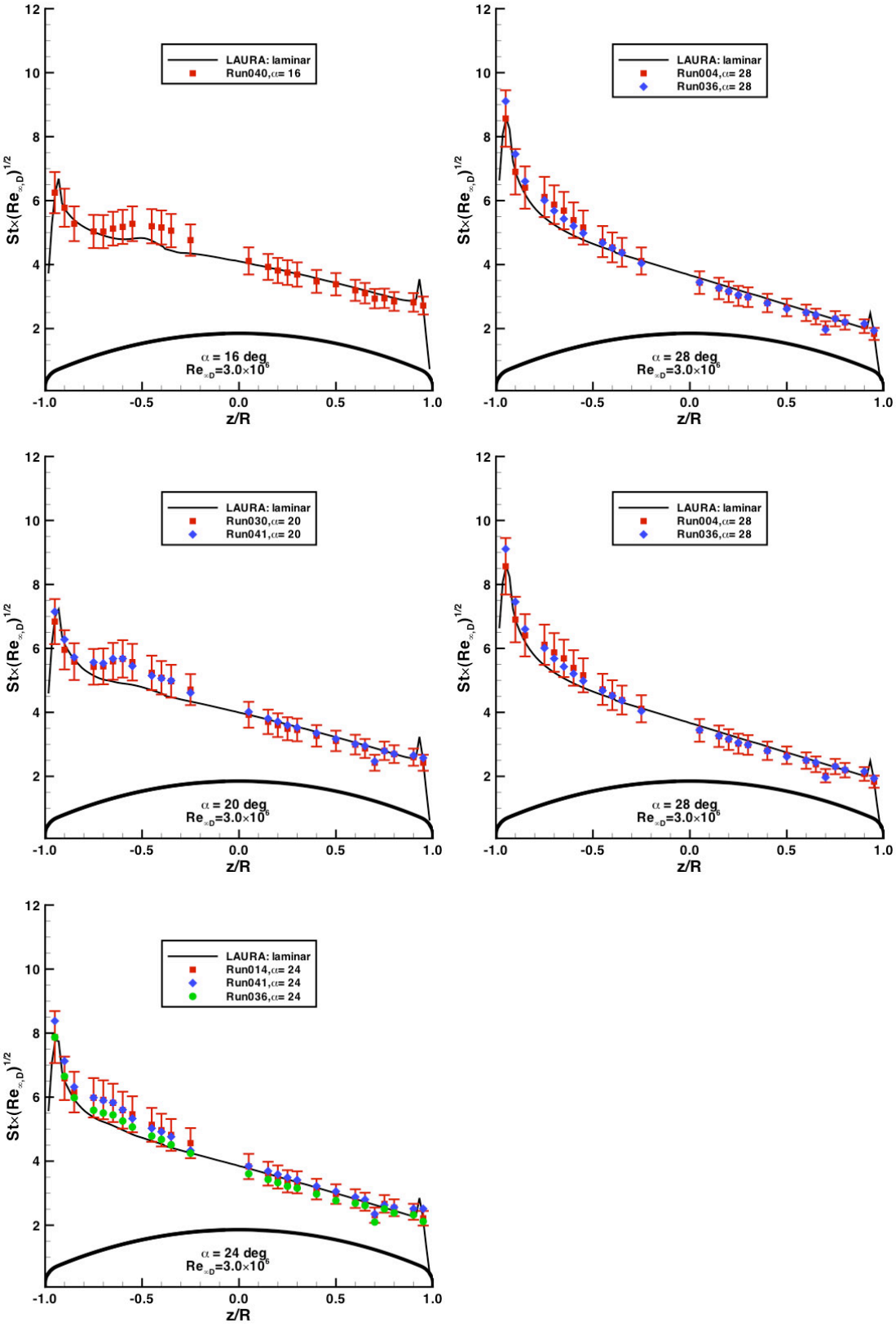

Figure 54. Comparison with laminar predictions, $Re_{\infty,D} = 3.0\times10^6$, α = 16-deg to 32-deg

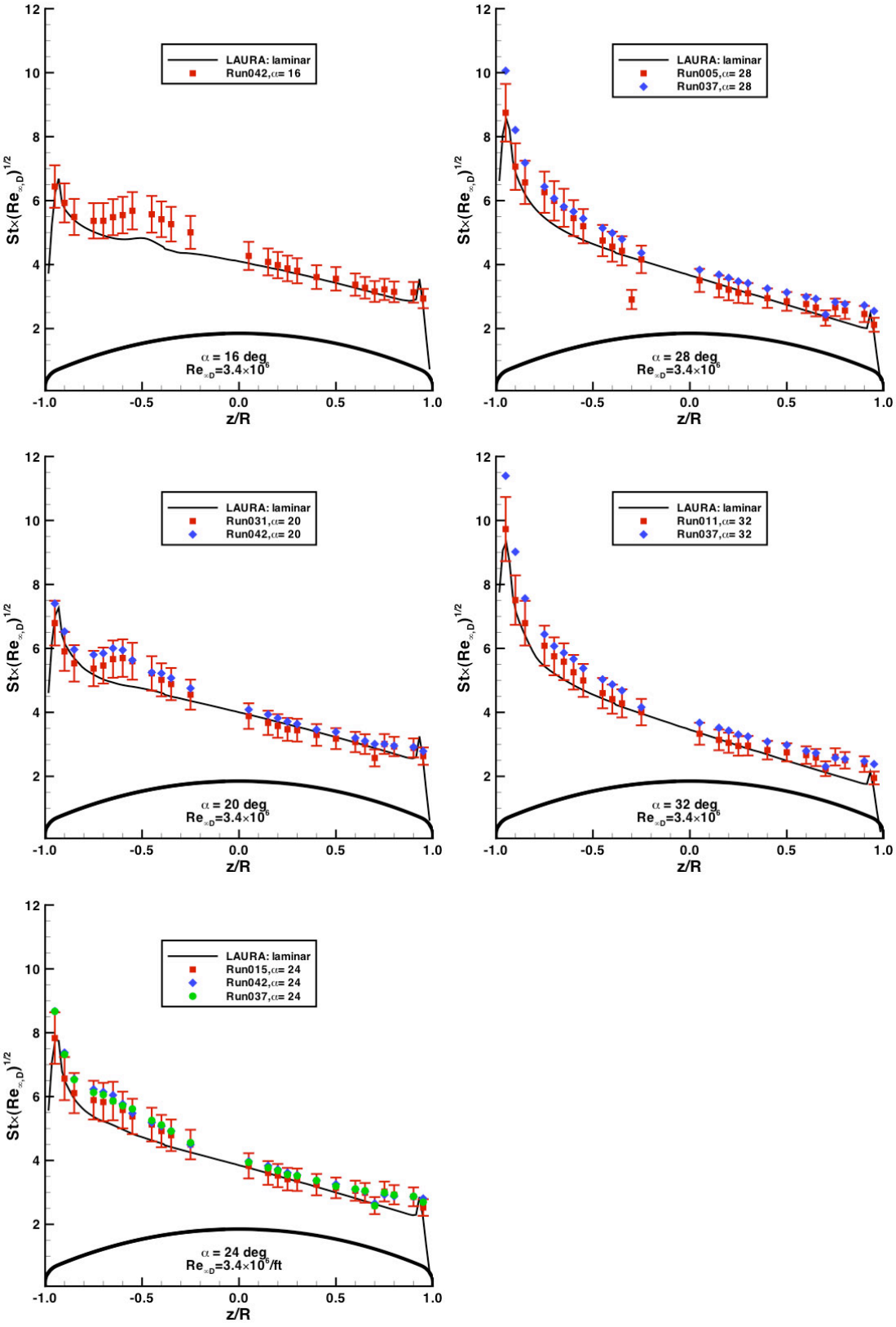

Figure 55. Comparison with laminar predictions, $Re_{\infty,D} = 3.4\times10^6$, α = 16-deg to 32-deg

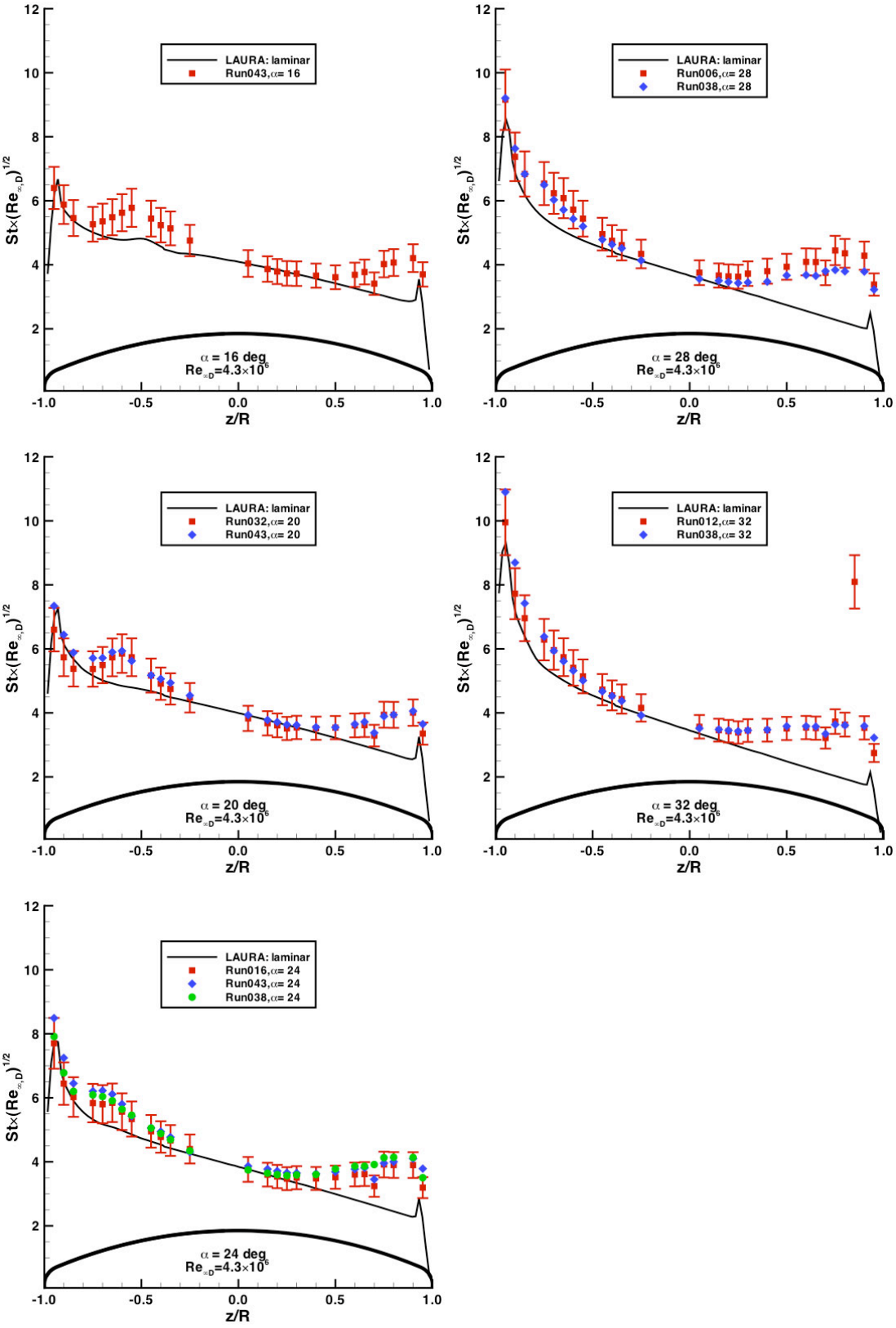

Figure 56. Comparison with laminar predictions, $Re_{\infty,D} = 4.3\times10^6$, α = 16-deg to 32-deg

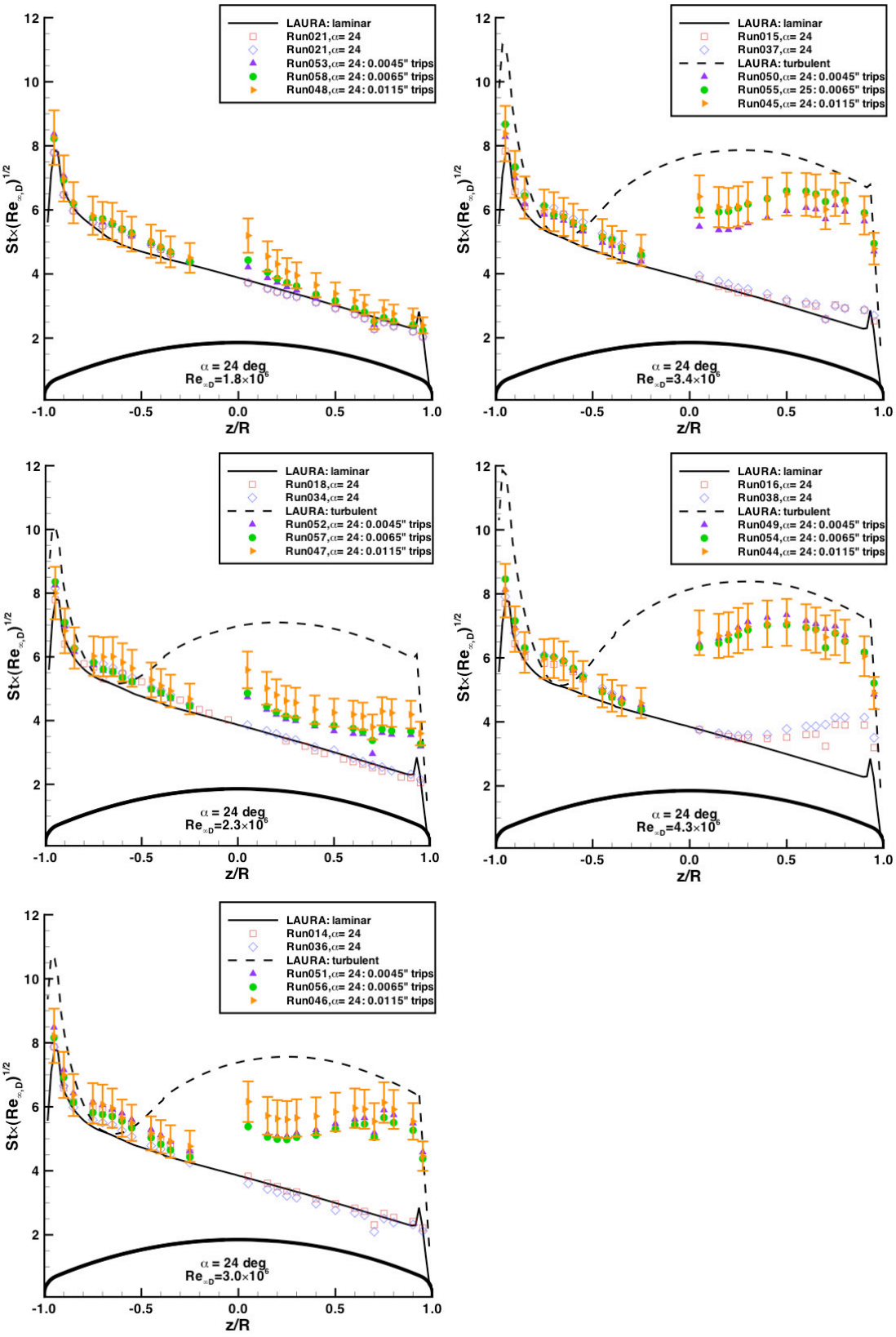

Figure 57. Trip effects on heating, α = 24-deg, $Re_{\infty,D} = 1.8\times10^6$ to 4.3×10^6

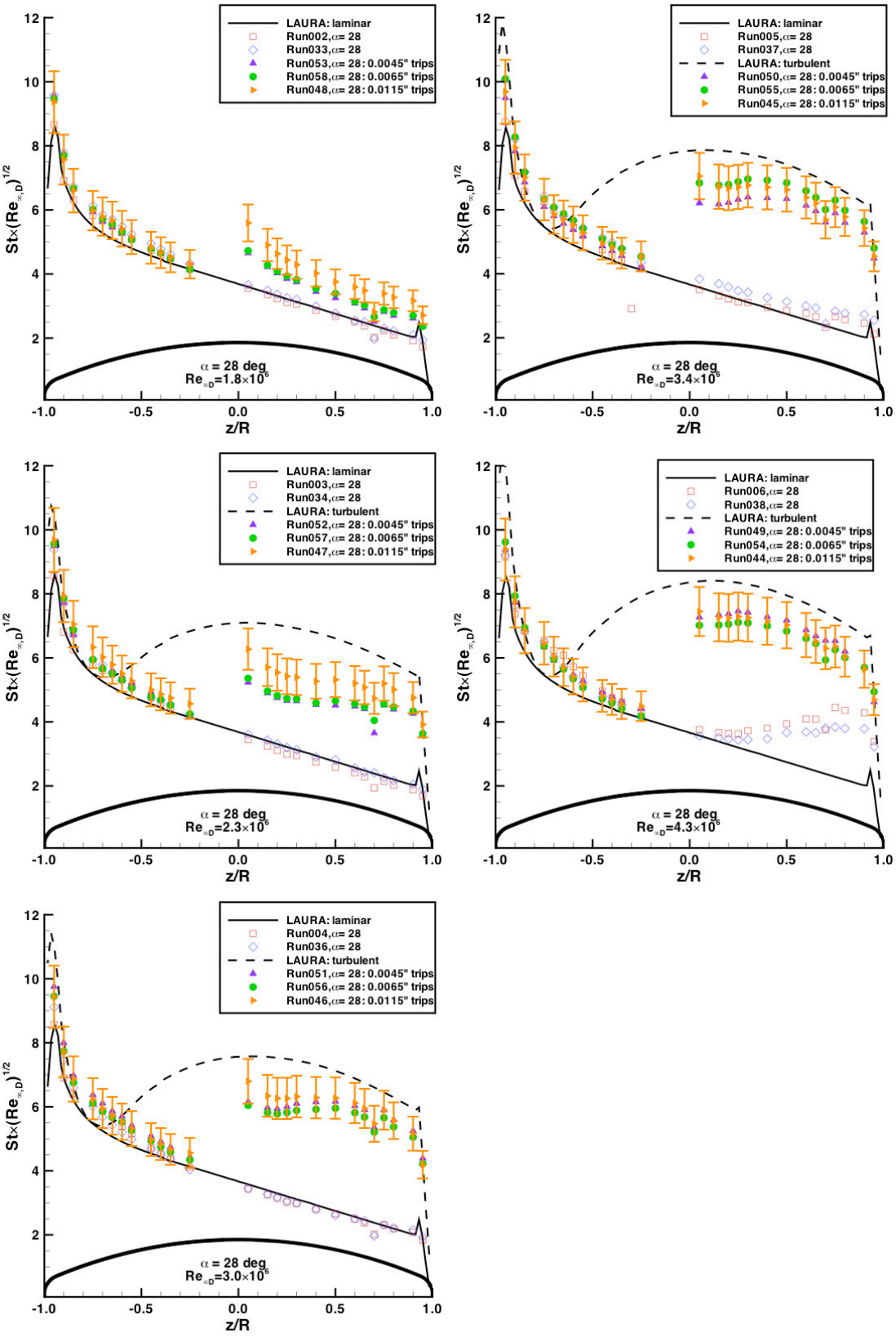

Figure 58. Trip effects on heating, α = 28-deg, $Re_{\infty,D} = 1.8\times10^6$ to 4.3×10^6

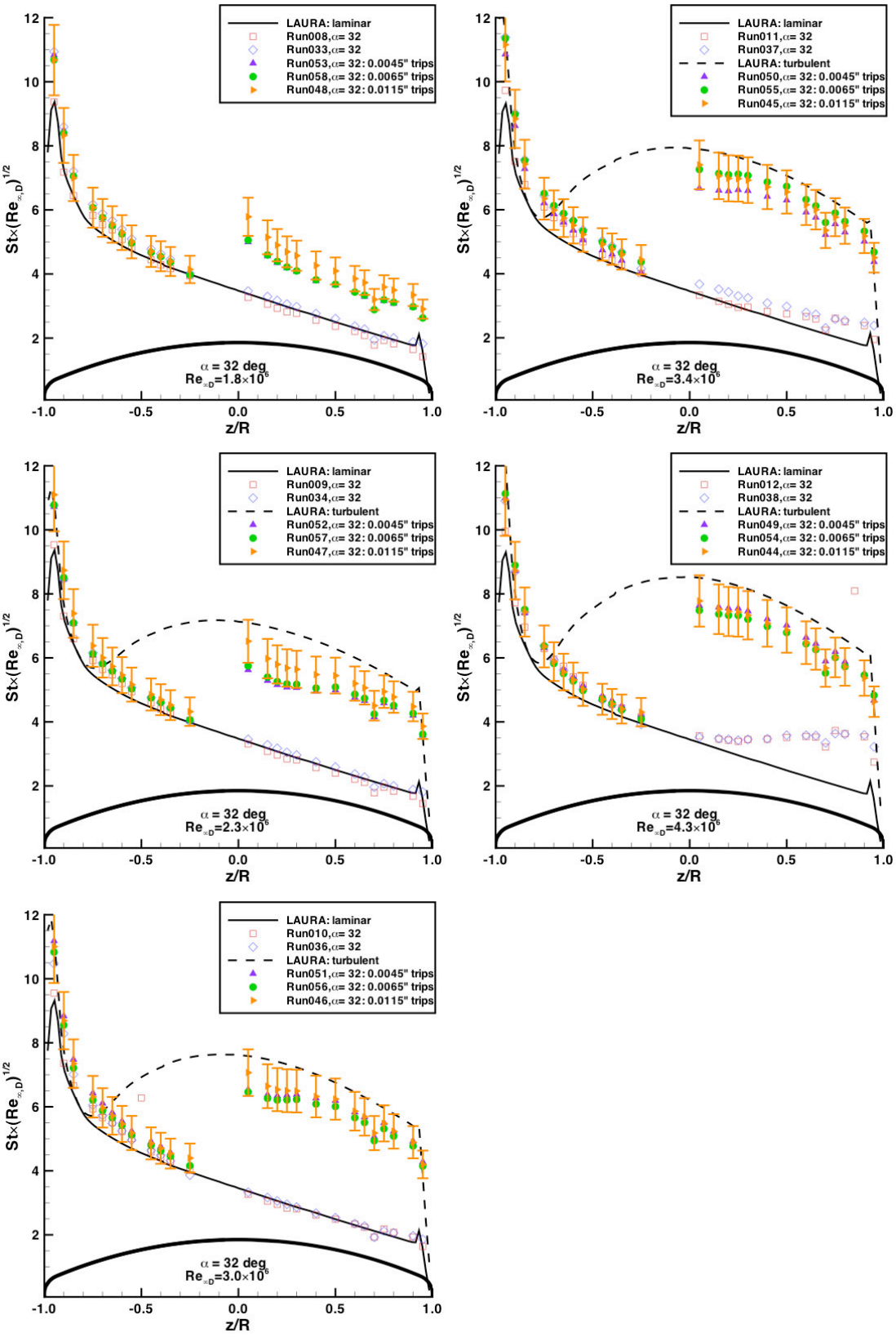

Figure 59. Trip effects on heating, α = 32-deg, $Re_{\infty,D} = 1.8\times10^6$ to 4.3×10^6

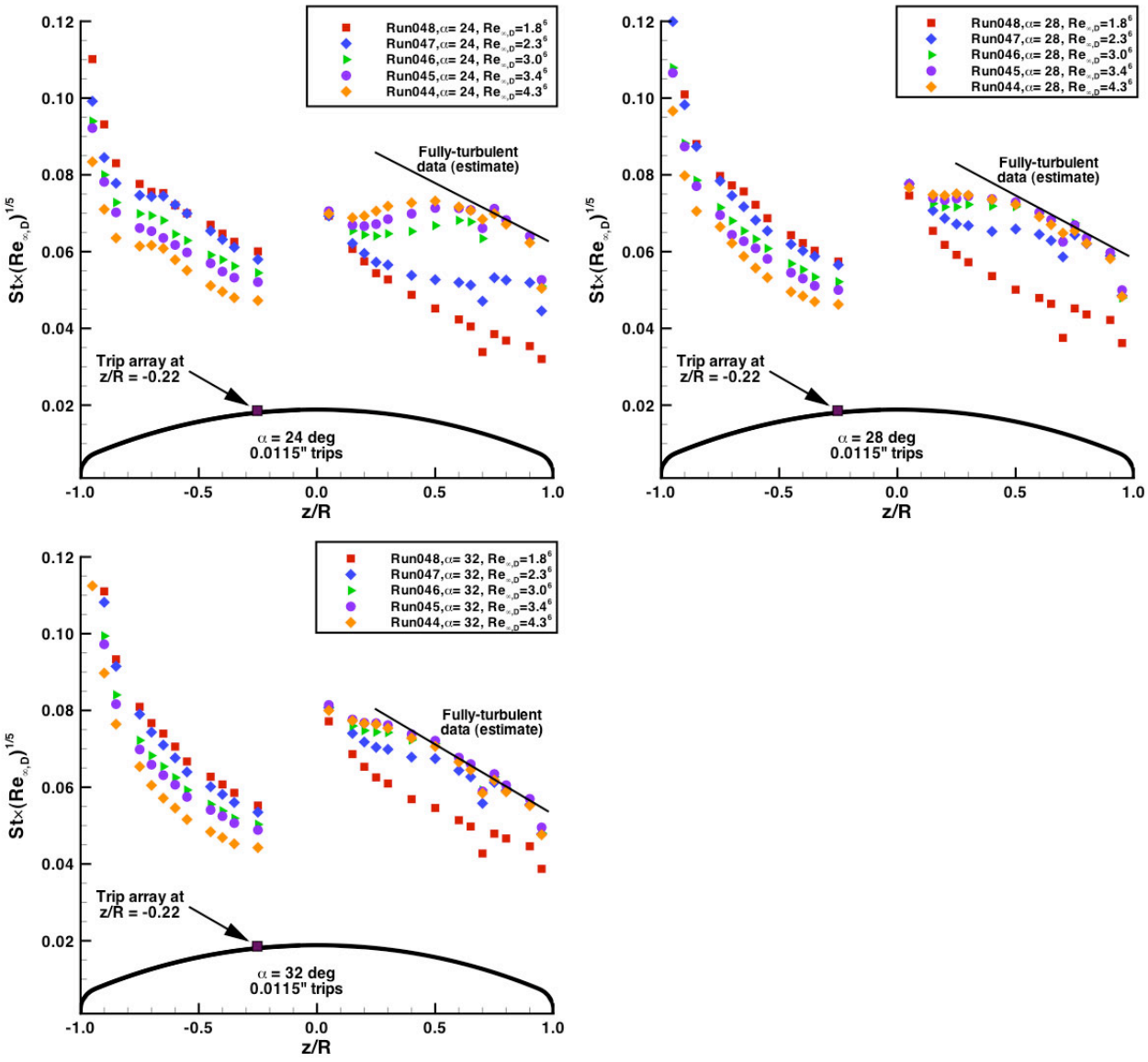

Figure 60. Turbulent correlation of tripped data, α = 24-deg to 32-deg

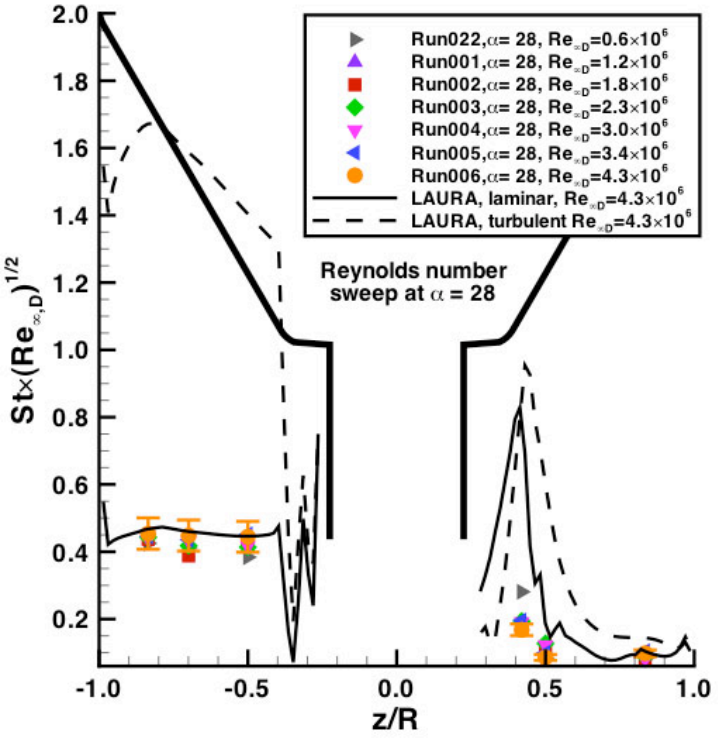

Figure 61. Wake comparison for α = 28-deg, smooth data

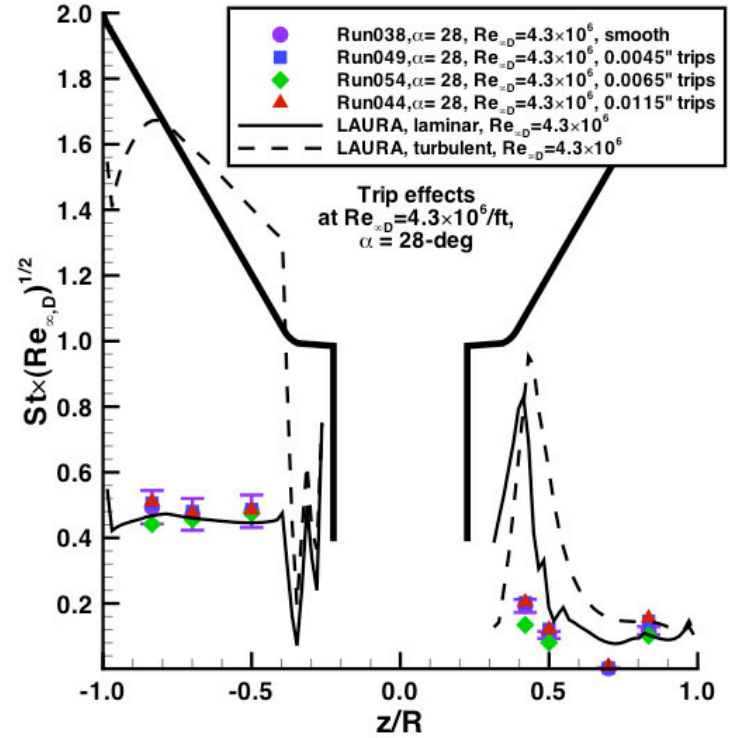

Figure 62. Wake comparison for α = 28-deg, tripped data

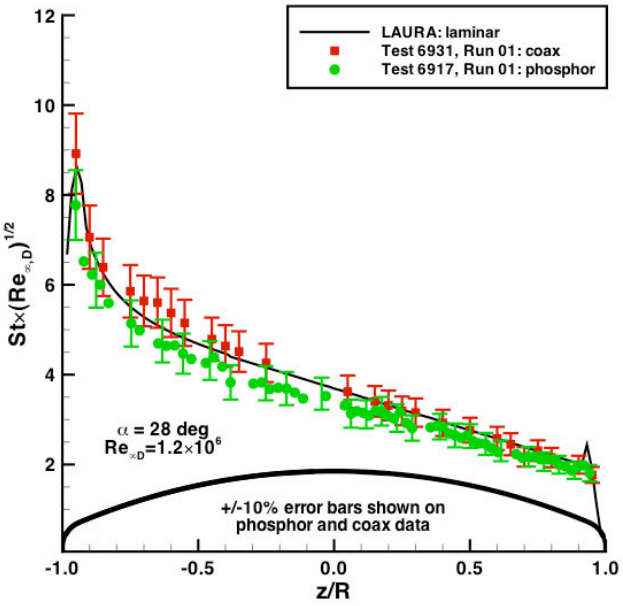

Figure 63. Comparison of smooth-body coaxial gage and global phosphor data for $Re_{\infty,D} = 1.2\times10^6$

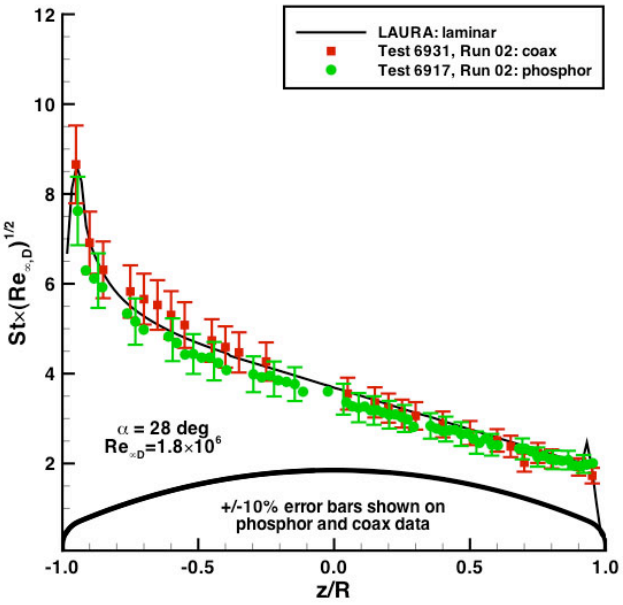

Figure 64. Comparison of smooth-body coaxial gage and global phosphor data for $Re_{\infty,D} = 1.8\times10^6$

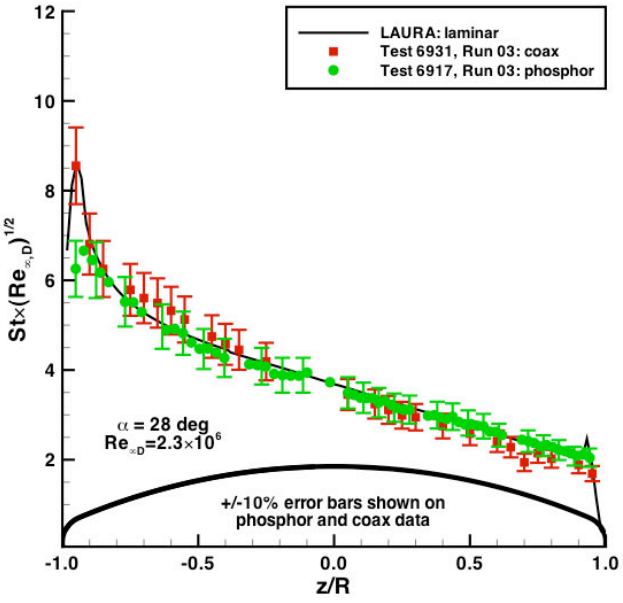

Figure 65. Comparison of smooth-body coaxial gage and global phosphor data for $Re_{\infty,D} = 2.3\times10^6$

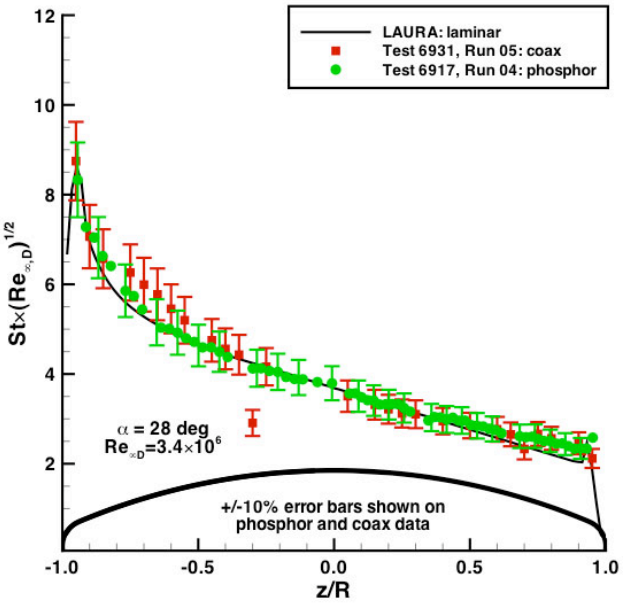

Figure 66. Comparison of smooth-body coaxial gage and global phosphor data for $Re_{\infty,D} = 3.4\times10^6$

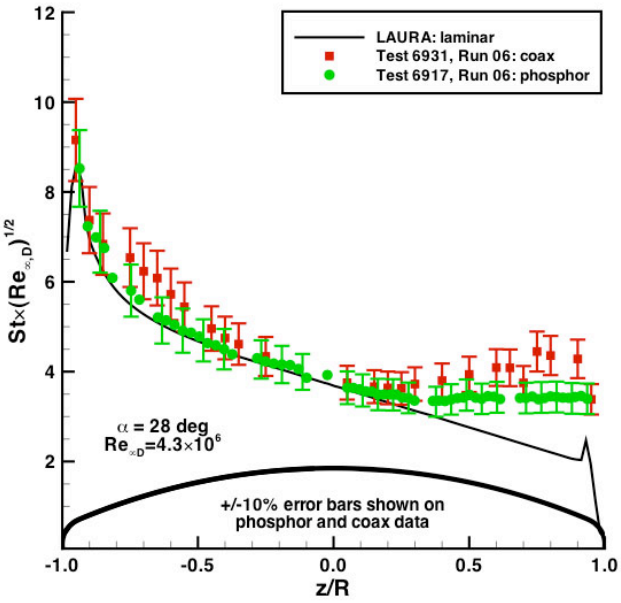

Figure 67. Comparison of smooth-body coaxial gage and global phosphor data for $Re_{\infty,D} = 4.3\times10^6$

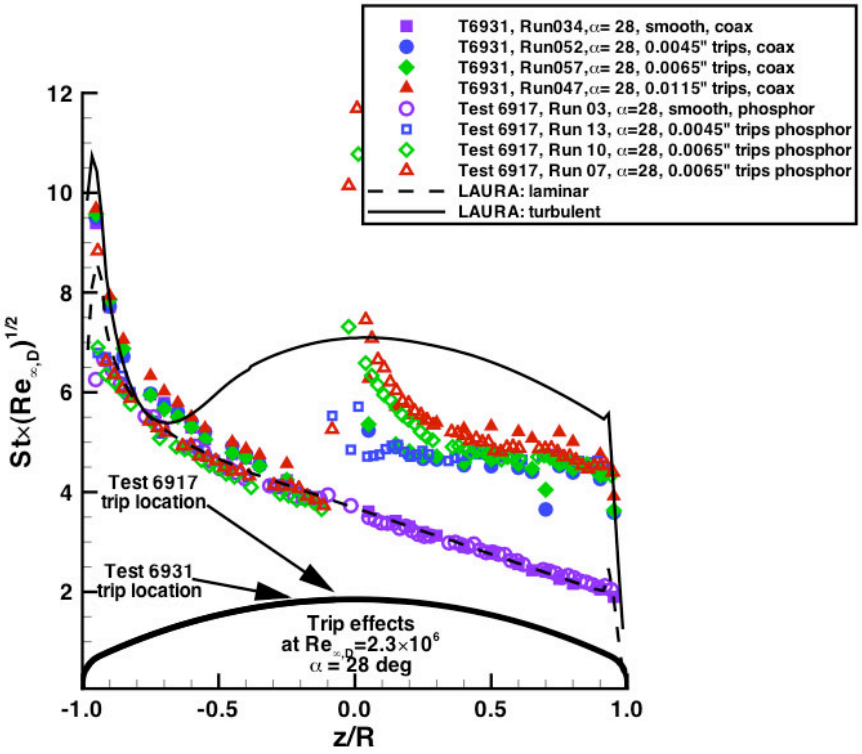

Figure 68. Comparison of tripped coaxial gage and global phosphor data for $Re_{\infty,D} = 2.3\times10^6$

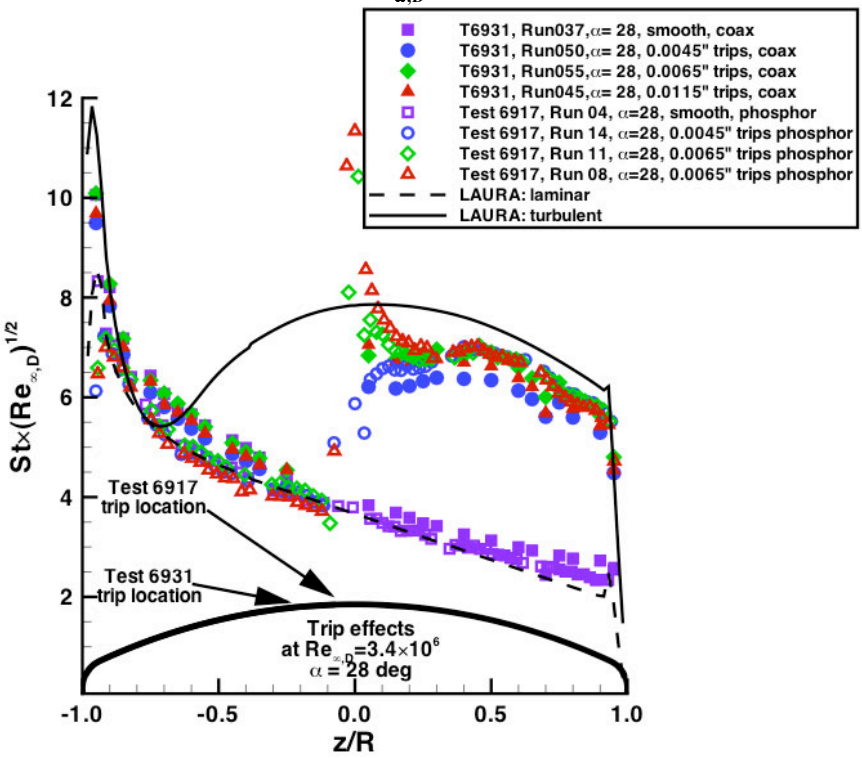

Figure 69. Comparison of tripped coaxial gage and global phosphor data for $Re_{\infty,D} = 3.4\times10^6$

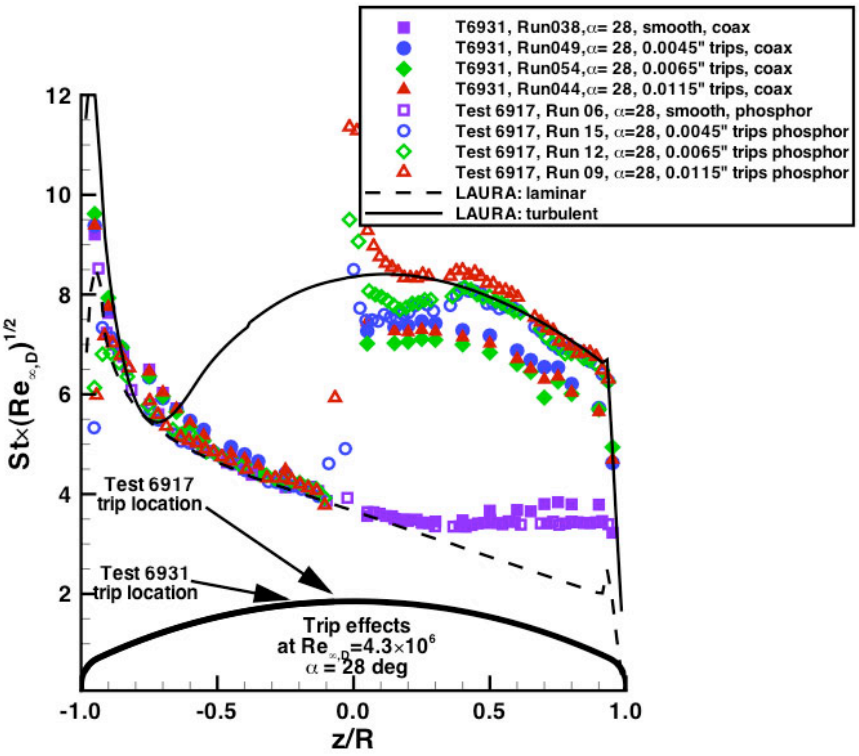

Figure 70. Comparison of tripped coaxial gage and global phosphor data for $Re_{\infty,D} = 4.3\times10^6$

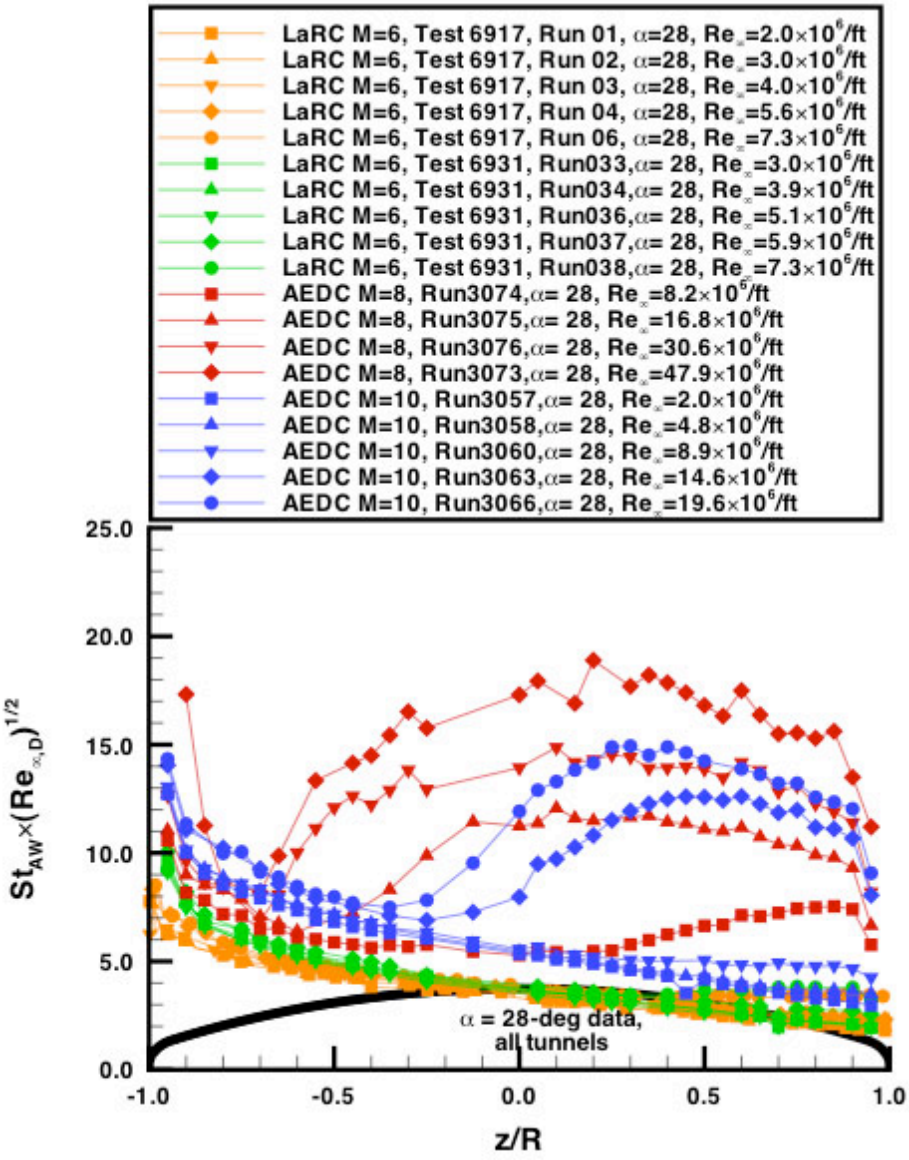

Figure 71. Comparison of AEDC and LaRC coaxial gage data for α = 28-deg using total enthalpy

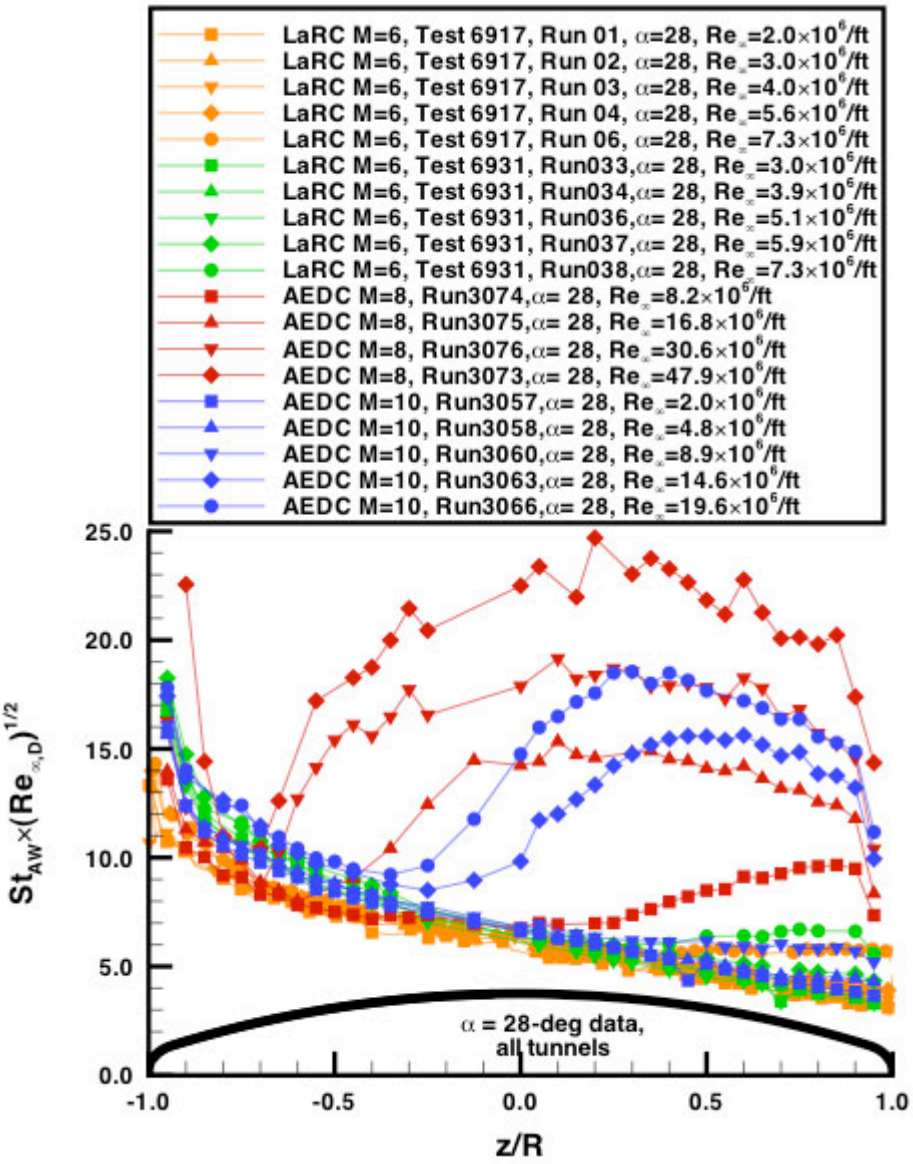

Figure 72. Comparison of AEDC and LaRC coaxial gage data for α = 28-deg using recovery enthalpy

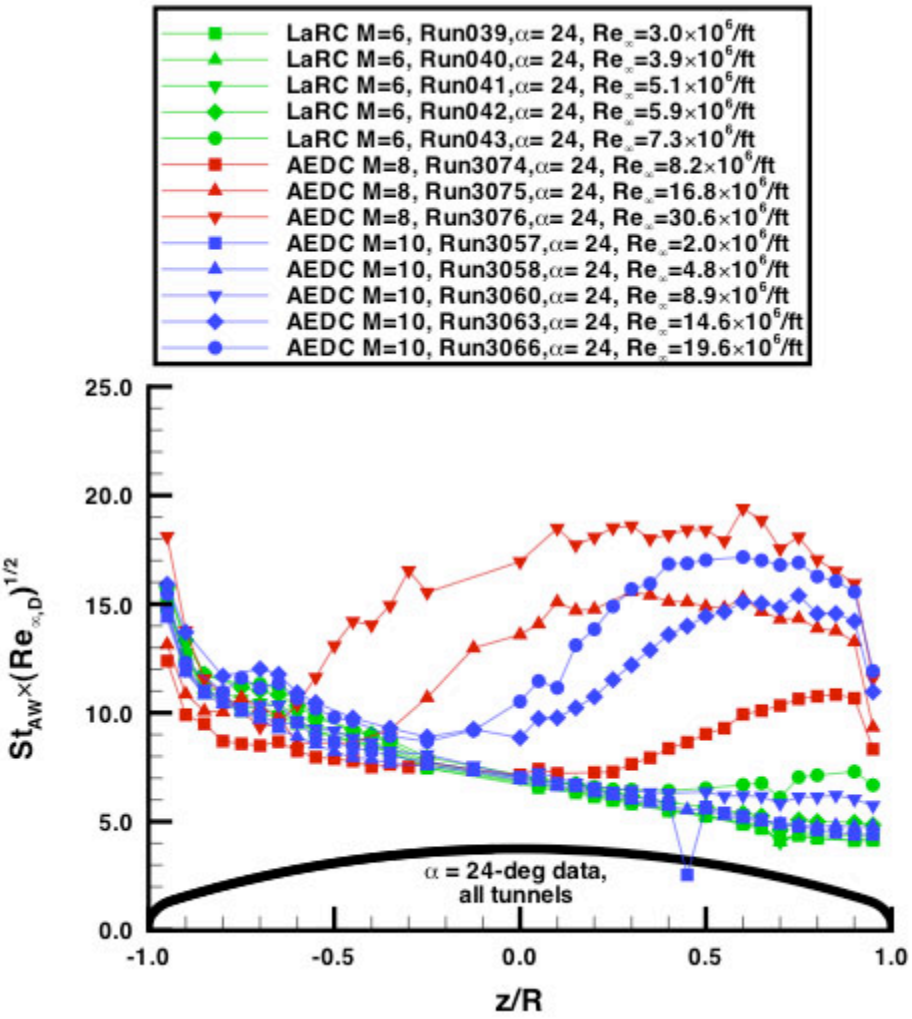

Figure 73. Comparison of AEDC and LaRC coaxial gage data for α = 24-deg using recovery enthalpy

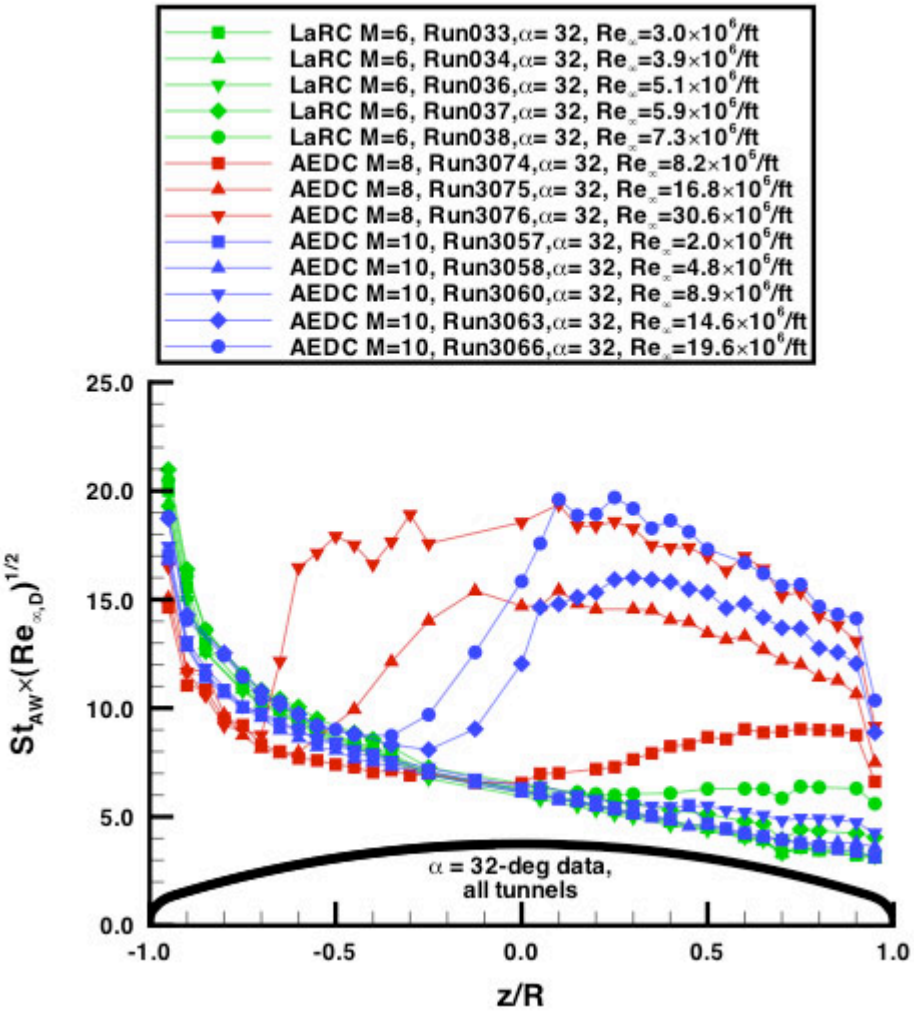

Figure 74. Comparison of AEDC and LaRC coaxial gage data for α = 32-deg using recovery enthalpy

REPORT DOCUMENTATION PAGE

Form Approved
OMB No. 0704-0188

1. REPORT DATE *(DD-MM-YYYY)*	2. REPORT TYPE	3. DATES COVERED *(From - To)*
01- 04 - 2009	Technical Memorandum	

4. TITLE AND SUBTITLE
Experimental Investigation of Project Orion Crew Exploration Vehicle Aeroheating: LaRC 20-Inch Mach 6 Air Tunnel Test 6931

5a. CONTRACT NUMBER

5b. GRANT NUMBER

5c. PROGRAM ELEMENT NUMBER

6. AUTHOR(S)
Hollis, Brian R.

5d. PROJECT NUMBER

5e. TASK NUMBER

5f. WORK UNIT NUMBER
526282.01.07.04.05

7. PERFORMING ORGANIZATION NAME(S) AND ADDRESS(ES)
NASA Langley Research Center
Hampton, VA 23681-2199

8. PERFORMING ORGANIZATION REPORT NUMBER
L-19613

9. SPONSORING/MONITORING AGENCY NAME(S) AND ADDRESS(ES)
National Aeronautics and Space Administration
Washington, DC 20546-0001

10. SPONSOR/MONITOR'S ACRONYM(S)
NASA

11. SPONSOR/MONITOR'S REPORT NUMBER(S)
NASA/TM-2009-215718

12. DISTRIBUTION/AVAILABILITY STATEMENT
Unclassified - Unlimited
Subject Category 02
Availability: NASA CASI (443) 757-5802

13. SUPPLEMENTARY NOTES

14. ABSTRACT

An investigation of the aeroheating environment of the Project Orion Crew Entry Vehicle has been performed in the Langley Research Center 20-Inch Mach 6 Air Tunnel. Data were measured on a ~3.5% scale model (0.1778-m/7-inch diameter) of the vehicle using coaxial thermocouples at free stream Reynolds numbers of 2.0×106/ft to 7.30×106/ft and computational predictions were generated for all test conditions. The primary goals of this test were to obtain convective heating data for use in assessing the accuracy of the computational technique and to validate test methodology and heating data from a test of the same wind tunnel model in the Arnold Engineering Development Center Tunnel 9. Secondary goals were to determine the extent of transitional/turbulent data which could be produced on a CEV model in this facility, either with or without boundary-layer trips, and to demonstrate continuous pitch-sweep operation in this tunnel for heat transfer testing.

15. SUBJECT TERMS
CEV; Aerothermodynamics; Transitional flow; Turbulence

16. SECURITY CLASSIFICATION OF:			17. LIMITATION OF ABSTRACT	18. NUMBER OF PAGES	19a. NAME OF RESPONSIBLE PERSON
a. REPORT	b. ABSTRACT	c. THIS PAGE			STI Help Desk (email: help@sti.nasa.gov)
					19b. TELEPHONE NUMBER *(Include area code)*
U	U	U	UU	84	(443) 757-5802